

Diss. ETH No. 21605

Dynamical Cluster Approximation with continuous lattice
Self-energy.

A thesis submitted to attain the degree of
DOCTOR OF SCIENCES of ETH ZURICH
(Dr. sc. ETH Zurich)

presented by
Peter W. J. Staar
(Master of Science, ETH Zürich)

born on 24 June 1986
citizen of Belgium

accepted on the recommendation of
Prof. Dr. T. C. Schulthess, examiner
Dr. T. A. Maier, co-examiner
Prof. Dr. M. Troyer, co-examiner
Prof. Dr. R. Wallny, chair

2013

Abstract

The goal of this thesis was to investigate how a density-density interaction between electrons on a lattice can lead to the emergence of a phase transition such as anti-ferromagnetism or superconductivity. The prototypical model that is used in this type of studies is the the single band 2D Hubbard model with a strong repulsive interaction. This model is the simplest representation of the high- T_c cuprates and the computation of its phase-diagram has been an outstanding problem over the last three decades in the field of condensed matter theory. In order to make a significant contribution to the field, we pursued a three-fold strategy to compute the transition temperature of a phase transition faster and more accurate. This three-fold strategy can be summarized as: (1) the development of a new algorithm named DCA⁺, (2) a significant improvement to the numerical implementation of the CT-AUX cluster-solver and (3) porting the algorithm to new hard-ware in order to harness the full power of a supercomputer. These three strategies are explained in detail respectively in chapter 2, 3 and 5. In chapter 4, we investigate several regions of the phase-diagram of the 2D Hubbard model and ultimately show that the lightly hole-doped Hubbard model with a strong repulsive interaction $U/t = 7$ has a finite T_c of $0.05t$. This region of the phase-diagram was not reachable up till now and was only possible due to a successful completion of each strategy. In chapter 6, I introduce a new algorithm to compute the spectrum of electronic lattice models. Contrary to other methods that have the same goal, this method obtains the spectrum by analytically continuing the self-energy through a straightforward constrained minimization process. Despite its utter simplicity, it reproduces the spectra of NiO very accurately.

Abstract

Das Ziel dieser Doktorarbeit ist die Bedingungen zu studieren, unter welchen eine Dichte-Dichte Wechselwirkung zwischen Elektronen auf einem Gitter zu Phasenübergängen, wie zum Beispiel Ferro-Magnetismus oder Supraleitung, führen kann. Für diese Art von Untersuchungen wird als Standardmodell das zweidimensionale Hubbard Modell mit stark abstoender Wechselwirkung betrachtet, wobei nur ein Energieband berücksichtigt wird. Dies ist die einfachste Darstellung eines Hochtemperatur Cuprat-Supraleiters. Die Berechnung des zugehörigen Phasendiagramms ist ein seit über drei Jahrzehnten offenes Problem in der Theorie der kondensierten Materie. Mit dem Ziel diesem Gebiet signifikant beizutragen wurden die folgenden drei Schritte befolgt, die es ermöglichen, die Übergangstemperatur eines Phasenübergangs schneller und präziser zu bestimmen: (1) Die Entwicklung eines neuen Algorithmus namens DCA^+ , (2) die wesentliche Verbesserung der numerischen Implementation des CT-AUX Cluster-Solvers und (3) die Anpassung des Algorithmus an neue Hardware, um die Kapazität eines Supercomputers vollständig nutzen zu können. Die einzelnen Schritte sind entsprechend in Kapitel 2, 3 und 5 im Detail erklärt. In Kapitel 4 werden diverse Regionen des Phasendiagramms des zwei dimensional Hubbard Modells untersucht und es wird allgemeingültig gezeigt, dass das schwach Lochgedopte Hubbard Modell mit stark abstoender Wechselwirkung $U/t = 7$ eine endliche kritische Temperatur T_c von $0.05t$ besitzt. Bis dato war dieser Abschnitt des Phasendiagramms nicht darstellbar und ist nur aufgrund der Komplettierung der obigen Schritte zugänglich geworden. In Kapitel 6 wird ein neuer Algorithmus zur Berechnung des Spektrums von Elektronen-Gittermodellen vorgestellt. Im Unterschied zu anderen Vorgehensweisen wird das Spektrum hier dadurch bestimmt, dass ein durch direkte Bedingungen eingeschränkter Minimierungsprozess die Eigenenergien analytisch erweitert. Trotz ihrer Schlichtheit reproduziert diese Methode das Spektrum von NiO äusserst präzise.

Acknowledgements

I would like to express my gratitude to all those who gave me the possibility to complete this thesis. First and foremost, I am deeply indebted to my supervisor T. C. Schulthess whose help and stimulating suggestions helped me during the time of my research and the writing of this thesis. Without his expertise and support, I would have never been able to successfully participate in the Gordon Bell prize. Next, I also want to thank T. A. Maier from the bottom of my heart for explaining the concepts of the DCA and helping me to overcome some of the difficulties we encountered while developing the DCA⁺ algorithm. I have furthermore to thank M. S. Summers and G. Alvarez for the help in understanding the DCA++ code.

I am grateful to my colleagues in the Schulthess group. I want to thank them for all their help, support, interest and valuable hints. Especially, I want to thank R. Solca for all his assistance with regard to the GPU's.

I want to thank the secretaries of the theoretical physics department for all the help with the administration.

Last but not the least, I would like to thank my girlfriend Sofia whose patience enabled me to complete this work.

Contents

Contents		vii
1 Introduction		1
2 Theory of the DCA⁺		5
2.1 Introduction		6
2.2 Theory		8
2.2.1 DCA and DCA ⁺ formalisms:		9
2.2.2 Structure of a DCA ⁺ cluster-calculation:		12
2.2.3 Analysis of the projection operator $P_{i,j}$ and its connection to the locality of $\Sigma(\vec{k})$:		15
2.2.4 Role of the cluster in the DCA ⁺		20
2.3 Implementation of the self-consistent loop.		21
2.3.1 Interpolation		21
2.3.2 Cluster Deconvolution		26
2.4 Theory and implementation of the two-particle framework.		30
2.4.1 Detection of phase-transitions in the DCA		31
2.4.2 Thermodynamic self-consistency and its implication for the DCA ⁺		32
2.4.3 Algorithm for the lattice-vertex $\Gamma(\vec{k}_1, \vec{k}_2)$		34
3 Implementation of the CT-AUX cluster-solver:		37
3.1 Introduction		38
3.2 The Continuous-Time Auxiliary Field algorithm		41
3.2.1 The partition function expansion.		41
3.2.2 The metropolis sampling procedure.		43
3.3 Introduction of submatrix updates in the CT-AUX		44
3.4 The random walk with submatrix updates		47
3.4.1 Preparation steps		48
3.4.2 Insertion, removal, spinflip of an auxiliary spins		48

3.4.3	Recompute step	48
3.4.4	Speed-up versus submatrix k_s	49
3.5	Single and two-particle measurement with d-NFFT:	50
3.5.1	measurement of single particle quantities	50
3.5.2	measurement of two-particle Greens-function G^{II}	55
4	Study of phase-diagram of the 2D Hubbard model.	59
4.1	Introduction	60
4.2	The anti-Ferromagnetic transition in the 2D repulsive Hubbard model.	62
4.3	Investigation of the pseudogap-region in the 2D repulsive Hubbard model.	63
4.4	Superconducting transition temperature T_c in 2D attractive Hubbard model.	68
4.5	Superconducting transition temperature T_c in 2D repulsive Hubbard model.	71
4.5.1	The superconducting transition for 10% hole doping at $U/t = 4$	71
4.5.2	Signatures of a Klosterlitz-Thouless transition.	75
4.5.3	The superconducting transition for 10% hole doping at $U/t = 7$	77
5	Scaling and performance of DCA⁺ on leadership systems.	79
5.1	Introduction	80
5.2	Implementation and method of performance measurements	81
5.3	Computer systems and performance model	83
5.4	Performance results at scale	86
6	Continuous-Pole-Expansion: A novel method to obtain the spectrum of electronic lattice models.	93
6.1	Introduction	94
6.2	Analytical properties of Fermionic Green's function and self-energy	97
6.3	Continuous pole expansion for the self-energy	99
6.4	Validation of CPE with Exact Diagonalization.	102
6.5	Application to Physical problems	104
6.5.1	Momentum-dependent gap formation in half-filled 2D Hubbard model.	105
6.5.2	Band-structure of NiO	109
6.6	Conclusions	115
7	Press Releases	117
7.1	ORNL	117
7.2	CSCS press release	120

Bibliography

125

Chapter 1

Introduction

For over a century, superconductivity has fascinated generations of physicists and materials scientists, and continues to captivate researchers as new classes of superconducting materials are discovered. Below a certain critical temperature T_c , superconductors exhibit conductance without resistance as well as perfect diamagnetism, i.e. a complete expulsion of an external magnetic field (Meissner-Ochsenfeld effect), implying that the electrons behave in a collective manner. This is possible, because of a net attractive interaction forcing electrons to form boson-like Cooper pairs, which can condense into a coherent macroscopic quantum state analogous to a Bose-Einstein condensate. The energy required to break up pairs (also called energy gap) suppresses the scattering processes from defects and impurities that would give rise to electrical resistance in normal conductors.

In conventional superconductors, which include many elemental metals such as Hg, Al and Nb, the attractive interaction between electrons arises from the interaction between the negatively charged electrons and the positively charged ions. The distortion of the ion lattice left behind by the motion of an electron attracts a second electron and thus results in an effective attractive interaction between the electrons. This mechanism is active and can overcome the instantaneous Coulomb repulsion at long times, or low energies, because the ion dynamics is slow compared to the electrons. This retardation, however, also limits the magnitude of T_c that can be reached in these systems. These concepts are well described and understood within a rigorous theoretical foundation, the BCS (Bardeen-Cooper-Schrieffer) theory [8], and its extension, the Migdal-Eliashberg theory [68, 20].

The high-temperature superconducting copper-oxide based materials (high- T_c cuprates), discovered in 1986, have much higher critical temperatures, up to 150 K, exceeding by far the theoretical limit of conventional superconductors. Early on this triggered speculations that superconductivity in these systems arises from a different mechanism. In addition, the spatial compo-

ment of the pair wave function was found to have $d_{x^2-y^2}$ -wave structure, different from the isotropic s -wave structure in conventional superconductors. It is by now generally accepted that pairing in these systems has a different origin and most likely arises from the strong magnetic interactions or fluctuations between the electron spins that result in an antiferromagnetic phase in the undoped parent compounds [73]. The details of how superconductivity emerges from the highly enigmatic pseudogap phase, which dominates much of the higher temperature phase diagram of the doped systems, is still under heavy debate.

The physics of these crystalline systems is well described by a Hamiltonian that is expanded in atomic orbitals

$$\mathcal{H} = \sum_{ij,\mu\nu,\sigma} t_{ij}^{\mu\nu} c_{i\mu\sigma}^\dagger c_{j\nu\sigma} + \sum_{ij,\mu\nu,\sigma\sigma'} U_{ij}^{\mu\nu,\sigma\sigma'} n_{i\mu\sigma} n_{j\nu\sigma'}, \quad (1.1)$$

where the fermionic creation (destruction) $c_{i\mu\sigma}^\dagger$ ($c_{i\mu\sigma}$) operator creates (destroys) an electron with spin σ in atomic orbital μ on lattice site i , $n_{i\mu\sigma} = c_{i\mu\sigma}^\dagger c_{i\mu\sigma}$ is the corresponding number operator and non-density-density interactions have been neglected. The transition amplitudes $t_{ij}^{\mu\nu}$ between orbitals on different sites and Coulomb interactions $U_{ij}^{\mu\nu,\sigma\sigma'}$ can be computed from ab initio electronic structure calculations [4, 3, 5, 7, 48, 66, 69] – these quantities decay rather fast with distance between lattice sites due to the spatial locality of the atomic orbitals and screening effects.

However, despite the simplicity of the Hamiltonian, the theoretical description of these systems is extremely challenging. Traditional many-body perturbation theory cannot be used, due to the absence of a small parameter, and current implementations based on density functional theory (DFT), are unable to adequately describe the strong electronic correlations that underly the physics of this system, particularly the physics of the superconducting state. However, DFT calculations of the electronic ground state show – in remarkable agreement with photoemission experiments – that the low-energy electronic structure is governed by a single band of electrons formed by the Cu $3d_{x^2-y^2}$ and the O $2p_{x/y}$ orbitals of the CuO planes. The physics of this band may be described by a single-band Hubbard model

$$\mathcal{H} = -t \sum_{\langle ij \rangle, \sigma} c_{i\sigma}^\dagger c_{j\sigma} + U \sum_i n_{i\uparrow} n_{i\downarrow}, \quad (1.2)$$

where the sums run over the sites i of a 2D square lattice and the notation $\langle ij \rangle$ indicates that the j -summation runs only over the four near neighbor sites of i . The second term describes an on-site Coulomb repulsion that

raises the energy when two electrons reside on the same site and therefore favors singly occupied sites and thus moment formation. Numerical calculations based on this model have found many phenomena similar to what has been observed experimentally, including antiferromagnetism, pseudogap behavior and strong d-wave pair correlations, and are thought to be the simplest to capture qualitatively the relevant physics of superconductivity in the cuprates. The reliable computation of the superconducting transition temperature, however, has thus far posed insurmountable computational challenges for even this simplified model.

Simulations based on the Dynamical Cluster Approximation (DCA) showed that the model describes a superconducting transition with *d*-wave character [60], and even allowed an analysis of the pairing mechanism [61]. But they were far from converged due to a notorious cluster shape dependence of the results computed within the DCA. Furthermore, the simulations of T_c were done at an unrealistically small value of $U/t = 4$, since the fermionic sign problem of the quantum Monte Carlo algorithms used as a cluster solver within the DCA, prevented simulations for values of $U/t = 7$ that would be more realistic for these systems.

A quantitative description that accounts for, e.g., materials specific variation of T_c between different cuprates, requires calculations based on the more complex multi-orbital model, see Eq. (1.1), which explicitly take into account additional bands and orbitals and thus can distinguish between different materials. Extending the computation to multiple orbitals and inclusion of realistic, materials specific electronic structure is not conceptually difficult. However, plans to do so have remained elusive, as the reliable solution of even the simple single-band Hubbard model has posed insurmountable computational challenges.

Chapter 2

Theory of the DCA⁺

Abstract

The dynamical cluster approximation (DCA) is a systematic extension beyond the single site approximation in dynamical mean field theory (DMFT), to include spatially non-local correlations in quantum many-body simulations of strongly correlated systems. In this chapter, we present an extension to the DCA, that can incorporate a continuous lattice self-energy in order to achieve better convergence with cluster size. The new method, which we call DCA⁺, cures the cluster shape dependence problems of the DCA, without suffering from causality violations of previous attempts to interpolate the cluster self-energy. A practical approach based on standard inference techniques is given to deduce the continuous lattice self-energy from an interpolated cluster self-energy. We will also discuss in detail how the two-particle framework of the DCA can be extended to the DCA⁺. The latter is of particular importance with regard to the determination of the critical temperature of a phase-transition in the lattice.

relevant papers:

- M. Jarrell, Th. Maier, C. Huscroft and S. Moukouri, *A Quantum Monte Carlo Algorithm for Non-local Corrections to the Dynamical Mean-Field Approximation*, Phys. Rev. B 64, 195130 (2001).
- T. Maier, M. Jarrell, Th. Pruschke and M. Hettler, *Quantum Cluster Theories*, Reviews of Modern Physics, 77, pp. 1027-1080 (2005).
- P. Staar, T. Maier and T. C. Schulthess, *Dynamical cluster approximation with continuous lattice self-energy*, Phys. Rev. B 88, 115101 (2013)
- P. Staar, T. Maier and T. C. Schulthess, *Detecting phase-transitions in electronic lattice-models with DCA⁺*, to be published soon (2013)

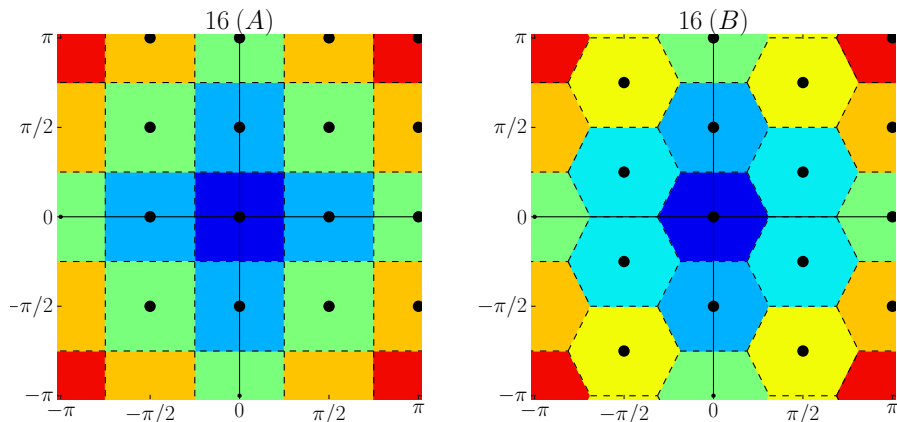


Figure 2.1: The positions of the cluster momenta $\{\vec{K}\}$ and shape of the patches for two 16 site DCA-clusters. Notice that the 16B site cluster does not have the same point-group symmetry as the Brillouin-zone, leading to a lattice self-energy with a lower symmetry.

2.1 Introduction

The Dynamical Cluster Approximation was developed to study materials of 2D nature, by allowing the self-energy to be non-local. In the DCA, the infinite lattice-problem is reduced to a finite size quantum cluster impurity with periodic boundary conditions, embedded into a self-consistent mean-field. This reduction is achieved via a coarse-graining procedure of the Green's function, in which the Brillouin zone is divided into N_c patches and the self-energy Σ is assumed to be constant on these patches. In this way, all correlations within the cluster are dealt with exactly, while long-range correlations outside the cluster are described via a mean-field. If the cluster impurity problem is solved exactly, such as with Quantum Monte Carlo (QMC) integration, the DCA will reproduce the exact solution of the lattice model in the limit of infinite cluster size.

In practice, the fermionic sign problem [55, 98] imposes an upper-bound to the cluster-size and a lower bound to the temperature which can be accessed. While small clusters have proven to give us an excellent qualitative insight on the physical phenomena [62], most physical quantities, such as the superconducting transition temperature T_c , converge poorly on the available small clusters [60]. The DCA can therefore not be used as a reliable method for quantitative predictions of those observables.

There are two important factors that influence the results of the DCA, both

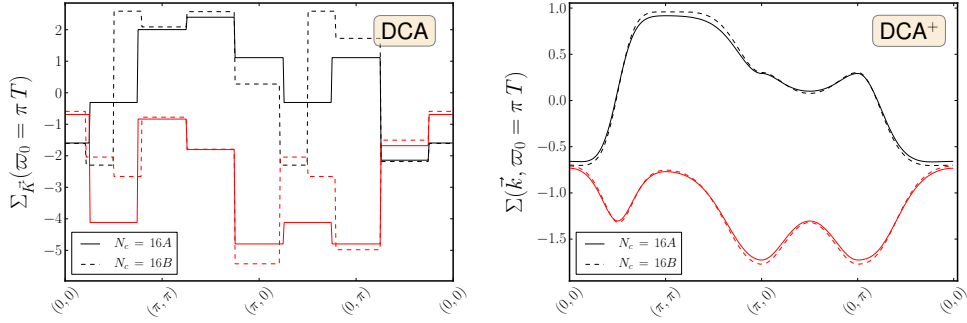


Figure 2.2: Momentum-dependence of the DCA and DCA⁺ self-energies (red and black represent the imaginary and real part) calculated on the 16A and 16B clusters in a half-filled Hubbard model with nearest neighbor hopping $t = 1$, Coulomb interaction $U/t = 7$ and next-nearest neighbor hopping $t'/t = -0.15$ at a temperature $T = 0.2$. For the DCA, one clearly sees a large difference between the self-energies of the two clusters at the section $(\pi, 0) \rightarrow (0, \pi)$, which is close to the Fermi-surface and thus physically the most relevant part of the self-energy. In the DCA⁺, the self-energies of the two clusters agree very well.

related to the choice of the cluster. The most obvious factor is the mean field approximation, which reduces the momentum anisotropy of the self-energy as the clusters become smaller. One can only avoid this error by considering clusters with a sufficiently large size. In practice, the critical cluster-size is obtained by comparing physical quantities on different cluster-sizes. More complicated is the influence of the geometry of the cluster. There is a set of different clusters, all of which have the same cluster size but different shape and therefore different positions of the cluster momentum points. In Fig. 2.1, we show two 16 site clusters for which this is the case. The different positioning of the cluster momentum points in these two clusters leads to a different geometric shape of the coarse-graining patches and thus a different parametrization of the self-energy. This is illustrated in Fig. 2.2, where the momentum dependence of the DCA self-energy at the lowest Matsubara frequency is shown for the 16A and 16B site cluster introduced in Fig. 2.1. The relative error between the self-energies on the different clusters is close to 100% around the Fermi-surface, making it unsuitable to derive any quantitative results from this calculation.

One can argue that the influence of the mean-field approximation for clusters with the same size is similar. Therefore, the difference in results can be brought back to the shape of the coarse-graining patches. One example is the difference in superconducting transition temperature T_c between the 16A and 16B site cluster [60]. The role of the geometry has been studied inten-

sively by investigating the evolution of the magnetic and superconducting transition temperatures over different cluster sizes [60, 93] or by comparing the site-occupancies of different clusters over a wide range of doping [102, 28].

The geometric shape dependence of the self-energy is built into the DCA by construction, since the DCA self-energy is expanded on the coarse-grain patches as [25]

$$\Sigma(\vec{k}, \omega_m) = \sum_i \varphi_{\vec{K}_i}(\vec{k}) \Sigma_{\vec{K}_i}(\omega_m). \quad (2.1)$$

Here, the set of patches $\{\varphi_{\vec{K}_i}(\vec{k})\}$ is formally defined through the cluster-momenta $\{\vec{K}_i\}$,

$$\varphi_{\vec{K}_i}(\vec{k}) = \begin{cases} 1 & \forall j : |\vec{k} - \vec{K}_i| \leq |\vec{k} - \vec{K}_j| \\ 0 & \exists j : |\vec{k} - \vec{K}_i| > |\vec{k} - \vec{K}_j| \end{cases} \quad (2.2)$$

and $\Sigma_{\vec{K}_i}(\omega_m)$ is the cluster self-energy for momentum \vec{K}_i .

In this paper, we present an extension to the DCA that allows the self-energy to be expanded in an arbitrary large set of smooth basis-functions, and thereby itself becoming a smooth function of momentum. The inclusion of a smooth self-energy into the framework of the DCA requires a new fundamental look at the algorithm. The resulting extended algorithm will be called DCA⁺, indicating an incremental generalization to the well-known DCA algorithm. The distinguishing feature of the DCA⁺ algorithm that sets it apart from the DCA algorithm is that cluster and lattice self-energies are in general different. In the DCA, the lattice self-energy $\Sigma(\vec{k})$ is a simple extension of the cluster self-energy $\Sigma_{\vec{K}_i}$ via the step function form in Eq. (2.1). It therefore has jump discontinuities between the patches. In the DCA⁺ the lattice self-energy is a function with continuous momentum dependence, which, when coarse grained is equal to the cluster self-energy.

2.2 Theory

In this section, we present the generic structure of the DCA⁺ algorithm, without going into any implementation details. First, we introduce the key features of the DCA⁺ algorithm that distinguish it from the DCA, and show that the latter is just a specialization of the former. Next, we present a geometric interpretation of the DCA⁺ algorithm in terms of the functional representation space of the self-energy. This interpretation provides guidance for how cluster-dependent features are incorporated into the lattice

self-energy, and offers insights for the derivation of a practical implementation of the DCA⁺ algorithm that will be discussed in the following section. In order to keep the notation simple, we will omit the frequency parameter ω in all equations. Furthermore, all single-particle functions defined on the impurity-cluster are represented by a subscript on the cluster-momenta (e.g. the cluster self-energy $\Sigma_{\vec{k}}$), while the continuous lattice single-particle functions will have the usual dependence on the momentum vector \vec{k} (e.g. the lattice self-energy $\Sigma(\vec{k})$). An overline over the quantity signifies that the latter has been coarsegrained.

2.2.1 DCA and DCA⁺ formalisms:

A system of interacting electrons on a lattice is generally described by a Hamiltonian $H = H_0 + H_{\text{int}}$, where the kinetic energy H_0 is quadratic in the fermion operators and the interaction H_{int} is quartic. Its free energy Ω may be written in terms of the exact single-particle Green's function G as

$$\Omega[G] = \text{Tr} \ln(-G) + \Phi[G] - \text{Tr}[(G_0^{-1} - G^{-1})G]. \quad (2.3)$$

Here we have used a matrix notation for the Green's function G of the interacting system described by H and the Green's function G_0 of the non-interacting system described by H_0 . $\Phi[G]$ is the Luttinger-Ward functional [57] given by the sum of all vacuum to vacuum "skeleton" diagrams drawn with G . The self-energy Σ is obtained from the functional derivative of $\Phi[G]$ with respect to G [10, 9]

$$\Sigma = \frac{\delta \Phi[G]}{\delta G}, \quad (2.4)$$

and is related to the Green's function via the Dyson equation

$$G_0^{-1} - G^{-1} = \Sigma. \quad (2.5)$$

These two relations imply that the free energy is stationary with respect to G , i.e. $\delta \Omega[G]/\delta G = 0$. In principle, the exact Green's function G and self-energy Σ can be determined from the self-consistent solution of Eqs. (2.4) and (2.5). However, since the functional $\Phi[G]$ is usually unknown, an approximation is required that replaces the exact $\Phi[G]$ by a known or a computable functional. Conserving approximations replace the exact $\Phi[G]$ by an approximate functional, which sums up certain subclasses of diagrams that are thought to capture the dominant physics. In general, this results in a weak coupling approximation. A different approach is taken in the DCA:

rather than approximating the Luttinger Ward Φ , the functional representation space of the Green's function is reduced by replacing the exact Green's function $G(\vec{k})$ by a *coarse-grained* Green's function $\bar{G}_{\vec{K}}$ in momentum space defined as

$$\bar{G}_{\vec{K}} = \int d\vec{k} \varphi_{\vec{K}}(\vec{k}) G(\vec{k}). \quad (2.6)$$

where the coarse-graining functions $\varphi_{\vec{K}}(\vec{k})$ have been defined in Eq. (2.2). We note that approximating G in this way corresponds to an approximation of the Laue function, $\Delta_{\vec{k}_1+\vec{k}_3, \vec{k}_2+\vec{k}_4}$, which expresses momentum conservation at each vertex in the diagrams defining Φ [34, 39]. For the single site DMFT approximation ($N_c = 1$), $\varphi(\vec{k})$ is constant over the entire Brillouin zone, and consequently the Laue function is replaced by $\Delta_{\text{DMFT}} = 1$, i.e. momentum conservation is disregarded. For a finite size DCA cluster ($N_c > 1$), the Laue function restores momentum conservation for the cluster momenta \vec{K} and reads in terms of the $\varphi_{\vec{K}}(\vec{k})$

$$\begin{aligned} \Delta_{\text{DCA}}(\vec{k}_1, \vec{k}_2, \vec{k}_3, \vec{k}_4) &= \delta_{\vec{k}_1+\vec{k}_3, \vec{k}_2+\vec{k}_4} \\ &\times \varphi_{\vec{K}_1}(\vec{k}_1) \varphi_{\vec{K}_2}(\vec{k}_2) \varphi_{\vec{K}_3}(\vec{k}_3) \varphi_{\vec{K}_4}(\vec{k}_4). \end{aligned} \quad (2.7)$$

By replacing the exact Laue function with its DCA approximation in the Luttinger Ward functional, the momentum integrals over the Green's functions in the diagrams defining the Φ -functional are reduced to sums over the finite set of coarse-grained Green's functions defined in Eq. (2.6). This way, $\Phi[\bar{G}]$ becomes identical to the Luttinger-Ward functional of a finite size cluster and the computation of the corresponding self-energy

$$\Sigma_{\vec{K}}^{\text{DCA}} = \delta\Phi[\bar{G}_{\vec{K}}]/\delta\bar{G}_{\vec{K}} \quad (2.8)$$

becomes feasible. As such, within the DCA approximation the free energy functional $\Omega[G]$ becomes

$$\Omega_{\text{DCA}}[G] = \text{Tr} \ln(-G) + \Phi[\bar{G}] - \text{Tr}[(G_0^{-1} - G^{-1})G].$$

From stationarity of the free energy, $\delta\Omega[G]/\delta G = 0$, one obtains the Dyson equation within the DCA

$$G_0^{-1}(\vec{k}) - G^{-1}(\vec{k}) = \sum_{\vec{K}} \varphi_{\vec{K}}(\vec{k}) \Sigma_{\vec{K}}^{\text{DCA}}. \quad (2.9)$$

Here, the right hand side follows from $\delta\bar{G}_{\vec{k}}/\delta G = \varphi_{\vec{k}}(\vec{k})$ and $\delta\Phi[\bar{G}_{\vec{k}}]/\delta\bar{G}_{\vec{k}} = \Sigma_{\vec{k}}^{\text{DCA}}$. Eqs. (2.6), (2.8) and (2.9) form a closed set of equations which is solved iteratively until self-consistency is reached. This is the DCA algorithm. Following Eq. (2.9), the self-energy $\Sigma(\vec{k})$ of the lattice Green's function $G(\vec{k})$, which is used to compute the coarse-grained Green's function in Eq. (2.6), is approximated by a piecewise constant continuation of the cluster self-energy $\Sigma_{\vec{k}}^{\text{DCA}}$, which changes between different momentum patches but is constant within a given patch,

$$\Sigma(\vec{k}) = \sum_{\vec{K}} \Sigma_{\vec{K}}^{\text{DCA}} \varphi_{\vec{K}}(\vec{k}). \quad (2.10)$$

With the DCA⁺ algorithm we introduce in this paper, the DCA framework is extended to allow for a more general relationship between the lattice self-energy $\Sigma(\vec{k})$ and cluster self-energy $\Sigma_{\vec{K}}$ than that in Eq. (2.10). In the DCA⁺, in analogy with Eq. (2.6), we only demand the cluster self-energy to be equal to the coarse-grained lattice self-energy,

$$\bar{\Sigma}_{\vec{K}} = \int d\vec{k} \varphi_{\vec{K}}(\vec{k}) \Sigma(\vec{k}). \quad (2.11)$$

In the DCA algorithm, this requirement is trivially satisfied since according to Eq. (2.10), $\Sigma(\vec{k})$ is set to the cluster self-energy $\Sigma(\vec{K})$ for momenta \vec{k} in patch P_i . However, it is important to realize that Eq. (2.11) allows for a more general approximation of the lattice $\Sigma(\vec{k})$, which, for example, can retain its smooth momentum dependence instead of the DCA step function character. To proceed, it is convenient for our purposes to express the free energy as a functional of the self-energy. By following the work of Potthoff [79, 78], we eliminate the Green's function G in favor of the self-energy Σ to write the free energy as a functional of the self-energy Σ ,

$$\Omega[\Sigma] = -\text{Tr} \ln[-(G_0^{-1} - \Sigma)] + (\mathcal{L}\Phi)[\Sigma]. \quad (2.12)$$

Here, the functional $(\mathcal{L}\Phi)[\Sigma]$ is obtained from $\Phi[G]$ through a Legendre-transformation

$$(\mathcal{L}\Phi)[\Sigma] = \Phi - \text{Tr}[\Sigma G]. \quad (2.13)$$

Replacing $\Sigma(\vec{k})$ in $(\mathcal{L}\Phi)[\Sigma]$ with the coarse-grained self-energy in Eq. (2.11), i.e. $\Sigma(\vec{k}) \approx \sum_{\vec{K}} \varphi_{\vec{K}}(\vec{k}) \bar{\Sigma}_{\vec{K}}$, then yields

$$(\mathcal{L}\Phi)[\Sigma] = \Phi - \sum_{\vec{K}} \bar{\Sigma}_{\vec{K}} \bar{G}_{\vec{K}}, \quad (2.14)$$

where $\bar{G}_{\vec{k}}$ is the coarse-grained Green's function defined in Eq. (2.6). If this functional is used in the free energy in Eq. (2.12), one obtains at stationarity, $\delta\Omega[\Sigma]/\delta\Sigma = 0$,

$$[G_0^{-1}(\vec{k}) - \Sigma(\vec{k})]^{-1} = \sum_{\vec{k}} \varphi_{\vec{k}}(\vec{k}) \bar{G}_{\vec{k}}. \quad (2.15)$$

Here, the right hand side follows from $\delta\bar{\Sigma}_{\vec{k}}/\delta\Sigma = \varphi_{\vec{k}}(\vec{k})$ and $(\mathcal{L}\Phi)[\bar{\Sigma}_{\vec{k}}]/\delta\bar{\Sigma}_{\vec{k}} = -\bar{G}_{\vec{k}}$. Using the identity $\int d\vec{k} \varphi_{\vec{k}}(\vec{k}) \varphi_{\vec{k}'}(\vec{k}) = \delta_{\vec{k}, \vec{k}'}$ and multiplying both sides with $\int d\vec{k} \varphi_{\vec{k}}(\vec{k})$ results in the DCA⁺ coarse-graining equation

$$\bar{G}_{\vec{k}} = \int d\vec{k} \varphi_{\vec{k}}(\vec{k}) [G_0^{-1}(\vec{k}) - \Sigma(\vec{k})]^{-1}. \quad (2.16)$$

We note that in contrast to the DCA algorithm, the lattice self-energy $\Sigma(\vec{k})$ enters in the coarse-graining step. It is related to the cluster self-energy $\Sigma_{\vec{K}}$ through Eq. (2.11), i.e. its coarse-grained result must be equal to $\Sigma(\vec{K})$. The special choice $\Sigma(\vec{k}) = \sum_{\vec{K}} \varphi_{\vec{K}}(\vec{k}) \Sigma_{\vec{K}}$ satisfies this requirement and recovers the DCA algorithm. But in general, $\Sigma(\vec{k})$ needs to only satisfy Eq. (2.11), i.e. one has more freedom in determining a lattice self-energy $\Sigma(\vec{k})$ from the cluster $\Sigma(\vec{K})$. In the DCA⁺ algorithm, we take advantage of this freedom to derive a $\Sigma(\vec{k})$ that retains a smooth \vec{k} -dependence and thus is more physical than the piecewise constant $\Sigma(\vec{k})$ of the DCA. As in the DCA, the cluster self-energy $\Sigma_{\vec{K}}$ may be determined from the solution of an effective cluster problem described by $(\mathcal{L}\Phi)[\Sigma]$ as a functional of the coarse-grained propagator $\Sigma[\vec{K}] = \Sigma[\bar{G}(\vec{K})]$. This, together with Eqs. (2.11) and (2.16) form the basis of the DCA⁺ algorithm.

A detailed description of the algorithm will be given in the implementation section. Evidently, determining the lattice self-energy $\Sigma(\vec{k})$ from the cluster self-energy $\Sigma_{\vec{K}}$ through inversion or deconvolution of Eq. (2.11) presents a difficult task.

2.2.2 Structure of a DCA⁺ cluster-calculation:

Since the lattice self-energy $\Sigma(\vec{k})$ no longer is restricted to Eq. (2.1), it can be expanded into an arbitrary set of smooth basis functions $\{\mathcal{B}_i(\vec{k})\}$, such as cubic splines or crystal harmonics, i.e.

$$\Sigma(\vec{k}) = \sum_i \mathcal{B}_i(\vec{k}) \sigma_i. \quad (2.17)$$

Here, σ_j are the expansion coefficients of the lattice self-energy corresponding to the basis-function $\mathcal{B}_j(\vec{k})$. Contrary to the DCA, the coarse-graining

patches $\varphi_{\vec{k}}(\vec{k})$ in the DCA^+ are not linked in any shape or form to the basis functions in which we expand the lattice self-energy. As was mentioned in the previous section, the DCA^+ maps the full lattice problem into a cluster impurity problem embedded into a mean field by coarse-graining both the lattice self-energy and lattice Green's function. The cluster-mapping in the DCA^+ is thus very similar to the cluster-mapping in the DCA, with the exception that we use a continuous lattice self-energy in the coarse-graining of the Green's function

$$\begin{aligned}\bar{\Sigma}_{\vec{k}} &= \frac{N_c}{V_{BZ}} \int_{BZ} d\vec{k} \varphi_{\vec{k}}(\vec{k}) \Sigma(\vec{k}), \\ \bar{G}_{\vec{k}} &= \frac{N_c}{V_{BZ}} \int_{BZ} d\vec{k} \varphi_{\vec{k}}(\vec{k}) \left[[G^0(\vec{k})]^{-1} - \Sigma(\vec{k}) \right]^{-1}.\end{aligned}\quad (2.18)$$

Eq. (2.18) can now be simplified by using the explicit expansion of the lattice self-energy in Eq. (2.17)

$$\bar{\Sigma}_{\vec{k}_i} = \sum_j \underbrace{\left(\int d\vec{k} \varphi_{\vec{k}_i}(\vec{k}) \mathcal{B}_j(\vec{k}) \right)}_{= P_{ij}} \sigma_j. \quad (2.19)$$

Here, $P_{i,j}$ is a projection operator, defined by coarse-graining the basis function \mathcal{B}_j over patch i . Note that in the DCA, this projection operator becomes the identity-operation $\delta_{i,j}$. Hence, the coarse graining of the lattice self-energy in the DCA is an implicit operation ($\sigma_i \equiv \bar{\Sigma}_{\vec{k}_i}$), while in the DCA^+ it becomes explicit.

With the introduction of the cluster-mapping in the DCA^+ in Eq. (2.19), the lattice mapping is conceptually well defined as long as the inverse of the projection-operator P exists. Assuming that P^{-1} exists, we can retrieve the expansion coefficients of the lattice self-energy from the self-energy of the cluster-solver $\Sigma_{\vec{k}}$ in a straightforward manner

$$\sigma_j = \sum_i (P^{-1})_{ij} \Sigma_{\vec{k}_i}. \quad (2.20)$$

This closes the DCA^+ iteration and allows us to carry out a self-consistent calculation.

In Fig. 2.3, we have summarized the generic structure of the DCA^+ algorithm, without specifying yet any implementation details of the lattice-mapping. In the "cluster-mapping" step, the lattice Green's function and

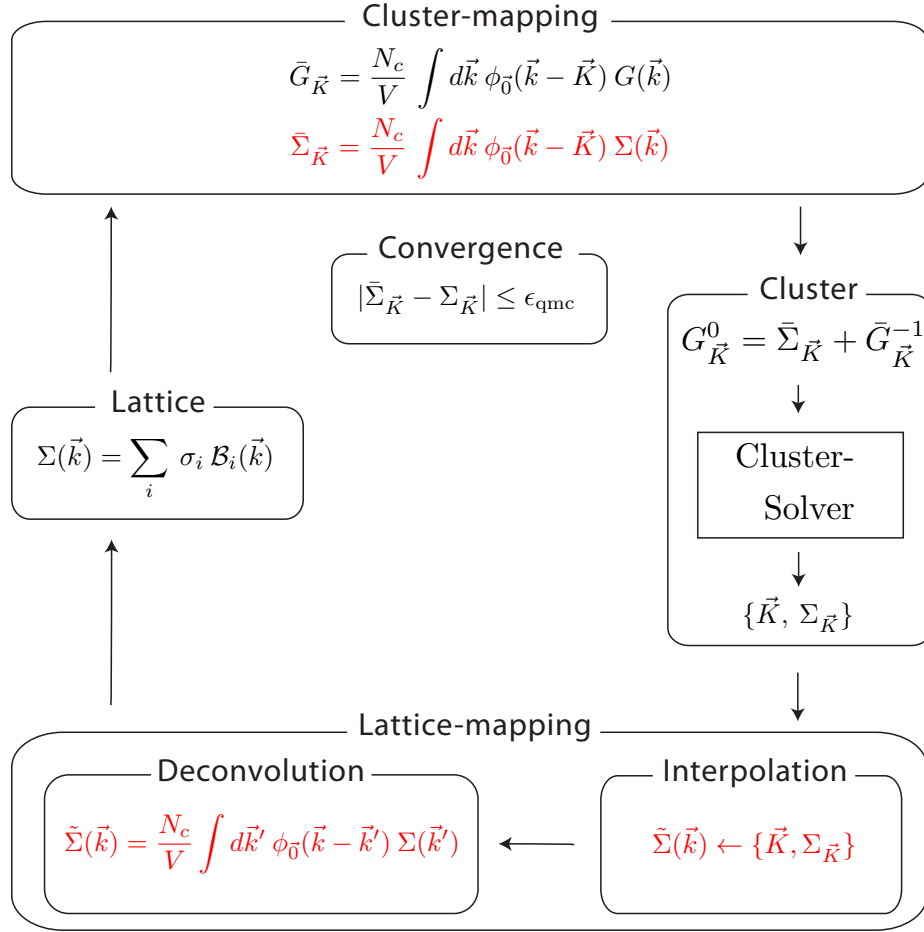


Figure 2.3: The generic structure of a self-consistent DCA⁺ algorithm, in which the cluster- and lattice-mapping play a central role in order to connect the continuous lattice self-energy $\Sigma(\vec{k})$ with the cluster self-energy $\Sigma_{\vec{K}}$. Convergence is reached when the cluster-solver produces a cluster self-energy $\Sigma_{\vec{K}}$ equal to the coarse-grained self-energy $\bar{\Sigma}_{\vec{K}} \equiv \bar{\Sigma}(\vec{K})$.

self-energy are coarse-grained onto the patches defined by $\Phi_{\vec{K}}(\vec{k})$ to give $\bar{G}_{\vec{K}}$ and $\bar{\Sigma}_{\vec{K}}$, respectively. A cluster solver algorithm such as QMC is then used to calculate, from the corresponding bare Green's function $G_{0,\vec{K}}$, the interacting Green's function and self-energy $\Sigma_{\vec{K}}$ on the cluster. In the "lattice-mapping step", which is missing in the standard DCA algorithm, a new estimate for the lattice self-energy $\Sigma(\vec{k})$ is then computed through inversion of the projection operator $P_{i,j}$. The lattice self-energy then enters the next cluster-mapping step via the lattice Green's function $G(\vec{k})$. In the implementation section of this paper, we will describe in detail how the lattice-mapping can

be done in a numerically stable way.

Due to the distinction between the lattice and cluster self-energy in the DCA^+ algorithm, we can not use the convergence criteria of the DCA. In the latter, convergence is reached if the self-energy (lattice or cluster) of the previous iteration is equal to the current one. If one monitors only convergence on the lattice self-energy in the DCA^+ algorithm, one might stop the iterations although the cluster solver still produces a cluster self-energy $\Sigma_{\vec{K}}$ that differs from the coarse-grained lattice self-energy $\bar{\Sigma}(\vec{K})$. This would indicate that the DCA^+ does not converge to a stationary point of the free energy functional Ω . To avoid such a problem, we demand that convergence is reached only when the coarse-grained lattice self-energy $\bar{\Sigma}(\vec{K})$ and the cluster self-energy $\Sigma_{\vec{K}}$ agree to within the Monte Carlo sampling error.

It is important to note that the proposed algorithm is fundamentally different from a simple interpolation of the cluster self-energy $\Sigma_{\vec{K}}$ between the cluster momenta \vec{K} . A smooth interpolation will almost certainly fail to satisfy Eq. (2.11), i.e. the main requirement of the DCA^+ that the coarse-grained lattice $\Sigma(\vec{k})$ is equal to the cluster $\Sigma_{\vec{K}}$. Such a procedure was proven in Ref. [34] to lead to causality violations when the cluster self-energy is added back to the inverse coarse-grained propagator in the "cluster exclusion" step to avoid overcounting of self-energy diagrams. In the DCA^+ , the lattice self-energy is different from an interpolated cluster self-energy and the self-energy that enters the cluster exclusion step is given by the coarse-grained lattice self-energy. Because of this, the proof given in Ref. [34] does not apply and the DCA^+ algorithm is not automatically plagued by causality problems. Although we do not have a rigorous proof that the DCA^+ algorithm remains causal, we have never encountered any causality violations in the application of this method to the single-band Hubbard model.

2.2.3 Analysis of the projection operator $P_{i,j}$ and its connection to the locality of $\Sigma(\vec{k})$:

From the previous subsection it follows that the projection operator $P_{i,j}$ plays a central role in the implementation of the DCA^+ algorithm. In order to obtain a self-consistent algorithm, it is conceptually clear that the projection operator has to be invertible. In practice, however, this might not be so easily achieved. In this section, we give the reader an intuitive understanding for this operator and show that its inverse exists if the DCA locality assumption is satisfied for the lattice self-energy. Furthermore, we discuss how the projection operator $P_{i,j}$ is influenced by the choice of the cluster.

To this end, we expand the lattice self-energy in terms of cubic Hermite splines [45]. These functions form a basis for cubic splines and obey a con-

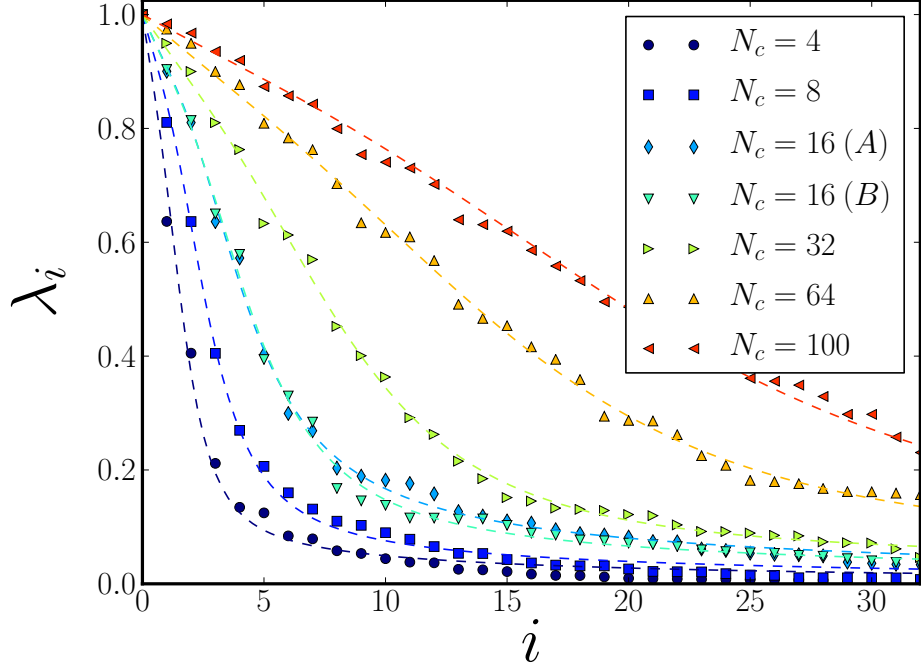


Figure 2.4: The leading eigenvalues of various clusters on a fine mesh of 512 points. We can clearly observe a strong decay of the leading eigenvalues for small clusters, which becomes weaker with increasing the cluster-size. This observation explains the intuitive notion that large clusters can describe finer features in the self-energy, since the image-space of larger clusters contains more eigenvectors.

volution property. The lattice self-energy can therefore be written as sum over a very fine mesh $\{\vec{k}_i\}$ in momentum space.

$$\Sigma(\vec{k}) = \sum_{\vec{k}_i} \sigma_{\vec{k}_i} \mathcal{H}(\vec{k} - \vec{k}_i) \quad \text{with} \quad \Sigma(\vec{k}_i) = \sigma_{\vec{k}_i} \quad (2.21)$$

It has to be stressed that choosing Hermite splines as a basis will not influence the conclusions we obtain here and thus does not reduce the generality of our arguments. It just simplifies the discussion, since the expansion index i can now be identified with a lattice momentum \vec{k}_i in the fine lattice mesh and the expansion coefficient σ_i with the lattice self-energy at that lattice momentum \vec{k}_i . Next, we generalize the cluster-mapping in Eq. (2.19), by replacing the cluster momentum points $\{\vec{K}_i\}$ by the fine lattice $\{\vec{k}_i\}$. The

coarse-graining then becomes a convolution of the lattice self-energy with the patches and we obtain

$$\bar{\Sigma}_{\vec{k}_i} = \sum_j \sigma_{\vec{k}_j} \underbrace{\int d\vec{k} \varphi_0(\vec{k} - \vec{k}_i) \mathcal{H}(\vec{k} - \vec{k}_j)}_{=P_{\vec{k}_i, \vec{k}_j}}. \quad (2.22)$$

The projection-matrix $P_{\vec{k}_i, \vec{k}_j}$ has now become a symmetric, square matrix. The latter allows us to do a spectral decomposition of $P_{\vec{k}_i, \vec{k}_j}$ into its eigenspace. If we represent its eigenvalues by λ and its corresponding eigenvector by e_λ , we obtain

$$\bar{\Sigma}_{\vec{k}_i} = \sum_j \sigma_{\vec{k}_j} \sum_\lambda \lambda e_\lambda(\vec{k}_i) \times e_\lambda^T(\vec{k}_j) \quad (2.23)$$

In terms of the eigenspace of the projection-operator, the cluster- and lattice-mapping can now be written as

$$\begin{aligned} \text{cluster-mapping: } \bar{\Sigma}_{\vec{k}_i} &= \sum_\lambda \lambda \langle \sigma_{\vec{k}_j}, e_\lambda(\vec{k}_j) \rangle e_\lambda(\vec{k}_i) \\ \text{lattice-mapping: } \sigma_{\vec{k}_i} &= \sum_\lambda \lambda^{-1} \langle \bar{\Sigma}_{\vec{k}_j}, e_\lambda(\vec{k}_j) \rangle e_\lambda(\vec{k}_i) \end{aligned} \quad (2.24)$$

Here, the inner-product $\langle \vec{a}, \vec{b} \rangle$ is represented by a simple dot-product between the two vectors \vec{a} and \vec{b} . From Eqs. (2.24), it is clear that the spectrum $\{\lambda\}$ of the projection-operator P_{ij} plays a central role in the cluster- and lattice mapping. In Fig. 2.4, we show the leading eigenvalues (i.e. having the largest absolute value) of $P_{i,j}$ for various clusters. One can clearly observe that all eigenvalues are smaller or equal than one and decay rapidly for small clusters ($N_c \leq 8$) and slowly for large clusters ($N_c \geq 32$). This can be easily understood from the form-factor of the patches. The latter are very similar to box-car filters, which are one of the most common low-pass filters used in the field of signal processing. Since the coarse-graining of the lattice self-energy in Eq. (2.22) can be rewritten as a convolution with the patches, the projection operator $P_{i,j}$ will in fact reduce all the Fourier components during the convolution, insuring that the L_2 -norm of any function in the eigenspace never grows. Consequently, this is also true for all eigenvectors, which leads us to conclude that the eigenvalues have to be less or equal to 1.

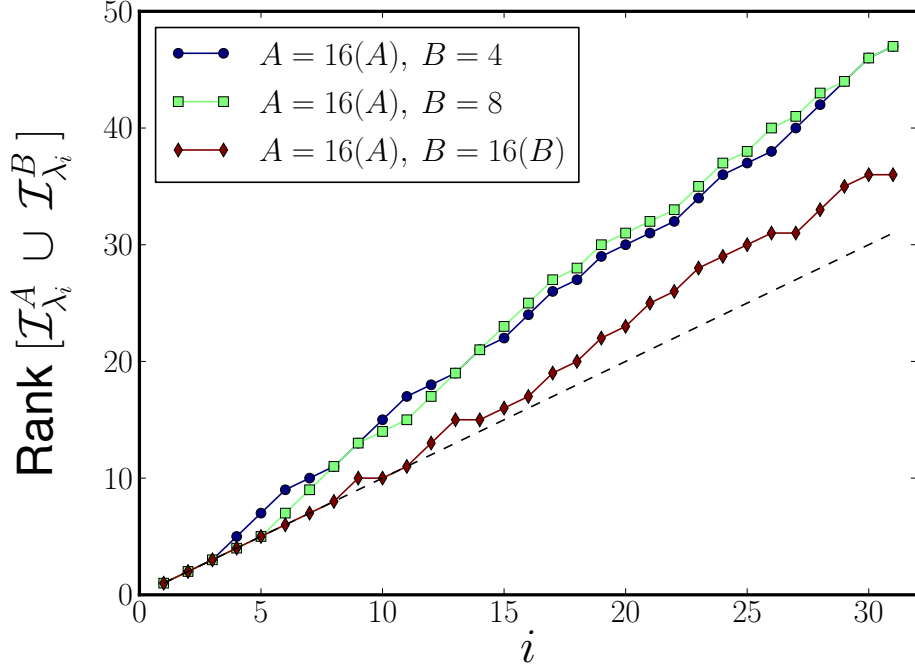


Figure 2.5: The dimension of the union image space $\mathcal{I}_{\lambda_i}^A \cup \mathcal{I}_{\lambda_i}^B$ for two different clusters A and B versus the eigenvalue index i . Since the rank of $\mathcal{I}_{\lambda_i}^A$ and $\mathcal{I}_{\lambda_i}^B$ both equal i , any deviation of the rank for the space $\mathcal{I}_{\lambda_i}^A \cup \mathcal{I}_{\lambda_i}^B$ from i indicates that the projection operators of clusters A and B span different image spaces. One can clearly observe that the differentiation of the 16A site cluster eigenspace with smaller clusters occurs faster.

Using the spectral decomposition of the projection-matrix, we can split the representation space of the continuous lattice self-energy into the image-space \mathcal{I} and the kernel-space \mathcal{K} of the projection operator $P_{i,j}$. Since our projection-operator does not follow the strict mathematical definition of a projection operator¹, we define the image \mathcal{I}_ε as the space spanned by the eigenvectors that have an eigenvalue larger than ε . Here, ε is a small, positive cut-off parameter. The kernel \mathcal{K}_ε contains the remainder of the space, and is thus spanned by the eigenvectors with an eigenvalue smaller than ε . Due to the inversion of the eigenvalue in Eq. (2.24), the lattice-mapping is only well-defined on the image-space \mathcal{I}_ε . This brings us to the first important observation. In order to do a self-consistent DCA⁺ calculation, the coarse-grained lattice self-energy should always be entirely defined on the image-space \mathcal{I}_ε of our projection operator. Otherwise, there exists no well-defined

¹A projection operator should satisfy the relationship $P^2 = P$. The eigenvalues of such an operation can only be 0 and 1.

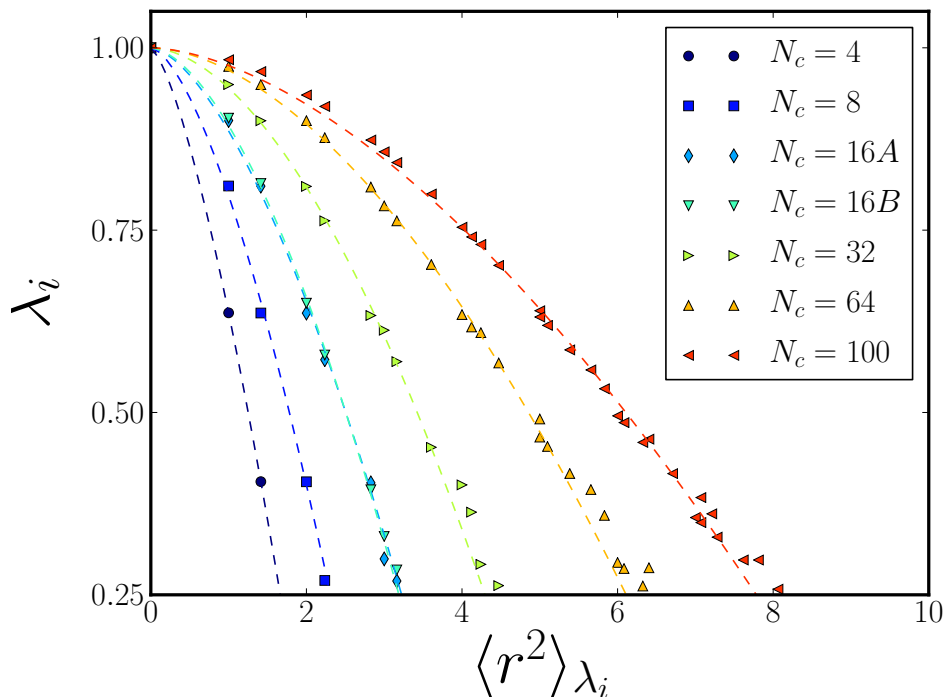


Figure 2.6: The correlation between the magnitude of the leading eigenvalue and the delocalization of its corresponding eigenvector for various clusters.

transformation that maps the cluster self-energy back into the lattice self-energy, which in turn breaks the DCA^+ self-consistency loop. Notice that this requirement holds trivially in the case of the traditional DCA, since in that case the projection matrix is simply the identity-matrix of size N_c , and all eigenvalues are equal to one.

Eq. (2.23) can also explain how the geometry of the patches will influence the results obtained with the DCA^+ . In Fig. 2.5, we plot the union space of the image spaces $\mathcal{I}_{\lambda_i}^A$ and $\mathcal{I}_{\lambda_i}^B$ versus eigenvalue index i for different clusters. The plot shows very clearly that the first leading eigenvectors are equal to each other, and gradually diverge as eigenvectors with smaller eigenvalues are added. This brings us to the second observation. If one wants to carry out a DCA-calculation with results that are independent of cluster shape, the cluster self-energy has to be representable on the intersection of the image-spaces \mathcal{I}_ε of both clusters.

So far, we have only discussed and introduced strict geometrical criteria on the lattice and cluster self-energy, that indicate when a DCA^+ cluster calculation is feasible. In order to link geometrical criteria to physics, we

show in Fig. 2.6 the delocalization of the leading eigenvectors $\langle r^2 \rangle$. Formally, we define the delocalization as

$$\langle r^2 \rangle_\lambda = \sqrt{\frac{\sum_{\vec{r}} e_\lambda^T(\vec{r}) r^2 e_\lambda(\vec{r})}{\sum_{\vec{r}} e_\lambda^T(\vec{r}) e_\lambda(\vec{r})}}. \quad (2.25)$$

At close inspection, we can see a clear correlation between the absolute value of the leading eigenvalues λ and the delocalization of its corresponding eigenvector for all cluster sizes. This correlation shows that the space \mathcal{I}_ϵ is actually spanned by the eigenvectors with a small delocalization. As a result, satisfying the geometric criteria to do a self-consistent DCA⁺ calculation is essentially equivalent to satisfying the DCA-assumption of locality for the lattice self-energy. Another important conclusion that can be drawn from Fig. 2.6 is that the number of vectors that span the space $\mathcal{I}_{\epsilon=0.25}$ becomes larger with increasing cluster size. This correlation reflects the intuitive notion in the DCA that larger clusters can describe finer features of the lattice self-energy.

2.2.4 Role of the cluster in the DCA⁺

In the DCA algorithm, the real space cluster takes a central role. It completely defines the basis-functions in which the self-energy is expanded. Furthermore, the real space cluster dictates how the lattice is mapped on the cluster through the coarse-graining procedure. Consequently, solutions obtained with the DCA algorithm usually dependent on the particular choice (shape) of the cluster. In practice, this leads to a very good qualitative description of the physics, but prohibits quantitative analysis, as calculated physical quantities strongly depend on cluster shape. In the DCA⁺, we start from an expansion of the self-energy into an arbitrary set of basis-functions. In this way, the influence of the real space cluster is reduced, since it does not dictate the basis-functions on which the self-energy is expanded. The real space cluster only specifies how the cluster is mapped on the lattice through the shape of the coarse-graining patches. Consequently, the focus in the DCA⁺ shifts from the real space cluster to the projection operator $P_{i,j}$. This operator embodies the quantum cluster approximation of the DCA⁺, since it connects the cluster self-energy with the lattice self-energy in a purely geometric way. The projection operator is only defined by the set of basis-functions of the lattice self-energy and the real space cluster and not subjected in any way to physical parameters (such as temperature, band-structure, interaction terms, ...). This purely 'geometric' property of the projection operator allows us to find a priori the necessary conditions to which the cluster self-energy has to be subjected, in order to allow for a self-consistent, cluster-independent DCA⁺ calculation. These necessary conditions that follow from the discussion in the previous subsections are:

- In order to perform a self-consistent DCA⁺ calculation, the cluster self-energy has to converge in the image-space \mathcal{I}_ε of the projector.
- In order to perform a cluster-independent DCA⁺ calculation on the cluster A and B , the cluster self-energy needs to converge on the intersection of the image-spaces of both projectors ($\mathcal{I}_\varepsilon^A \cap \mathcal{I}_\varepsilon^B$).

2.3 Implementation of the self-consistent loop.

In the last section, we have introduced a projection operator $P_{i,j}$ and shown its involvement in the cluster and lattice-mapping. Via a geometric consideration, we have shown conceptually that its inverse exists as long as the expansion coefficients $\langle \bar{\Sigma}_{\vec{k}}, e_\lambda(\vec{k}) \rangle$ of the cluster self-energy vanish rapidly in the image-space \mathcal{I}_ε of the projection operator $P_{i,j}$. At closer inspection, the lattice mapping is thus a two stage process. First, we need to determine the expansion coefficients of the cluster self-energy. To this end, we will propose a novel interpolation technique, which is motivated from the analytical properties of the self-energy. The interpolated cluster self-energy $\bar{\Sigma}_{\vec{k}_j}$ is then used to compute the inner product $\langle \bar{\Sigma}_{\vec{k}_j}, e_\lambda(\vec{k}_j) \rangle$ with the eigenfunctions of the projection operator $P_{i,j}$, which gives the expansion coefficients of the cluster self-energy. Secondly, we need to deconvolute the interpolated cluster self-energy on the image space \mathcal{I}_ε , where we need to determine the optimal value for the parameter ε . If the latter is too large, the self-consistency can not be reached. If ε is too small, the lattice-mapping will become numerically unstable due to the division of small eigenvalues. To solve this problem, we adapt the Richardson-Lucy deconvolution algorithm, which inverts Eq. (2.22) in a numerically stable way.

2.3.1 Interpolation

In the context of tight-binding models, one of the most successful algorithms to interpolate its band structure is the Wannier-interpolation-method [64]. It finds its justification in the localized nature of Wannier orbitals, from which the tight-binding models are derived. Since the self-energy is a correction to the band-structure due the interaction between the electrons, the Wannier interpolation method seems a suitable interpolation algorithm. Okamoto et al. [75] have examined this possibility implicitly, by expanding the lattice self-energy $\Sigma(\vec{k})$ into the cubic-harmonic basis-functions $\{C_{\vec{k}}(\vec{k})\}$.

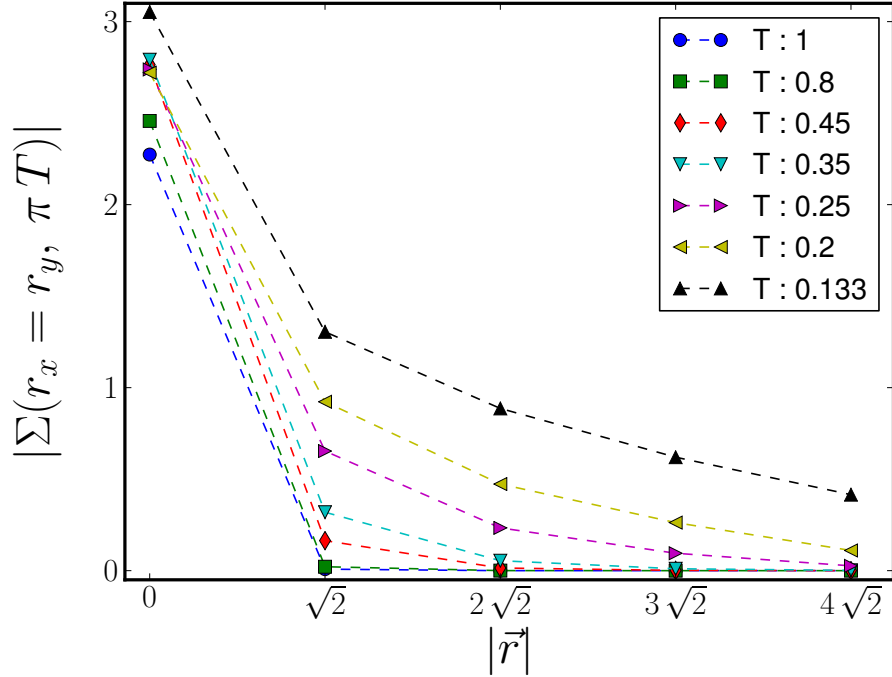


Figure 2.7: The decay of Σ_R for a $N_c = 100$ -site cluster with $U/t = 7$ and $t'/t = 0$ for various temperatures at half filling. For high temperatures ($T \leq 0.3$), the system is only weakly correlated and Σ_R will rapidly decay. For low temperatures, the correlations exceed the cluster-radius $R_c = 5$.

$$\begin{aligned}\Sigma(\vec{k}) &= \sum_{\vec{K}} C_{\vec{K}}(\vec{k}) \Sigma_K \\ C_{\vec{K}}(\vec{k}) &= \frac{1}{N_c} \sum_{\vec{R}} e^{i\vec{R}(\vec{K}-\vec{k})}\end{aligned}\quad (2.26)$$

This approach only works when the self-energy $\Sigma_{\vec{K}}$ is sufficiently smooth, such that the real-space self-energy $\Sigma_{\vec{R}}$ converges on the cluster in real space. Notice that the latter is implicitly computed in Eq. (2.26), since

$$\Sigma(\vec{k}) = \sum_{\vec{K}} C_{\vec{K}}(\vec{k}) \Sigma_{\vec{K}} = \sum_{\vec{R}} e^{-i\vec{R}\vec{k}} \underbrace{\frac{1}{N_c} \sum_{\vec{K}} e^{i\vec{R}\vec{K}} \Sigma_{\vec{K}}}_{=\Sigma_{\vec{R}}}.$$

The sum over all lattice points can now be split into two terms. In the first term, we run over all lattice-points within the cluster-radius. In the second term, we sum over all the remaining points in the lattice.

$$\begin{aligned}
 \Sigma(k) &= \sum_{\vec{R}} e^{-i\vec{R}\vec{k}} \Sigma_{\vec{R}} \\
 &= \sum_{|\vec{R}| < R_c} e^{-i\vec{R}\vec{k}} \Sigma_{\vec{R}} + \sum_{|\vec{R}| \geq R_c} e^{-i\vec{R}\vec{k}} \Sigma_{\vec{R}}
 \end{aligned} \tag{2.27}$$

If correlations have longer range, $\Sigma_{\vec{R}_i}$ will no longer converge on the cluster in real space. This is clearly illustrated in Fig [2.7], where we show the self-energy $\Sigma_{\vec{R}}$ for a $N_c = 100$ -site cluster with $U/t = 7$ for various temperatures. At high temperatures ($T \geq 0.25$), the system is only weakly correlated. The self-energy $\Sigma_{\vec{R}}$ in this temperature range is contained within the cluster-radius $R_c = 5$. For lower temperatures, it is clear that $\Sigma_{\vec{R}}$ extends beyond R_c . Applying the Wannier interpolation scheme according to Eq. (2.26) to such correlated systems is simply not allowed, since the expansion coefficients $\Sigma_{\vec{R}}$ outside the cluster can not be assumed to be zero. A straightforward application of Eq. (2.26) will lead to ringing and eventually to causality violations. The latter was observed by Okamoto et al. [75], and could only partially be resolved by introducing low-pass filtering schemes. The applicability of this approach is very limited, due to a lack of a general framework to determine these filters.

Formalism of the interpolation:

From the previous section, it has become clear that the interpolation techniques such as Eq. (2.26) can only work if the function converges on the finite (and often small) basis-set. The rate of convergence depends critically on the choice of the basis-functions. Consider for example the free Green's function G^0 of the single band Hubbard model:

$$G^0(\vec{k}, \omega) = [i\omega - \varepsilon(\vec{k})]^{-1}. \tag{2.28}$$

While this Green's function G^0 will converge poorly on the cubic-harmonics of the lattice for small frequency ω , it is straightforward to see that $[G^0]^{-1}$ will be completely converged on a 4-site cluster. This simple example shows how one can extend the interpolation-idea introduced by Okamoto et al [75]. Given an injective transformation \mathcal{T} , we can write

$$\begin{aligned}
 \mathcal{F}(\vec{k}) &= \mathcal{T}^{-1} \left[\mathcal{T}[\mathcal{F}](\vec{k}) \right] \\
 &= \mathcal{T}^{-1} \left[\sum_{\vec{R}} C_{\vec{R}}(\vec{k}) \mathcal{T}[\mathcal{F}_{\vec{R}}] \right]
 \end{aligned} \tag{2.29}$$

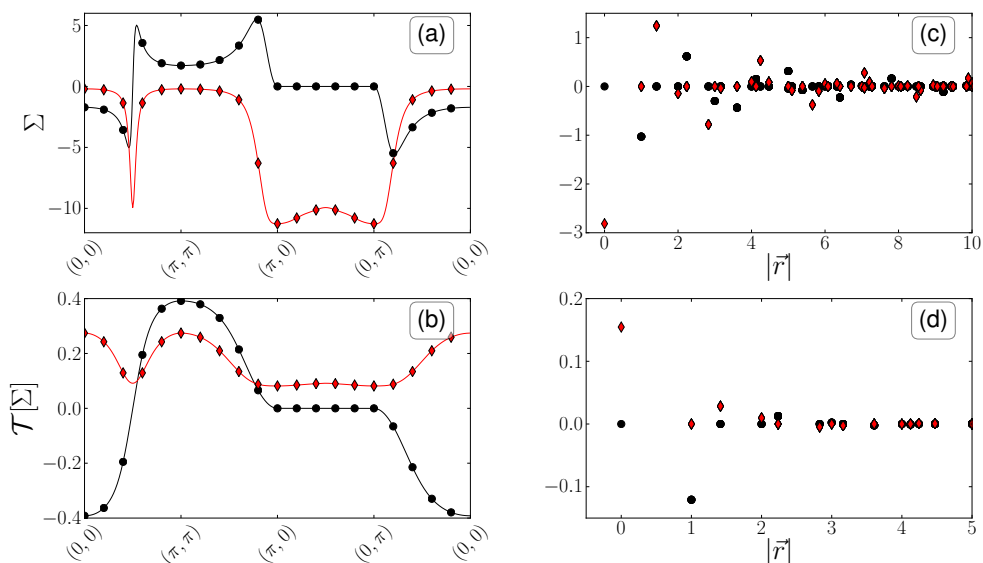


Figure 2.8: Interpolation-procedure for the self-energy Σ_K at the lowest Matsubara frequency for a 100-site cluster at a temperature $T = 0.2$, $U/t = 7$ and $t' = 0$ at half-filling. (A) The interpolated function $\Sigma(\vec{k})$ is a smooth function through the results Σ_K obtained from the QMC cluster solution, where the circles and diamonds represent respectively the real and imaginary part. (B) The transformed function $\mathcal{T}[\Sigma]$ smoothes the self-energy function, making it suitable for a cubic harmonics expansion. (C) The Fourier transform of the interpolated function $\Sigma(k)$. Notice that the tails expand much further than the cluster-radius $R_c = 5$. (D) The Fourier transform of the function $\mathcal{T}[\Sigma_K]$. The convergence is reached at $R_c = 3$.

The method of operation to interpolate a function becomes now clear. Find an injective (and preferably analytical) transformation \mathcal{T} , such that the transformed function-values converge on the chosen basis-functions. Use this expansion to compute the transformed function-values on arbitrary k-points. Finally, apply the inverse transformation \mathcal{T}^{-1} on the transformed function-values in order to obtain the desired interpolated function-values on arbitrary k-points.

This approach has many advantages. First, it provides a measure that indicates when the interpolation-procedure works or fails. If $\mathcal{T}[\Sigma_{\vec{k}}]$ does not converge on the basis-set, one is not allowed to perform an interpolation. Second, this interpolation-procedure does not introduce *extra information* – filtering schemes and other numerical tricks to ensure causality, on the other hand, introduce extra, undesirable structure into the interpolated functions. By using filtering schemes or other numerical tricks to assure causality, we

introduce extra structure in the function that is to be interpolated, which is undesirable. Third, if the transformation \mathcal{T} is analytical, we will not break the analyticity of the interpolated function. For Green's functions and their derived functions such as the self-energy, analyticity is an important property. In arbitrary interpolation schemes such as splines [19] or radial-basis expansions [16], this analyticity is often broken. The obtained interpolating function is therefore questionable from a physics-point of view. The challenge of this approach is naturally the search for a correct transformation \mathcal{T} . Notice that \mathcal{T} can be different for different functions, since the only requirements are injectivity and convergence on the chosen basis-set. In the next subsections, we will propose such a transformations for the self-energy Σ . The proposed transformation will be motivated by physical and analytical properties of the self-energy.

Interpolation on large clusters:

Since the imaginary part of the self-energy is strictly negative in the upper-half of the complex-plane [1]

$$\text{Im}[\Sigma(\vec{k}, i\omega > 0)] < 0. \quad (2.30)$$

we can introduce an injective transformation \mathcal{T} that preserves the analyticity of the self-energy²,

$$\mathcal{T}(\Sigma) = [\Sigma - \alpha i]^{-1}, \text{ with } \alpha > 0. \quad (2.31)$$

Due to the property shown in (2.30), the transformation \mathcal{T} will map the self-energy Σ into a bounded function, irrespective of how spiky the self-energy Σ is. Notice also that we first shift the imaginary part of the self-energy down by αi , in order to avoid introducing poles due to the Monte Carlo statistical noise. Consequently, the function $\mathcal{T}(\Sigma)$ will now be localized in real space, and we can safely perform an expansion of the function $\mathcal{T}(\Sigma)$ over cubic harmonics. We have illustrated this process in Fig. 2.8, by applying our interpolation procedure to a 100-site cluster at a temperature $T = 0.2$ at half filling. In (A), we show respectively the computed values of the cluster self-energy $\Sigma_{\vec{k}}$ and its interpolation $\Sigma_{\vec{k}}$ along a high-symmetry line in the Brillouin-zone. Notice that the imaginary part of the interpolation function remains at all times negative! In (B), the transformed function $\mathcal{T}[\Sigma_{\vec{k}}]$ is shown, together with its interpolating function. Clearly, the transformation \mathcal{T} has reduced the sharp features in the self-energy, and the function has become smoother. In (C) and (D), we show the Fourier transform from

²Since $\text{Im}[\Sigma(\vec{k}, \omega)] < 0$, we will not introduce any new poles in the upper-half plane by inverting the function.

respectively the interpolated self-energy $\Sigma(\vec{k})$ and the transformed values $\mathcal{T}[\Sigma_{\vec{k}}]$. The large difference in the convergence radii is clear, and shows the effectiveness of our indirect approach compared to a direct one. This result is not a coincidence. In the appendix, we have proven in a rigorous way the point-wise convergence.

Interpolation on small clusters:

For certain parameter sets, the fermionic sign problem prevents the investigation of large enough clusters, for which $\mathcal{T}[\Sigma]$ will converge. In this case, we recommend to interpolate the $\mathcal{T}[\Sigma]$ using cubic splines, instead of interpolating the latter with the earlier proposed Wannier-interpolation. Since $\mathcal{T}[\Sigma]$ is a much smoother function, cubic splines can still perform reasonably well, even in the case of small clusters. The self-energy on the other hand will not be smooth, and a straightforward spline interpolation will lead to overshoots or ringing, which in turn might lead to an acausal self-energy. This particular phenomenon has been studied extensively by Okamoto et al [75]. The ringing might be cured by the use of tension splines [18], in which case a tension parameter is introduced. It is however important to keep in mind that the splines might add extra information into the system, and thus bias the physics. This problem does not occur with Wannier interpolation, as long as the Fourier coefficients of $\mathcal{T}[\Sigma_{\vec{k}}]$ converge on the real space cluster.

lattice-symmetry:

Most of the clusters used in the DCA do generally not obey the same symmetry operations as the infinite lattice. As a consequence, the lattice-self-energy in the DCA breaks the symmetry of the lattice, due to its strict parametrization with the coarsegrain patches. The only way to resolve this issue in the DCA, is to restrict to the few clusters that obey the cluster-symmetry. In order to remove this undesirable feature in the DCA⁺, we symmetrize the self-energy after the interpolation. The interpolated cluster-self-energy obeys thus by construction the symmetry operations of the lattice.

2.3.2 Cluster Deconvolution

The goal of this section is to present a practical implementation of the lattice-mapping. As mentioned in the theoretical section of this paper, the lattice mapping is in essence the inversion of the cluster mapping defined in Eq. (2.18). In a common DCA⁺ calculation, we will have much more basis functions than Monte Carlo cluster-points. As a consequence, we need to determine more lattice expansion coefficients than cluster-points that are given by the cluster-solver. The inversion problem is thus seemingly under-determined. Therefore, we do not attempt to solve Eq. (2.18) directly, but

first generalize the coarsegraining equation of the self-energy. This is accomplished by rewriting each coarsegraining patch as a translation of the patch around the origin, i.e $\varphi_{\vec{K}}(\vec{k}) = \varphi_{\vec{0}}(\vec{k} - \vec{K})$. Next, we generalize the cluster-momentum vector \vec{K} to an arbitrary momentum vector. Using the interpolated cluster self-energy $\bar{\Sigma}_{\vec{K}}$ as a substitute for the cluster self-energy $\Sigma_{\vec{K}}$ in Eq. (2.18), we obtain

$$\bar{\Sigma}(\vec{k}) = \frac{N_c}{V} \int d\vec{k}' \varphi_{\vec{0}}(\vec{k} - \vec{k}') \Sigma(\vec{k}') \quad (2.32)$$

Any solution of Eq. (2.32) is thus also a solution of Eq. (2.18). We should stress that with the exception of the continuity of the self-energy, this generalization does not introduce any new information as long as the Wannier-interpolation converges! With Eq. (2.32), we have now rephrased the lattice-mapping into a deconvolution problem. These type of problems are regularly encountered in the field of signal theory and image processing and various algorithms have been successfully developed to address the ill-conditioned deconvolution problem [38].

The Richardson-Lucy algorithm:

One of the most common deconvolution algorithms is the Richardson-Lucy algorithm [81, 56]. The latter is based on a Bayesian inference scheme. Since the patches are strictly positive and integrate to unity, we can interpret them as a probability distribution function.

$$\forall \vec{k}, \vec{k}' : \varphi_{\vec{0}}(\vec{k} - \vec{k}') \geq 0, \quad 1 = \frac{N_c}{V_{BZ}} \int_{BZ} d\vec{k} \varphi_{\vec{0}}(\vec{k} - \vec{k}')$$

As such, we can apply Bayes theorem and construct a conditional probability \mathcal{Q} for any given lattice self-energy $\Sigma(\vec{K})$

$$\mathcal{Q}(\vec{k}|\vec{k}') = \frac{\varphi_{\vec{0}}(\vec{k}' - \vec{k}) \Sigma_{\vec{k}'}(\vec{k})}{\int_{BZ} d\vec{k}'' \varphi_{\vec{0}}(\vec{k}' - \vec{k}'') \Sigma(\vec{k}'')}. \quad (2.33)$$

We should stress at this point that conditional probability \mathcal{Q} is computed separately for the real and imaginary part of the self-energy. The conditional probability $\mathcal{Q}(\vec{k}|\vec{K})$ is then used to construct a new lattice self-energy $\Sigma'(\vec{k})$, given a continuous cluster self-energy $\bar{\Sigma}(\vec{k}')$,

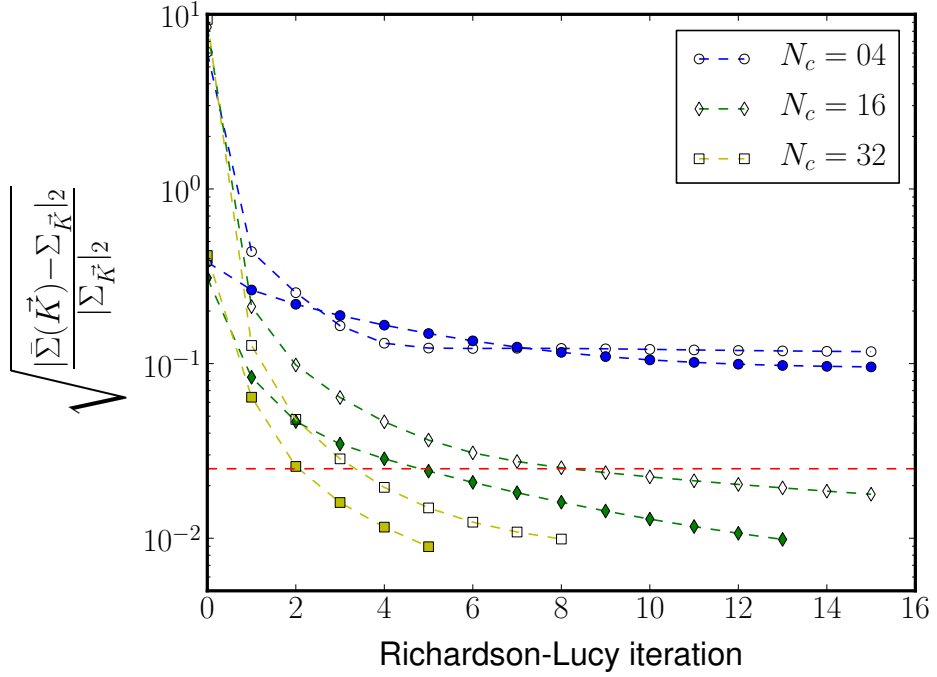


Figure 2.9: Relative error between the cluster self-energy $\Sigma_{\vec{K}}$ and the integrated lattice self-energy $\bar{\Sigma}(\vec{K})$ for the real (open symbols) and imaginary (solid symbols) part at 5% doping and $T = 0.2$.

$$\Sigma'(\vec{k}) = \int_{\text{BZ}} d\vec{k}' Q^t(\vec{k}|\vec{k}') \bar{\Sigma}(\vec{k}'). \quad (2.34)$$

The idea of the Richardson-Lucy algorithm is now to use Eq. (2.33) and Eq. (2.34) in an iterative way. After plugging both equations together, we end up with a fixed point problem

$$\Sigma(\vec{k}) \leftarrow \Sigma(\vec{k}) \int d\vec{k}' \frac{\varphi_0(\vec{k} - \vec{k}') \bar{\Sigma}(\vec{k}')}{\int d\vec{k}'' \varphi_0(\vec{k}' - \vec{k}'') \Sigma(\vec{k}'')}. \quad (2.35)$$

If the interpolated function $\bar{\Sigma}(\vec{k})$ is now used as our initial guess for the lattice self-energy $\Sigma(\vec{k})$, Eq. (2.35) provides us with a simple implementation for the lattice-mapping. In light of the DCA⁺ algorithm, the Richardson-Lucy deconvolution algorithm has many interesting properties, that make it an ideal algorithm to be used for the deconvolution. First of all, it is a

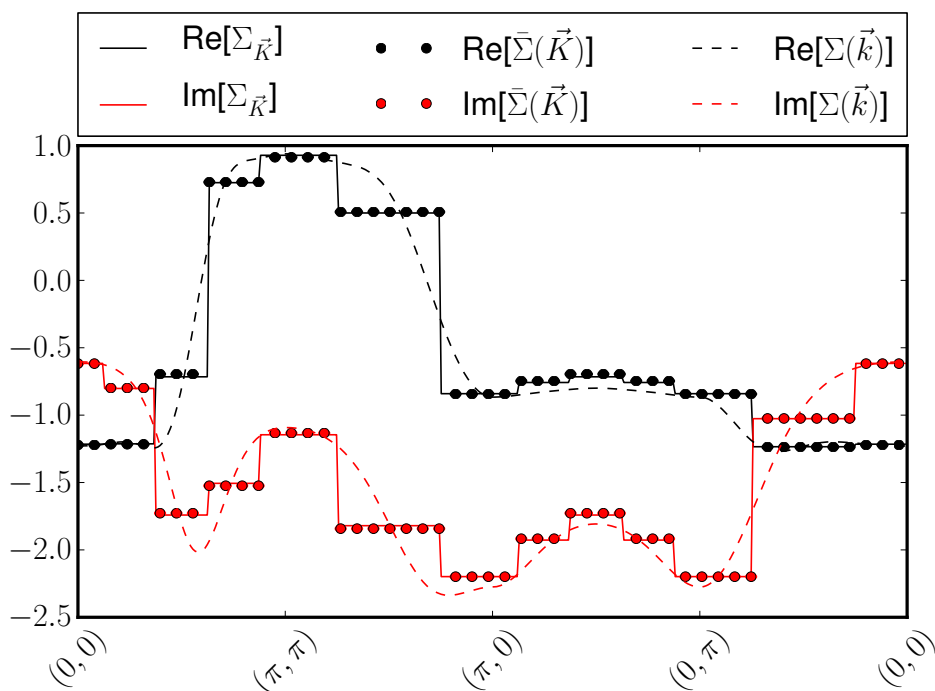


Figure 2.10: Comparison between the lattice self-energy $\Sigma(\vec{k}, \pi T)$, the cluster self-energy $\Sigma_{\vec{K}}(\pi T)$ and the coarse-grained lattice self-energy at the cluster-momenta $\bar{\Sigma}_{\vec{K}}(\pi T) \equiv \bar{\Sigma}(\vec{K}, \pi T)$ for a 32-site cluster at 5% doping and $T = 0.2$.

straightforward algorithm that does not need any extra, non-physical input. Other deconvolution algorithms, such as total variation [85, 14] introduce non-physical penalty factors to insure smoothness of the result. Secondly, the Richardson-Lucy algorithm conserves the sign of strictly positive and negative functions. This property can be easily proven in Eq. (2.35), since $\varphi_0(\vec{k})$ is strictly positive. Hence, if the initial guess for $\Sigma(\vec{k})$ and $\bar{\Sigma}(\vec{k}')$ are both positive (negative) for all momenta \vec{k} , the resulting $\Sigma(\vec{k})$ will also be positive (negative). Therefore, if the interpolated cluster self-energy $\bar{\Sigma}(\vec{k})$ is causal, the lattice self-energy will also be a causal function. Third, it has been proven that the solution of this iterative scheme converges to the maximum of the likelihood function [56]. Hence, of all lattice self-energies that generate the same cluster self-energy after the convolution (coarse-graining), the Richardson-Lucy algorithm will produce the lattice self-energy that is the most likely to reproduce the cluster self-energy.

Like all other deconvolution algorithms, the Richardson-Lucy algorithm is an approximate algorithm, meaning that the convergence to the exact solu-

tion is not guaranteed up to an arbitrary precision. This is not surprising, since we know that the convolution is invertible as long as the expansion coefficients of the cluster-self-energy in Eq. (2.24) decay faster than the eigenvalues of the projection-operator. Consequently, the smaller the cluster, the slower the Richardson-Lucy algorithm will converge to a solution and the bigger the discrepancy between the coarsegrained lattice self-energy $\bar{\Sigma}(\vec{K})$ and the cluster self-energy $\Sigma_{\vec{K}}$ obtained from the cluster-solver. This phenomenon is illustrated in Fig. 2.9, where we show the relative error in the L_2 -norm between $\bar{\Sigma}(\vec{K})$ and $\Sigma_{\vec{K}}$. The figure clearly shows that the larger cluster converges faster and that the residual error between the cluster and coarsegrained self-energy decreases with increasing cluster-size.

In a typical deconvolution, we stop the iteration process if a certain accuracy is obtained. In theory, one could use the statistical error of the Monte Carlo integration to determine the accuracy. In practice, we have found that a relative error below 2.5% delivers in most cases very good results. In Fig. 2.10, we show the lattice self-energy for a 32-site cluster, stopped at an accuracy of 2.5%. We can clearly observe that the cluster and coarse-grained lattice self-energy coincide very well.

2.4 Theory and implementation of the two-particle framework.

In this section, we present the theoretical foundation as well as a practical implementation of the two-particle framework in the DCA⁺ algorithm. Just as in the DCA, this framework is a systematic methodology, aimed at detecting the critical temperature of various kinds of phase-transitions in the lattice. Since the DCA⁺ is a natural extension of the DCA, we will first briefly revise how phase transitions are detected in the DCA, following closely the argumentation of Jarrell et. al. [39]. Next, we introduce the theoretical foundation of the two-particle framework in the DCA⁺. Starting from the diagrammatic criterium for a thermodynamic consistent algorithm $\Gamma(k_1, k_2) = \delta\Sigma(k_1)/\delta G(k_2) = \delta^2\Phi/(\delta G(k_1)\delta G(k_2))$ introduced by Baym and Kadanoff [10, 9], we derive a coarsegraining condition that links the lattice vertex function $\Gamma(k_1, k_2)$ with the cluster vertex function Γ_{K_1, K_2} . This coarsegraining condition is the two-particle equivalent of the coarsegraining condition for the self-energy in the DCA⁺. Finally, we introduce a practical, numerically stable algorithm that for a given cluster vertex generates a continuous lattice vertex, that satisfies the previously introduced two-particle coarsegraining condition.

2.4.1 Detection of phase-transitions in the DCA

The critical temperature of a second order phase transition can be accurately recorded by monitoring the divergence of the associated lattice-susceptibility over a range of temperatures. The lattice-susceptibility is obtained indirectly from the two-particle cluster Greens-functions, which are computed in the last DCA-iteration when self-consistency is reached for the self-energy. In this section, we revise how to compute lattice-susceptibilities in the DCA for the two most prominent channels, namely the particle-hole (*ph*) and particle-particle (*pp*) channel. Formally, the two-particle Greens functions in the *ph* and *pp* channel are defined as

$$\begin{aligned} G_{ph}^{Q,II}(K_1, K_2) &= \langle c_{K_1+Q}^\dagger c_{K_1} c_{K_2}^\dagger c_{K_2+Q} \rangle, \\ G_{pp}^{Q,II}(K_1, K_2) &= \langle c_{K_1+Q}^\dagger c_{-K_1}^\dagger c_{-K_2} c_{K_2+Q} \rangle. \end{aligned} \quad (2.36)$$

Here, the brackets $\langle \dots \rangle$ represent the thermal average, which in our case is obtained through a CT-AUX Quantum Monte Carlo impurity solver and a delayed NFFT measurement technique. For the symbols K and Q , we use the conventional representation [1] $K = \{\vec{K}, \omega_m\}$ and $Q = \{\vec{Q}, \nu_n\}$ where \vec{K} and \vec{Q} are the cluster momentum vectors and ω_m and ν_n are respectively the uneven and even frequencies. Since Q is a constant, we will drop the superscript Q for notational convenience. With the interacting two-particle cluster Greens function G^{II} , we can solve the cluster Bethe-Salpeter equation towards the cluster vertex function Γ_{K_1, K_2}^c . This is accomplished by inverting the matrix-representation of respectively the non-interacting and interacting two-particle cluster Greens function G^0 and G^{II} , and subsequently subtracting the inverse matrices:

$$\Gamma_{K_1, K_2}^c = [G^0]_{K_1, K_2}^{-1} - [G^{II}]_{K_1, K_2}^{-1}. \quad (2.37)$$

Here, G^0 is constructed from a pair of interacting single-particle cluster Greens-functions G^I , which are also computed in the last DCA-iteration. In accordance with Eqs. (2.36), the non-interacting two-particle Greens function is different for both channels and defined as,

$$\begin{aligned} G_{ph}^0(K_1, K_2) &= \delta_{K_1, K_2} G^I(K_1 + Q) G^I(K_2), \\ G_{pp}^0(K_1, K_2) &= \delta_{K_1, K_2} G^I(K_1 + Q) G^I(-K_2). \end{aligned} \quad (2.38)$$

Next, we compute the two-particle lattice Greens-function χ , by approximating the lattice vertex function with the cluster vertex function obtained from

Eq. (2.37). Just as the lattice self-energy in the DCA, the cluster vertex function Γ_{K_1, K_2} is expanded into the set of coarsegraining patches $\{\varphi_{\vec{K}_i}(\vec{k})\}$ in order to obtain the lattice vertex function $\Gamma(k_1, k_2)$

$$\Gamma(k_1, k_2) = \sum_{K_1, K_2} \varphi_{K_1}(k_1) \Gamma_{K_1, K_2}^c \varphi_{K_2}(k_2).$$

Similarly to the lattice self-energy in the DCA, the lattice vertex function is constant on the patches. This reduces the complexity of the lattice Bethe-Salpeter significantly, since the product of the lattice vertex function Γ with the non-interacting two-particle lattice Greens-function χ^0 can now be simplified to the product of the cluster vertex function Γ^c with the coarsegrained non-interacting two-particle lattice Greens-function $\bar{\chi}^0$. Formally, the latter is defined in both channels as

$$\begin{aligned} \bar{\chi}_{ph}^0(K_1, K_2) &= \delta_{K_1, K_2} \int d\vec{k} \varphi_{\vec{K}_1}(\vec{k}) G(\vec{k} + Q) G(\vec{k}), \\ \bar{\chi}_{pp}^0(K_1, K_2) &= \delta_{K_1, K_2} \int d\vec{k} \varphi_{\vec{K}_1}(\vec{k}) G(\vec{k} + Q) G(-\vec{k}). \end{aligned} \quad (2.39)$$

The lattice Bethe-Salpeter equation can now be solved towards the two-particle lattice Greens-function χ

$$\chi = \bar{\chi}^0 [\mathbb{1} - \Gamma^c \bar{\chi}^0]^{-1}. \quad (2.40)$$

The corresponding lattice susceptibility is now obtained by summing over all frequencies and all cluster-momenta. Since a second order phase transition is marked by a divergence of its susceptibility χ , the critical temperature can be accurately determined by investigating where the leading eigenvalue of the matrix $\Gamma^c \bar{\chi}_0$ crosses 1.

2.4.2 Thermodynamic self-consistency and its implication for the DCA⁺

Early on, Hettler [35, 34] pointed out that the DCA is thermodynamic self-consistent algorithm, meaning that the vertex-function obtained with the DCA is in effect equal to the functional derivative of the cluster self-energy Σ_K towards the cluster Greens-function G_K

$$\Gamma_{K_1, K_2}^c = \frac{\delta \Sigma_{K_1}}{\delta G_{K_2}}. \quad (2.41)$$

This property is essential for the DCA in order to accurately monitor phase-transition in the context of the two-particle framework. As was shown by Baym and Kadanoff, an algorithm that violates Eq. (2.41) will report different phase transition temperatures in the single and two-particle framework, which is clearly unphysical.

In the DCA⁺, the lattice self-energy $\Sigma(k)$ is the central quantity in the self-consistency loop and is kept as a fully continuous function in momentum-space. The equivalent of the self-energy in the two-particle framework is the vertex-function. Consequently, we want to extend the two-particle framework of the DCA to the DCA⁺ by introducing a continuous lattice vertex function. In order to insure thermodynamic self-consistency, we demand that this continuous lattice vertex function satisfies the continuous equivalent of Eq. (2.41), i.e.

$$\Gamma(k_1, k_2) = \frac{\delta \Sigma(k_1)}{\delta G(k_2)}. \quad (2.42)$$

Since the exact functional dependence of the self-energy in terms of the Greens function is not tractable, it is not possible to deduce lattice vertex function Γ directly from Eq. (2.42). To that end, we apply the chain-rule, a common technique in the DCA⁺, on the right hand side and obtain

$$\Gamma(k_1, k_2) = \sum_{K_1, K_2} \frac{\delta \Sigma(k_1)}{\delta \Sigma_{K_1}} \frac{\delta \Sigma_{K_1}}{\delta G_{K_2}} \frac{\delta G_{K_2}}{\delta G(k_2)}. \quad (2.43)$$

We can now multiply both sides with a product of coarsegraining patches $\varphi_{\vec{K}}(k_1) \varphi_{\vec{K}'}(k_2)$ and integrate both sides of the equation over the Brillouin zone. Using the functional definition of the coarsegraining patch $\varphi_{\vec{K}}(\vec{k}_1) = \delta \Sigma_{\vec{K}} / \delta \Sigma(k_1)$, we can simplify the first factor of each term in Eq. (2.43) to a delta-function $\varphi_{\vec{K}}(\vec{k}_1) \times \delta \Sigma(k_1) / \delta \Sigma_{K_1} = \delta_{\vec{K}, \vec{K}_1}$. Using the coarsegrain condition for the Greens-function in the DCA⁺, we can simplify the last factor in each term to $\delta G_{K_2} / \delta G(k_2) = \varphi_{\vec{K}_2}(\vec{k}_2)$. Due to the orthonormality of the coarsegrain patches, we then arrive at another delta-function

$N_c / V \int dk_2 \varphi_{\vec{K}_2}(\vec{k}_2) \varphi_{\vec{K}'}(k_2) = \delta_{\vec{K}', \vec{K}_2}$. With the realization that $\delta \Sigma_{K_1} / \delta G_{K_2}$ is in fact the cluster vertex function Γ_{K_1, K_2}^c shown in Eq (2.41), we can now write down the DCA⁺ coarsegraining condition for the lattice vertex-function

$$\Gamma_{K_1, K_2}^c = \left(\frac{N_c}{V} \right)^2 \int_V d\vec{k}_1 d\vec{k}_2 \varphi_{\vec{K}_1}(\vec{k}_1) \Gamma(\vec{k}_1, \vec{k}_2) \varphi_{\vec{K}_2}(\vec{k}_2). \quad (2.44)$$

The DCA⁺ can therefore be extended to the two-particle framework in a straightforward way by introducing a lattice-mapping for the cluster vertex function Γ_{K_1, K_2}^c to a lattice vertex function $\Gamma(\vec{k}_1, \vec{k}_2)$, which is fully continuous in momentum space. It should be noted that the coarsegraining condition in Eq. (2.44) is the two-particle equivalent of the self-energy coarsegraining condition shown in Eq. (2.32), which forms the basis of the DCA⁺ algorithm. Just as with the self-energy in the DCA⁺, the lattice vertex function Γ is defined implicitly through a coarsegraining over its momenta vectors. Consequently, we have assumed that the lattice vertex function is a smooth function, in which case we can safely invert Eq. (2.44).

Assuming that we can invert Eq. (2.44), the process of detecting a phase transitions in the DCA⁺ is very similar to the DCA. Equations (2.36), (2.37) and (2.38) are not affected by the DCA⁺. In Eq. (2.39), the noninteracting two-particle lattice Greens function will now be computed using the continuous lattice self-energy in the Greens-functions of the integrand. Just as the lattice vertex function, the latter will be computed on a fine k-mesh, in which case the lattice Bethe-Salpeter equation for the DCA⁺ becomes

$$\chi = \chi^0 [1 - \Gamma \chi^0]^{-1}. \quad (2.45)$$

The next section will be entirely dedicated to a numerical algorithm that can solve the integral-equation (2.44) in a stable fashion.

2.4.3 Algorithm for the lattice-vertex $\Gamma(\vec{k}_1, \vec{k}_2)$

The lattice self-energy $\Sigma(\vec{k})$ is obtained in the DCA⁺ through a consecutive interpolation and deconvolution of the cluster-self-energy $\Sigma_{\vec{K}}$. To maintain the similarity between the vertex and the self-energy, we will follow the same recipe in order to implement a lattice-mapping for the vertex. To simplify the interpolation-process, we first decompose the cluster vertex into its singular value representation

$$\Gamma_{\vec{K}_1, \vec{K}_2}^c = \sum_i \sigma_i U_i(\vec{K}_1) V_i(\vec{K}_2). \quad (2.46)$$

In this way, the cluster vertex function can be written as a sum of factorized terms into its two indices K_1 and K_2 . The singular value decomposition of the cluster vertex is motivated by two reasons. First of all, the implementation of the interpolation is greatly simplified with the decomposition. It is much easier to interpolate functions with a single index than

a double momentum index. Secondly, in all cases encountered in this paper, we have observed that the singular vectors have typically a very strong frequency dependency, but a weak momentum dependency. This is not surprising from a physical point of view, as the effective interaction between the quasi-particles is very localized in real space. This weak momentum dependence makes them ideal functions to interpolate with cubic splines, without the risk of introducing any numerical anomalies. The interpolated vertex-function $\tilde{\Gamma}$ can thus be written down as,

$$\tilde{\Gamma}(\vec{k}_1, \vec{k}_2) = \sum_i \sigma_i U_i(\vec{k}_1) V_i(\vec{k}_2). \quad (2.47)$$

Just as in the DCA⁺, we generalize the coarsegraining in Eq. (2.44) to a convolution and expand the lattice vertex function into the set of basis-functions $\{\mathcal{B}\}$ used for the lattice self-energy³. If cubic Hermite splines [45] are used as basis-functions, we can rewrite Eq. (2.44) as a matrix-equation,

$$\begin{aligned} \tilde{\Gamma}(\vec{k}'_1, \vec{k}'_2) &= \sum_{\vec{k}_1, \vec{k}_2} \Phi(\vec{k}'_1, \vec{k}_1) \Gamma_l(\vec{k}_1, \vec{k}_2) \Phi(\vec{k}'_2, \vec{k}_2) \\ \Phi(\vec{k}_1, \vec{k}_2) &= \int d\vec{k}' \varphi_0(\vec{k}_1 - \vec{k}') \mathcal{B}(\vec{k}' - \vec{k}_2) \end{aligned} \quad (2.48)$$

Using a singular value decomposition of the matrix Φ , we can formally invert Eq. (2.48) and obtain an explicit formula for the lattice-vertex Γ

$$\begin{aligned} \Gamma(\vec{k}_1, \vec{k}_2) &= \sum_i \sigma_i \tilde{u}_i(\vec{k}_1) \tilde{v}_i(\vec{k}_2), \quad (2.49) \\ \tilde{u}_i(\vec{k}) &= \sum_j v_j^\Phi(\vec{k}) \frac{\langle u_j^\Phi(\vec{k}), U_i(\vec{k}) \rangle}{\sigma_j^\Phi}, \\ \tilde{v}_i(\vec{k}) &= \sum_j \frac{\langle V_i(\vec{k}), v_j^\Phi(\vec{k}) \rangle}{\sigma_j^\Phi} u_j^\Phi(\vec{k}). \end{aligned}$$

From the geometric interpretation of the DCA⁺, we know that the singular values of the Φ -matrix decay rapidly. Just as in the case of the self-energy, the lattice mapping for the vertex can only be performed if the expansion coefficients $\langle u_j^\Phi(\vec{k}), U_i(\vec{k}) \rangle$ and $\langle V_i(\vec{k}), v_j^\Phi(\vec{k}) \rangle$ decay faster than the singular values.

³The set of basis-functions $\{\mathcal{B}\}$ can be freely chosen by the reader, since the DCA⁺ is not dependent on the choice of the basis-functions. In this paper, we have used cubic Hermite splines [45].

Chapter 3

Implementation of the CT-AUX cluster-solver:

Abstract

Solving the cluster-impurity problem is the most expensive computational step in the entire DCA⁽⁺⁾-loop. As such, it is imperative to have a fast cluster-solver in order to reach the interesting regions of the phase-diagram. In this chapter, we present improvements to the continuous-time auxiliary field (CT-AUX) cluster solver, which was initially developed by Gull et. al. For the sampling of the configuration, we present a submatrix update algorithm that is very similar to the submatrix update algorithm in the Hirsch-Fye and originally developed by Nukala et. al. The algorithm takes optimal advantage of modern CPU architectures by consistently using matrix instead of vector operations, resulting in a speedup of a factor of at least 10. The measurement of the single- and two-particle Greens-function was also improved by introducing a non-equidistant fast Fourier transform (NFFT). Compared to a straightforward non-equidistant discrete Fourier-transform (NDFT), the NFFT algorithm accelerates the measurements with 2 to 3 orders of magnitude.

relevant papers:

- E. Gull, P. Werner, O. Parcollet and M. Troyer, *Continuous-time auxiliary-field monte carlo for quantum impurity models.*, EPL, 82:57003, 2008.
- P. Nukala, T. Maier, M. Summers, G. Alvarez, and T. Schulthess, *Fast update algorithm for the quantum Monte Carlo simulation of the Hubbard model*, PRB, 80:195111,2009.
- E. Gull, P. Staar, S. Fuchs, P. Nukala, M. Summers, T. Pruschke, T. Schulthess and T. Maier, *Submatrix updates for the continuous-time auxiliary-field algorithm*, PRB, 83:075122,2011.

- P. Staar, T. Maier and T. Schulthess, *Efficient non-equidistant FFT approach to the measurement of single- and two- particle quantities in continuous time Quantum Monte Carlo methods.*, Journal of Physics: Conference Series, 402:012015, 2012.

3.1 Introduction

The DCA⁽⁺⁾ algorithm is schematically represented in Fig. 3.1, where the emphasis has now been put on the CT-AUX cluster solver instead of the DCA⁽⁺⁾-loop. In order to have a fast implementation of the DCA⁽⁺⁾ algorithm, it is crucial to have an efficient, fast QMC cluster-solver, since other sections of the loop only take a marginal amount of the total run-time. All continuous time QMC-solvers consists of 2 parts, which are executed in consecutive order for many iterations during the sampling of the Greens-function G^I (see Fig 3.1). In the first part, one stochastically samples the partition function over its expansion order $\langle k \rangle$ in a step by step process, until the sample is uncorrelated from the original sample. In the CT-AUX solver, these steps consist of random insertions and removals of Hubbard Stratonovitch spins in the Hubbard Stratonovitch configuration [29]. For a Hybridization solver [101, 103], the steps are implemented by random insertions or removals of pairs of operators. In the second part, one measures the Greens-functions which correspond to the sample of the partition function. In this section, we want to review in detail how these two parts, i.e. the updating of the Hubbard Stratonovitch configuration and the measuring of the Greens-function, can be improved in the case of a CT-AUX cluster-solver.

In the past, two numerical algorithmic improvements have significantly increased the speed of the simulations with the Hirsch-Fye algorithm: the *delayed* updates [2] and the *submatrix* updates [74]. Both *delayed* and *submatrix* updates are mainly based on efficient memory management. Modern computer architectures employ a memory hierarchy: calculations are performed on data that is first loaded into registers. Any data that are not in the registers are stored either in the *cache* (currently with a size of a few MB) or in the *main memory* (with a size of a few GB). The cache is relatively fast, but there is little of it, while access to the main memory is often slow and shared among several compute cores. The bottleneck in many modern scientific applications, including the continuous-time algorithms, is not the speed at which computations are performed, but the speed at which data can be loaded from and stored into main memory. The central object in the Hirsch-Fye algorithm is a matrix, which for large cluster calculations does not fit into the cache. In essence, Monte Carlo updates consist of rank-one updates or matrix-vector products on this large matrix. Such updates perform $\mathcal{O}(\langle k \rangle^2)$ operations on $\mathcal{O}(\langle k \rangle^2)$ data, where $\langle k \rangle$ is the size of the matrix,

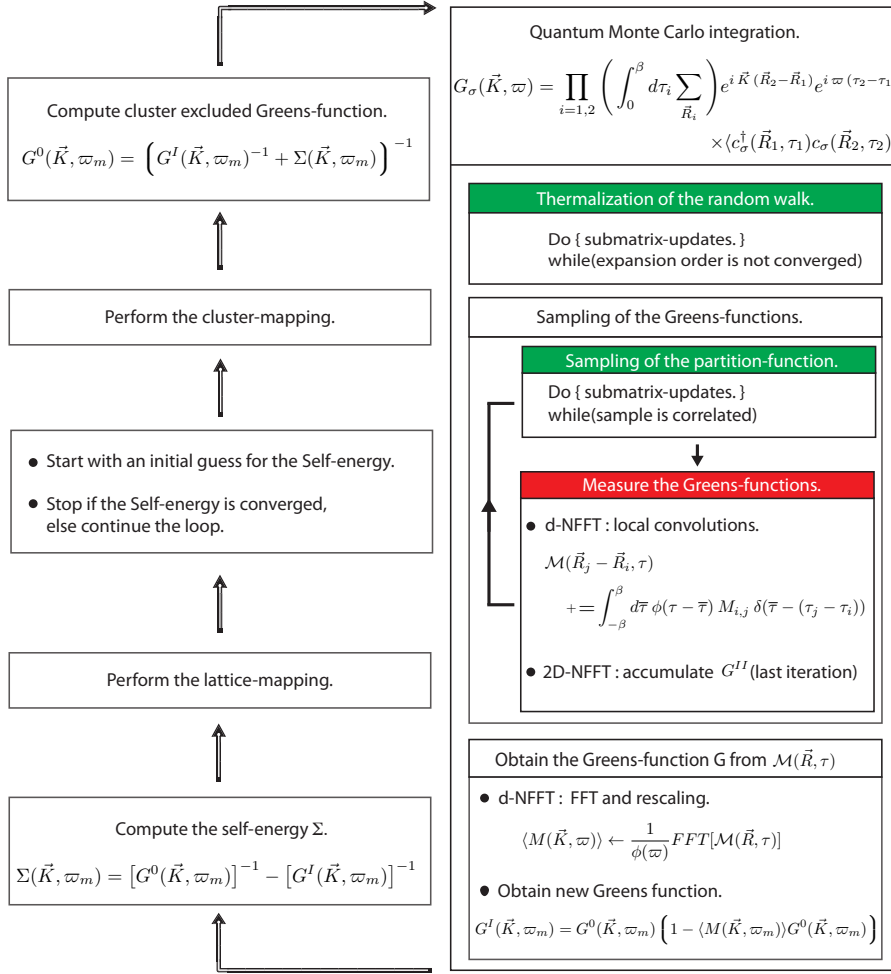


Figure 3.1: A schematic representation of the DCA⁽⁺⁾ self-consistency loop, in which a CT-AUX cluster solver is used. The sections affected by optimizations discussed in this chapter are high-lighted in red and green. The thermalization of the random of the stochastic walk and the sampling of the partition function are accelerated by the *submatrix* update procedure [33] (green). The measurement of the single and two-particle functions are accelerated respectively by the d-NFFT and 2D NFFT procedures (red). Notice that the d-NFFT algorithm spans over two sections of the Monte Carlo integration: In the sampling-phase of the Greens-function, it will convolute the samples of the function $M(\vec{r}, \tau)$ with a localized window-function ϕ to obtain \mathcal{M} and accumulate the latter. After the sampling phase, it will Fourier transform this convoluted function \mathcal{M} and rescale it by the appropriate Fourier coefficient of the window-function, in order to obtain the averaged Fourier transform of $\langle M(\vec{r}, \tau) \rangle$. The latter is than used to obtain the interacting Greens function G^I , from which a new self-energy Σ can be obtained.

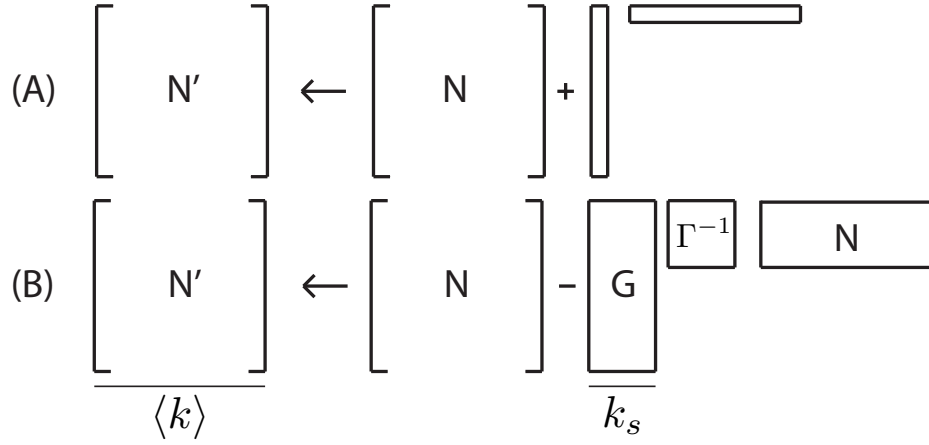


Figure 3.2: Illustration of update formulas. (A): rank-one updates, accessing $\mathcal{O}(\langle k \rangle^2)$ data points for $\mathcal{O}(\langle k \rangle^2)$ operations and performing one update. (B): submatrix updates, accessing $\mathcal{O}(\langle k \rangle^2)$ values but performing $\mathcal{O}(\langle k \rangle^2 k_s)$ operations for k_s updates.

and therefore run at the speed of memory. Matrix-matrix operations, with $\mathcal{O}(\langle k \rangle^3)$ operations executed on $\mathcal{O}(\langle k \rangle^2)$ data, could run at the speed of the registers, as more (fast) calculation per (slow) load / store operation are performed. The reason behind the success of both the *submatrix* and the *delayed* updates is the combination of several (slow) successive rank-one operations into one fast matrix-matrix operation, at the cost of some minimal overhead. This is illustrated in Fig. 3.2.

An important question is therefore how these techniques may be generalized to the continuous-time CT-AUX algorithm and how these savings translate into newly accessible physics. In the first section of the chapter, we present a submatrix-update procedure for the CT-AUX [33]. We will show that it accelerates the sampling of the partition function by a factor of at least 10 in the CT-AUX. This fast sampling leads to a quick thermalization, and allows us to linearly scale large cluster-problems to hundreds-of-thousands of processors [94].

The acceleration of the sampling procedure also means that the time spent in the measurements becomes disproportionately large. This motivated us to search for fast and efficient methods to measure the Greens-functions, both in the single- and two-particle case. Consequently, we present in the second part of the chapter methods to accelerate the measurements of the Greens function in the context of continuous time cluster solvers. They are based on non-equidistant fast Fourier transforms (NFFT). The focus in this paper lies on how the NFFT can be used to do measurements in the CT-

AUX cluster solver, but the findings can be applied to other continuous time solvers without complications such as the Hybridization-solver.

3.2 The Continuous-Time Auxiliary Field algorithm

In this section, we present the submatrix updates for CT-AUX [29], for which the linear algebra is similar to the well-known Hirsch Fye [36] method. We start with a short derivation of the CT-AUX solver from the partition function. Next, we show how the Metropolis sampling procedure can be used to perform the integration. Finally, we introduce the submatrix-updates and show the improvements to the time-to-solution.

3.2.1 The partition function expansion.

The Hamiltonian of the cluster-impurity model of size N_c can be parametrized by an effective hopping-matrix $t_{i,j}$ and an on-site interaction U

$$\mathcal{H} = \underbrace{\sum_{\sigma} \sum_{i,j=1}^{N_c} t_{i,j} c_{i,\sigma}^{\dagger} c_{j,\sigma}}_{=\mathcal{H}_0} + U \underbrace{\sum_{i=1}^{N_c} (n_{i,\uparrow} - 1/2)(n_{i,\downarrow} - 1/2)}_{=\mathcal{H}_i} - \frac{UN_c}{4}. \quad (3.1)$$

Here, $c_{i,\sigma}^{(\dagger)}$ denotes the annihilation (creation) of an electron at site i with spin σ and $n_{i,\sigma} = c_{i,\sigma}^{\dagger} c_{i,\sigma}$ represents the impurity occupation at site i with spin σ . Continuous-time algorithms expand expressions for the partition function $\mathcal{Z} = \text{Tr}[\exp(-\beta H)]$ at inverse temperature β into a diagrammatic series. In CT-AUX, this series is a perturbation expansion in the interaction:

$$\begin{aligned} \mathcal{Z} &= e^{-K} \text{Tr} \left[e^{-\mathcal{H}_0} T_{\tau} e^{-\int_0^{\beta} d\tau (\mathcal{H}_i - K/\beta)} \right] \\ &= e^{-K} \sum_{n \geq 0} \left(\frac{K}{\beta} \right)^n \int_0^{\beta} d\tau_0 \dots \int_{\tau_{n-1}}^{\beta} d\tau_n \\ &\quad \times \underbrace{\text{Tr} \left[e^{(\beta - \tau_n) \mathcal{H}_0} \left(1 - \frac{\beta \mathcal{H}_i}{K} \right) \dots e^{(\tau_2 - \tau_1) \mathcal{H}_0} \left(1 - \frac{\beta \mathcal{H}_i}{K} \right) e^{-\tau_1 \mathcal{H}_0} \right]}_{=\mathcal{Z}_n} \end{aligned} \quad (3.2)$$

As Rombouts indicated in his papers [82, 83], the interaction term \mathcal{H}_i in this expansion can be decoupled through the introduction of an auxiliary field,

$$\begin{aligned}
 1 - \frac{\beta \mathcal{H}_i}{K} &= \frac{1}{2} \sum_i \sum_{s_i = -1, 1} e^{\gamma s (n_{i,\uparrow} - n_{i,\downarrow})}, \\
 \cosh(\gamma) &= 1 + \frac{\beta U N_c}{2K},
 \end{aligned} \tag{3.3}$$

introducing an arbitrary constant K and auxiliary spins s . Hence

$$\begin{aligned}
 \mathcal{Z} &= \sum_{n \geq 0} \sum_{\substack{s_i = \pm 1 \\ 1 \leq i \leq n}} \int_0^\beta d\tau_1 \dots \int_{\tau_{n-1}}^\beta d\tau_n \left(\frac{K}{2\beta} \right)^n Z_n, \\
 \mathcal{Z}_n(\{s_i, \tau_i\}) &\equiv \text{Tr} \prod_{i=n}^1 e^{-\Delta \tau_i H_0} e^{s_i \gamma (n_\uparrow - n_\downarrow)}
 \end{aligned} \tag{3.4}$$

Note that the insertion of an arbitrary number of interaction vertices (auxiliary spin and time pairs) (s_j, τ_j) with $s_j = 0$ into Eq. (3.4) does not change the value of $\mathcal{Z}_n(\{s_i, \tau_i\})$. We will refer to auxiliary spins with value $s_n = 0$ as non-interacting spins. By performing a Grassman-variables integral, we can rewrite the trace of exponentials of one-body operators in Eq. (3.4) as a determinant of a $(n \times n)$ matrix N .

$$\begin{aligned}
 \frac{Z_n(\{s_i, \tau_i\})}{Z_0} &= \prod_{\sigma = \uparrow, \downarrow} \det N_\sigma^{-1}(\{s_i, \tau_i\}), \\
 N_\sigma^{-1}(\{s_i, \tau_i\}) &= e^{V_\sigma^{\{s_i\}}} - \mathcal{G}_{0\sigma}^{\{\tau_i\}} \left(e^{V_\sigma^{\{s_i\}}} - 1 \right), \\
 e^{V_\sigma^{\{s_i\}}} &= \text{diag} \left(e^{\gamma(-1)^\sigma s_1}, \dots, e^{\gamma(-1)^\sigma s_n} \right).
 \end{aligned} \tag{3.5}$$

$G_{0\sigma}^{\{\tau_i\}}$ denotes a $(n \times n)$ matrix of bare Green's functions, $(G_{0\sigma}^{\{\tau_i\}})_{ij} = \mathcal{G}_{0\sigma}(\tau_i - \tau_j)$. The matrix N is related to the Green's function matrix G by $G = N G_0$. The matrices G and N for auxiliary spin configurations that have the same imaginary time location for all vertices, but differ in the value of a single auxiliary spin s_p , are related by a Dyson equation

$$\begin{aligned}
 N' &= N + (G_{:,p} - \delta_{:,p}) \lambda N_{p,:}, \\
 G' &= G + (G_{:,p} - \delta_{:,p}) \lambda G_{p,:}, \\
 \lambda &= e^{V_p' - V_p} - 1.
 \end{aligned} \tag{3.6}$$

Here, the notation $X_{:,p}$ and $X_{p,:}$ represent respectively the p -th column or row of the matrix X . These Dyson-equations will form the basis for the submatrix-algorithm discussed later in this chapter.

It is also important to notice that Eq. (3.5) forms an explicit formula, that allows one to compute N directly as a function of the bare Green's function matrix and the auxiliary spin configuration $\{\tau_i, s_i\}$. This is a particularly handy expression, as it allows us to verify the correctness of the updated N -matrix at each time in the QMC integration.

3.2.2 The metropolis sampling procedure.

The infinite sum over expansion orders n and the integral and sum over vertices $\{(s_i, \tau_i)\}$ in Eq. (3.4) is computed to all orders in a stochastic Monte Carlo process: The algorithm samples time ordered configurations $\{(s_i, \tau_i)\}$ with weight

$$w(\{s_i, \tau_i\}) = \left(\frac{Kd\tau}{2\beta}\right)^n \prod_{\sigma=\uparrow,\downarrow} \det N_\sigma^{-1}(\{s_i, \tau_i\}). \quad (3.7)$$

To guarantee ergodicity of the sampling, it is sufficient to insert and remove spins with a random orientation $s_i = \uparrow, \downarrow$ at random times $0 \leq \tau_i < \beta$. Spin insertion updates are balanced by removal updates. For an insertion update we select a random time in the interval $[0, \beta)$ and a random direction for this new spin, leading to a proposal probability $p^{\text{prop}}(n \rightarrow n+1) = (1/2)(d\tau/\beta)$. For removal updates a random spin is selected and proposed to be removed, leading to a proposal probability $p^{\text{prop}}(n+1 \rightarrow n) = 1/(n+1)$. The combination of Eq. (3.7) with these proposal probabilities leads to the Metropolis acceptance rate $p(n \rightarrow n+1) = \min(1, R)$ with

$$R = \frac{K}{n+1} \prod_{\sigma=\uparrow,\downarrow} \frac{\det[N_\sigma^{(n+1)}]^{-1}}{\det[N_\sigma^{(n)}]^{-1}}. \quad (3.8)$$

In addition to the insertion and removal updates we consider spin flips of auxiliary spins. These updates are self-balancing, and the transition probability from a state $\{(s_1, \tau_1), \dots, (s_i, \tau_i), \dots\}$ to a state $\{(s_1, \tau_1), \dots, (-s_i, \tau_i), \dots\}$ is given by

$$R = \prod_{\sigma=\uparrow,\downarrow} \frac{\det[N_\sigma^{(n)}(\{(s_1, \tau_1), \dots, (-s_i, \tau_i), \dots\})]^{-1}}{\det[N_\sigma^{(n)}(\{(s_1, \tau_1), \dots, (s_i, \tau_i), \dots\})]^{-1}}. \quad (3.9)$$

Non-interacting auxiliary spins, or auxiliary spins with value 0, do not change the value of $w(\{s_i, \tau_i\})$ in Eq. (3.7). We will make use of this fact to precompute a matrix that is equivalent to N but contains non-interacting vertices represented by spin 0 auxiliary spins. Insertion and removal updates then become equivalent to spin-flip updates (from 0 to 1 or -1 and vice versa), thus allowing for a similar application of the sub-matrix update algorithm as in the case of the Hirsch-Fye solver [74]. This procedure is explained in more detail in Sec. 3.4.

3.3 Introduction of submatrix updates in the CT-AUX

To derive the sub-matrix updates algorithm equivalent to the one outlined in Ref. [74], let us consider a typical step k of the algorithm at which the interaction p_k with spin and time (s_{p_k}, τ_{p_k}) of m interaction vertices, is changed from V_{p_k} to V'_{p_k} . The new matrix G^{k+1} is then given by Eq. (3.6),

$$\begin{aligned} G^{k+1} &= G^k + (G^k_{:,p_k} - \delta_{:,p_k}) \delta_{p_k,:} \lambda^k G^k, \\ \lambda^k &= e^{V'_{p_k} - V_{p_k}} - 1. \end{aligned} \quad (3.10)$$

We proceed by showing how the determinant ratio $\det N^k / \det N^{k+1}$ of Eq. (3.8) as well as the new matrix N^{k+1} are computed efficiently using the Woodbury formula

$$[A^{-1} + X \Lambda Y]^{-1} = A - A X (\Lambda^{-1} + Y A X)^{-1} Y A. \quad (3.11)$$

As such, we define an inverse matrix A of G , analyze its changes during an update, and show how they can be incorporated in a small $(k \times k)$ matrix Γ that is easily computed by accessing only k_s^2 matrix elements in each step. The inverse of this matrix is then iteratively computed either by employing an *LU* decomposition, or a partitioning scheme. A change to the inverse Green's function matrix $A^k = (G^k)^{-1}$ is of the form

$$\begin{aligned} A^{k+1} &= A^k + \gamma^k (A^k_{:,p_k} - \delta_{:,p_k}) \delta_{p_k,:} \\ &= A^k (\mathbb{1} + \gamma^k \delta_{:,p_k} \delta_{p_k,:}) - \gamma^k \delta_{:,p_k} \delta_{p_k,:}, \\ \gamma^k &= e^{-\gamma \sigma (s'_{p_k} - s_{p_k})} - 1. \end{aligned} \quad (3.12)$$

We define $\tilde{A}^k_{ij} = A^k_{ij} + \gamma^k A^k_{:,p_k} \delta_{p_k,i} = A^k (\mathbb{1} + \gamma^k \delta_{:,p_k} \delta_{p_k,:})$, i.e. the matrix A^k where the p -th column is multiplied by $(1 + \gamma^k)$. We can recursively apply Eq. (3.12) to obtain an expression for performing multiple interaction changes, as long as they occur for different spins:

$$A^{k+p} = A^k \underbrace{\prod_{l=1}^p (\mathbb{1} + \gamma^l \delta_{:,p_l} \delta_{p_l,:})}_{=\mathcal{D}} + \sum_{l=1}^p \underbrace{\delta_{:,p_l}}_{=X} \underbrace{-\gamma^l}_{=\Lambda} \underbrace{\delta_{p_l,:}}_{=X^T} \quad (3.13)$$

Here, X is a fat column with 1 on positions $\{p_l, l\}$ with $l \in \{1, \dots, p\}$ and Λ is a $p \times p$ diagonal matrix with the elements $-\gamma^l$. The new matrix A^{k+p} is therefore generated from A^k by successively multiplying columns $p_l, 0 \leq l \leq p$ of A^k with γ^l and adding constants to the diagonal. X and Y^T are index matrices that label the changed spins and keep track of a prefactor γ^l . For measurements we need access to the Green's function G , not its inverse A . It is obtained after k_s steps by applying the Woodbury formula to Eq. (3.13)

$$G^{k+p} = \left[A^k \mathcal{D} + X Y \right]^{-1}, \quad (3.14)$$

$$= \mathcal{D}^{-1} G^k - \mathcal{D}^{-1} G^k X (\Lambda^{-1} + X^T \mathcal{D}^{-1} G^k X)^{-1} X^T \mathcal{D}^{-1} G^k. \quad (3.15)$$

We can simplify this expression by noting that the diagonal matrices commute and defining a new diagonal matrix $\tilde{\mathcal{D}} = X^T \mathcal{D}^{-1} X$. Using the identity $\tilde{\mathcal{D}} X^T = X^T \mathcal{D}^{-1}$, we obtain that

$$\begin{aligned} G^{k+p} &= \mathcal{D}^{-1} G^k - \mathcal{D}^{-1} G^k X (\Lambda^{-1} + \tilde{\mathcal{D}} X^T G^k X)^{-1} \tilde{\mathcal{D}} X^T G^k, \\ &= \mathcal{D}^{-1} G^k - \mathcal{D}^{-1} G^k X \underbrace{(\tilde{\mathcal{D}}^{-1} \Lambda^{-1} + X^T G^k X)^{-1}}_{=\Gamma^{-1}} X^T G^k, \\ &= \mathcal{D}^{-1} \left(G^k - G_{:,p_k} \Gamma^{-1} G_{p_k,:} \right). \end{aligned} \quad (3.16)$$

Here we have introduced a $k_s \times k_s$ - matrix Γ , which is defined as

$$\Gamma_{i,j} = G_{i,j}^k - \delta_{i,j} \frac{1 + \gamma_i}{\gamma_i}, \quad (3.17)$$

Note that G^k is the interacting Green's function at step $k = 0$ and not the bare Green's function \mathcal{G}^0 of the effective action, unless all auxiliary spins are zero. Translating this Green's function formalism to a formalism for N matrices is straightforward. We multiply Eq. (3.16) from the right with $(\mathcal{G}^0)^{-1}$, which yields

$$N^{k+p} = D^{-1}(N - G_{:,p_k} \Gamma^{-1} N_{p_k,:}), \quad (3.18)$$

where one $G_{:,p_k}$ remains in Eq. (3.18). Notice here that the Greens-function matrix is never computed explicitly. For the interacting vertices, we can deduce from Eq. (3.5) a simple formula for $G_{i,j}^k$. By simply multiplying Eq. (3.5) on the left-hand side with N , we obtain that,

$$1 = Ne^V - NG_0 e^V + NG_0 \quad (3.19)$$

We can now exploit the relationship $G = N G_0$ and arrive at,

$$G_{ij} = (N_{ij} e^{V_j} - \delta_{ij}) / (e^{V_j} - 1) \quad (3.20)$$

For the non-interacting vertices, we we need to compute $G_{ij} = \sum_k N_{ik} G_{kj}^0$ at a cost of $O(N)$ for each i and j . To either accept or reject a configuration change, we need to compute the determinant ratio $\det N^{k+1} / \det N^k$. The latter is equivalent to $\det G^{k+1} / \det G^k \equiv \det A^k / \det A^{k+1}$, since the G_0 matrices are the same. From the matrix-determinant lemma and Eq. (3.13), we know that

$$\det A^{k+1} = \prod_{j=1}^p (-\gamma_j) \det A^k \det \Gamma. \quad (3.21)$$

The computation of the determinant $\det \Gamma^k$ is an expensive $O(k^3)$ operation, if Γ^k has to be recomputed from scratch. However, we successively build Γ^k by adding rows and columns. This can be implemented efficiently by progressively building the LU decomposition of Γ . This LU -decomposition is then used for the inversion in Eq. (3.18). For each accepted update, we keep track of a LU decomposition of Γ in the following way:

$$\begin{aligned} \Gamma^k &= \begin{pmatrix} \Gamma^{k-1} & s \\ w^T & d \end{pmatrix} = \begin{pmatrix} L^{k-1} & 0 \\ x^T & 1 \end{pmatrix} \begin{pmatrix} U^{k-1} & y \\ 0 & \beta \end{pmatrix}, \\ y &= L^{-1} s, \quad x = (U^T)^{-1} w, \quad \beta = G_{k,k} - \frac{1 + \gamma^k}{\gamma^k} - x^T y \end{aligned} \quad (3.22)$$

where both x^T and y are computed in $O(k^2)$ by solving a linear equation for a triangular matrix. The determinant ratio needed for the acceptance of an update is

$$\frac{\det A^{k+1}}{\det A^k} = -\beta\gamma^k. \quad (3.23)$$

These updates have been formulated for spins that have only been updated once. In the case where the same spin is changed twice or more, rows and columns in Γ , or L and U , need to be modified. These changes are of the form $\Gamma \rightarrow \Gamma + uv^T$, and Bennett's algorithm [12] can be used to refactorize the matrix. The probability to accept/reject a $(k+1)$ -th spin requires $O(k^2)$ operations, since the computation of x and y in Eq. (3.22) requires $O(k^2)$ operations.

3.4 The random walk with submatrix updates

The sums and integrals of Eq. (3.4) are computed by a random walk in the space of all expansion orders, auxiliary spins, and time indices. In the cluster case, configurations acquire an additional site index. A configuration c_n at expansion order n contains n interaction vertices with spins, sites, and time indices:

$$c_n = \{(\tau_1, s_1, \sigma_1), \dots, (\tau_n, s_n, \sigma_n)\}. \quad (3.24)$$

The configuration space \mathcal{C} consists of all integrands / summands in Eq. (3.4), which we can represent by sets of triplets of numbers, consisting of auxiliary spins, times, and site indices,

$$\mathcal{C} = \{c_i \mid i \in \mathbb{N}\}. \quad (3.25)$$

To efficiently make use of the submatrix updates, we add an additional step before insertion and removal updates are performed. In this preparation step, we insert a number k_s of randomly chosen non-interacting vertices with auxiliary spin $s = 0$, which, as discussed in Sec. 3.2, does not change the value of the partition function. Once these vertices are inserted, insertion and removal updates at the locations of the pre-inserted non-interacting vertices become identical to spin-flip updates. An insertion update of a spin $s = 1$ now corresponds to a spin-flip update from spin $s = 0$ to spin $s = 1$ and similar for removal updates. To accommodate this pre-insertion step, we split our random walk into an inner and an outer loop. In the outer loop, we perform measurements of observables and run the preparation step discussed above as well as recompute steps. These steps are described

in more detail below. In the inner loop (labeled by k) we perform k_s insertion, removal, or spin-flip updates at the locations of the pre-inserted non-interacting spins. It is best to choose k_s small, such that the Γ -matrices fit into the cache.

3.4.1 Preparation steps

We begin a Monte Carlo sweep with preliminary computations for spins that we will propose to insert or remove. For this, we generate randomly a set of k_{\max}^{ins} pairs of (site,time) indices, where k_s denotes the maximum insertions possible. We then compute the additional rows of the matrix N for these noninteracting spins:

$$\tilde{N} = \begin{pmatrix} N & 0 \\ \tilde{R} & 1 \end{pmatrix}, \quad (3.26)$$

where \tilde{R} is a matrix of size $n \times k_s$ containing the contributions of newly added noninteracting spins,

$$\tilde{R}_{ij} = \mathcal{G}_{ik}^0 (e^{-\gamma \sigma s_k} - 1) N_{kj}, \quad (3.27)$$

at the cost of $\mathcal{O}(n^2 k_s)$, as well as the Green's function matrix $G = N\mathcal{G}^0$ for the new spins.

3.4.2 Insertion, removal, spinflip of an auxiliary spins

Vertex insertion updates are performed by proposing to flip one of the newly inserted non-interacting spins from value zero to either plus or minus one. The determinant ratio is obtained by using (3.21), i.e. by consecutive solving Eq. (3.22). If the update is accepted, the auxiliary spin is changed and the matrix Γ is enlarged by a row and a column. Starting from a configuration $c_k = \{(\tau_1, s_1, \sigma_1), \dots, (\tau_k, s_k, \sigma_k)\}$, we propose to remove the interaction vertex (τ_j, s_j, σ_j) . The ratio of the two determinants is computed by proposing to flip an auxiliary spin from ± 1 to zero. For this we compute s and w as in Eq. (3.22), and then compute x and y by solving a linear equation for a triangular system. Finally, Eq. (3.23) is computed using Eq. (3.22). If the update is accepted the auxiliary spin is set to zero and Γ is enlarged by a row and a column. To perform a spin-flip update we choose a currently interacting spin with value ± 1 and propose to flip it to ∓ 1 . If the update is accepted, Γ grows by a row and a column.

3.4.3 Recompute step

This scheme of insertion, removal, and spinflip updates is repeated k_s times. With each accepted move the matrix Γ grows by a row and a column. To

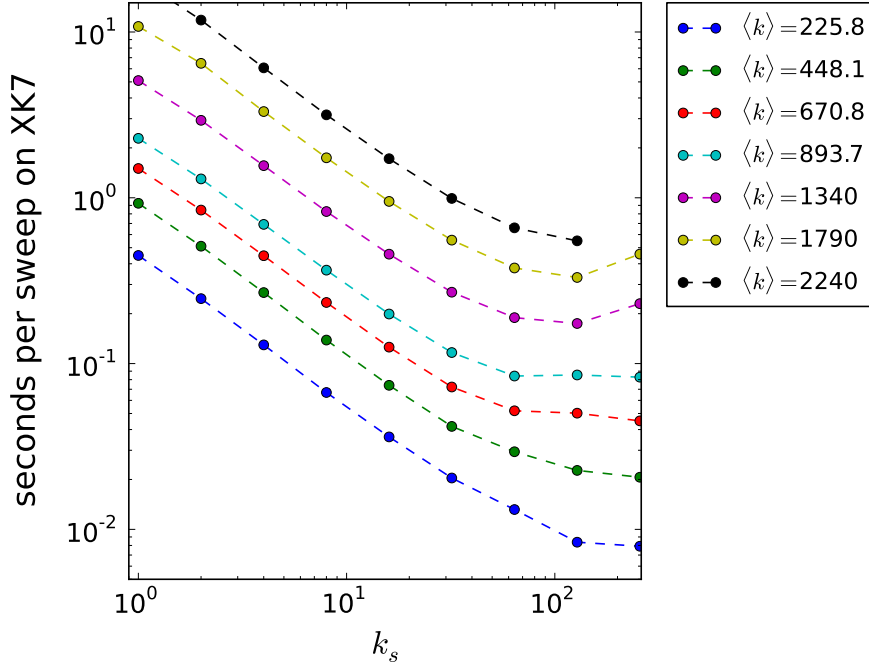


Figure 3.3: The seconds per sweep on an XK7-node (Todi). By increasing the submatrix-size k_s , we can keep the Gamma-matrices in cache and therefore avoid latency between the CPU and main-memory as well as between the CPU and the GPU.

keep the algorithm efficient, we periodically recompute the full N matrix using Eq. (3.18),

$$N^{k+k_s} = \mathcal{D}^{-1} (N - G_{:,p_k} \Gamma^{-1} N_{p_l,:}). \quad (3.28)$$

As Γ grows with every accepted update, the cost of computing determinant ratios is $O(k^2)$. The recompute step consists of two inversions for L and U , which are both $O(k^2)$ operations, and two matrix multiplications, at cost $O(k^2N)$ and $O(N^2k)$ respectively. Noninteracting auxiliary spins can then be removed from $N_{ij}^{k+k_s}$ by deleting the corresponding rows and columns.

3.4.4 Speed-up versus submatrix k_s .

In Fig. 3.3, we show the seconds per sweep on an XK7-node (Todi). By increasing the submatrix-size k_s , we can keep the Gamma-matrices in cache and therefore avoid latency between the CPU and main-memory as well as between the CPU and the GPU. The optimal submatrix-size lies around 10^2 .

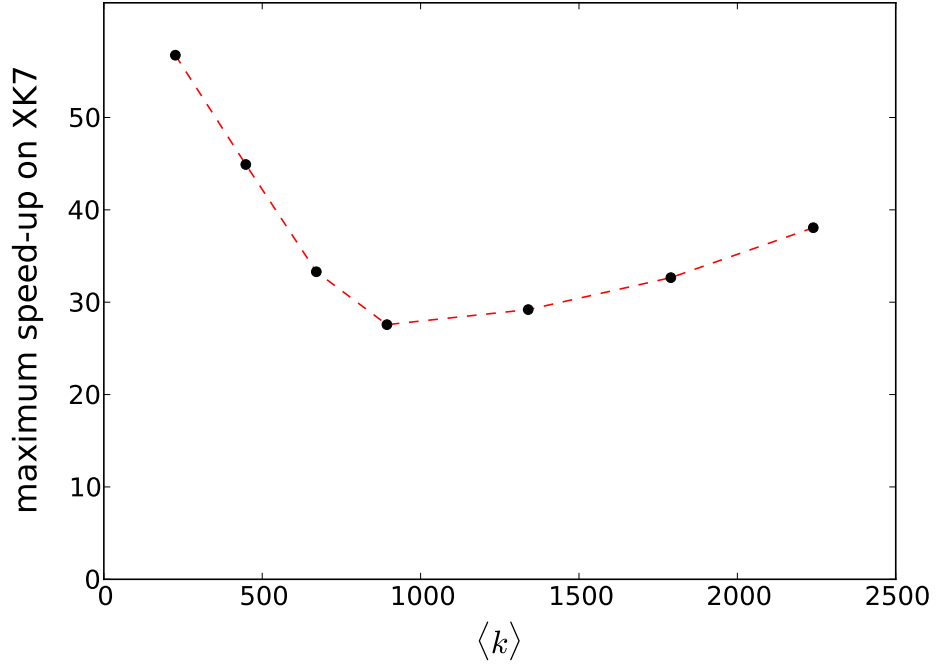


Figure 3.4: The maximum speed-up as a function of the expansion-order (or matrix-size) $\langle k \rangle$. The latter is defined as the ratio of the maximum time per sweep versus the minimum time per sweep as a function of the submatrix size k_s

In Fig. 3.4, we show the maximum speed-up on an XK7-node (Todi), by plotting the ratio of the maximum time per sweep versus the minimum time per sweep as a function of the submatrix size k_s . It is interesting to see that the maximum-speed-up is minimal around the matrix-size $\langle k \rangle \approx 800$. There is a logical explanation for this. For small Γ matrices, we can take full advantage of the cache. For large matrices, the CUBLAS-library becomes extremely efficient. However, for matrix-sizes of $\langle k \rangle \approx 800$, the cache of the current Bulldozer CPU is too small, while at the same time the matrix is also too small to fully occupy the GPU-cores.

3.5 Single and two-particle measurement with d-NFFT:

3.5.1 measurement of single particle quantities

There exist two types of single particle quantities. The most common ones, such as the self-energy and the single-particle Greens function G^I are translation invariant in space and time. The non-invariant single particle Greens functions are only used during the computation of the two-particle Greens

function. We focus first on the space-time translation invariant quantities. In the CT-AUX algorithm, the single-particle Greens function G^I is not directly obtained via the Monte Carlo integration, but derived from an other accumulated quantity $\langle M[\mathbf{k}, i\omega] \rangle$. In the latter, $\langle \dots \rangle$ represents the Monte Carlo integration. Following closely the notation in Ref. [29], we can write down the quantity M as a function of the N -matrix and its corresponding Hubbard-Stratonovitch spin configuration $\{v\}$,

$$\begin{aligned} G^I[k] &= G^0[k] - G^0[k] \langle M[k] \rangle G^0[k], \\ M^{\{v\}}[\mathbf{r}, i\omega] &= \sum_{\lambda_1, \lambda_2 \in \{v\}} e^{i\omega(\tau_{\lambda_2} - \tau_{\lambda_1})} M^{\{v\}}[\lambda_1, \lambda_2] \\ M^{\{v\}}[\lambda_1, \lambda_2] &= \delta_{\mathbf{r}, \mathbf{r}_{\lambda_2} - \mathbf{r}_{\lambda_1}} (e^{V\{v_{\lambda_1}\}} - 1) N[\lambda_1, \lambda_2]. \end{aligned} \quad (3.29)$$

The measurement boils down to a Fourier transform of non-equispaced data since the vertices reside on randomly chosen imaginary times. This eliminates the possible use of the fast Fourier transform (FFT) because the latter requires equispaced data. In a straightforward implementation of the non-equispaced discrete Fourier transform (NDFT), each measurement would be a two step process. One would first compute the Fourier coefficient matrix $C_{m,l} = e^{i\omega_m \tau_l}$, which involves the evaluation of many expensive trigonometric functions. Next, the actual transform would be carried out via a matrix-vector multiplication. Both operations scale as $\mathcal{O}(N_\omega N_\tau)$, where N_ω and N_τ represent respectively the number of positive matsubara frequencies and the number of vertices.

We present here a measurement algorithm which scales linear in N_τ , and requires only one Fourier transform at the end of each Monte-Carlo integration. The dependency of our measurement algorithm on N_ω is therefore virtually eliminated and a speed-up of order N_ω can be expected. Before we introduce the d-NFFT, it is instructive to give a short review on the non-equispaced fast Fourier transform (NFFT) algorithm [44]. The NFFT algorithm is based on the convolution theorem, shown in Eq. (3.30). It states that the Fourier transform of a convolution is equal to the point-wise product of the Fourier transforms:

$$f_\omega \varphi_\omega = \int_0^\beta d\tau e^{i\omega \tau} \left[\int_0^\beta d\lambda \varphi(\tau - \lambda) f(\lambda) \right]. \quad (3.30)$$

The NFFT algorithm makes use of this theorem in the following manner. First, the non-equispaced data-set $\{\tau_i, f_i\}$ is projected onto an equispaced grid, with $m N_\omega$ intervals. Here, m is called the oversampling factor and is typically in the range of 4 to 10. This projection is achieved via a convolution

Algorithm 1 The delayed-NFFT algorithm, which computes the single-particle Greens-function G^I :

Require: N -samples $\{v\} = \{\{\tau_1, M(\tau_1)\}\}$ of function $M(\tau)$ at random times in the interval $[-\beta, \beta]$

Ensure: Return the average of the Fourier-transformed samples $\langle M(\omega) \rangle$.

Define the function $\mathcal{M}(\tau_1)$ on the oversampled grid $\{\tau_1 = -\beta + l_1 \Delta\tau \mid l_1 \in \{0, \dots, m N_\omega\}\}$ and with $\Delta\tau = \frac{2\beta}{m N_\omega}$

```

for  $i = 1 \rightarrow N$  do
  for  $\{\tau_1, M(\tau_1)\} \in \{v\}_i$  do
     $I = \frac{\tau_1 + \beta}{\Delta\tau}$    {find the lower-index of  $\tau_i$  such that  $\tau(I) \leq \tau_1 < \tau(I+1)$ }

    for  $\lambda = -m \rightarrow m$  do
       $\varphi_{interp} \leftarrow$  interpolate  $\varphi$  at  $\tau(I + \lambda) - \tau_1$ 
       $\mathcal{M}(I + \lambda) \leftarrow \mathcal{M}(I + \lambda) + \varphi_{interp} * M(\tau_1)$ 
    end for
  end for
end for

```

Compute $\mathcal{M}(\omega) \leftarrow FFT[\mathcal{M}(\tau)]$

Compute $\langle M \rangle \leftarrow \frac{\mathcal{M}(\omega)}{N * \varphi(\omega)}$

Compute $G^I(\omega) \leftarrow G^0(\omega) [1 + \langle M(\omega) \rangle G^0(\omega)]$

with a localized, translation invariant kernel φ , such as a Gaussian distribution function. The localization of the kernel is in the range of $[-m, m]$ lattice spacings, which insures that the time needed for the convolution scales linearly with the data size. Next, the FFT algorithm is applied on the projected, now equispaced data and one obtains its representation in Matsubara frequencies. At last, each data-point in Matsubara frequencies is renormalized by its corresponding Fourier-coefficient of the kernel φ , and hence we recover the Fourier component f_ω of the original non-equispaced data-set. The NFFT algorithm can be summarized as,

$$f_\omega \leftarrow \frac{1}{\varphi_\omega} FFT \left[\left\{ \bar{f}_l = \sum_\lambda \varphi\left(\tau_\lambda - \frac{l\beta}{N}\right) f_\lambda \mid l \in 1, \dots, m N_\omega \right\} \right] = NFFT(\{\tau_\lambda, f_\lambda\}) \quad (3.31)$$

From Eq. (3.31), it is clear that the NFFT algorithm scales as $\mathcal{O}(m N_\omega \log(m N_\omega) + m N_\tau)$. An important property of the NFFT-algorithm is that for particular kernels the maximum relative error on f_ω can be proven to decrease exponentially as a function of the oversampling parameters m [44]. In the case of

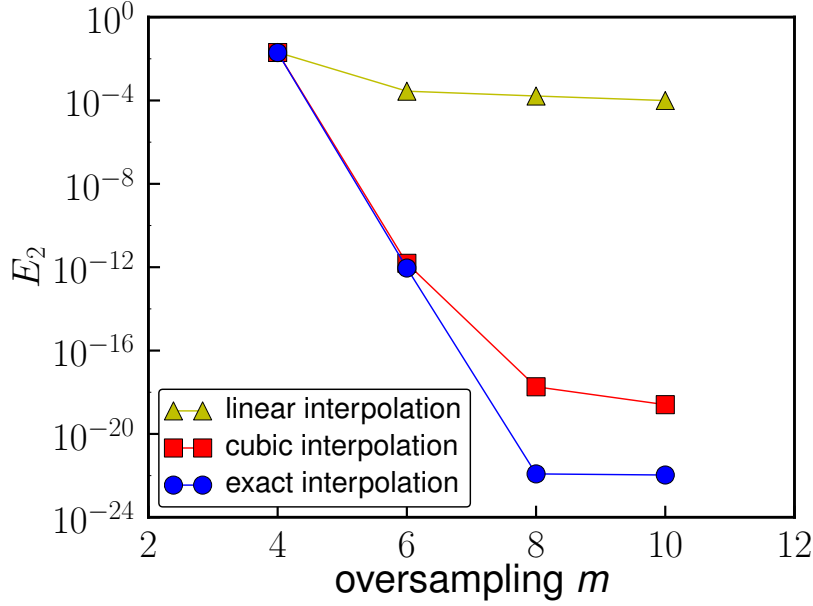


Figure 3.5: The relative error E_2 versus the oversampling factor m . The error decreases exponentially for increasing m , as expected from the theory. When the kernel φ is approximated by an interpolating value, the error becomes independent of the m . In the linear regime, the error saturates at $\approx 10^{-4}$, while in the cubic regime it saturates at machine precision $\approx 10^{-16}$.

a gaussian window function φ_g , the maximum relative error E_2 is

$$E_2 = \frac{|f_{\omega}^{NFFT} - f_{\omega}^{NDFT}|}{\|f_{\omega}^{NDFT}\|_1} = 4 e^{-m \pi (1-1/(2\sigma-1))}.$$

In the case of a Monte-Carlo integration with a continuous time solver, the latter will produce many data-sets, all on a different set of randomly chosen times. Since the FFT is a linear operation, we can delay this operation until the end of each Monte-Carlo integration. In this way, one accumulates the convoluted function $M[\mathbf{r}, \tau_i]$ during the Monte-Carlo integration, instead of $M[\mathbf{r}, i \omega]$.

$$M[\mathbf{r}, \tau_i] = \sum_{\lambda_1, \lambda_2 \in \{v\}} \varphi((\tau_{\lambda_2} - \tau_{\lambda_1}) - \tau_i) M^{\{v\}}[\lambda_1, \lambda_2] \quad \text{with} \quad \tau_i = \frac{2i\beta}{m N_{\omega}} \quad (3.32)$$

As a result, only a single Fourier transform and rescaling has to be performed on $M[\mathbf{r}, \tau_i]$ to obtain $\langle M[\mathbf{k}, \omega] \rangle$ at the end of each Monte Carlo

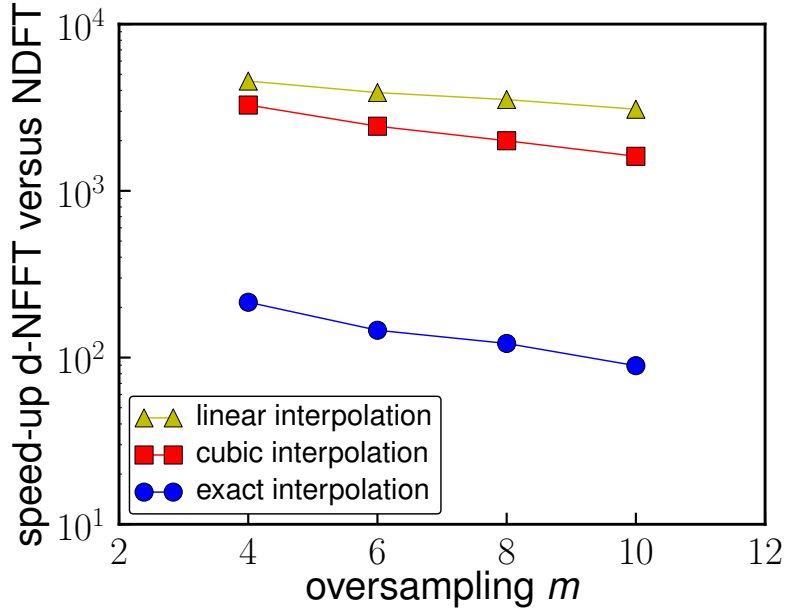


Figure 3.6: The speed-up of d-NFFT compared to DFT, versus the oversampling parameter m . Replacing the exact evaluation of the kernel φ with its interpolated value results clearly in a drastic speed-up. For this figure, we used typical parameters for a Monte Carlo simulation ($N_\omega = 512, N_\tau = 1024$).

iteration. From the latter, G^I can be obtained in the usual manner according to Eq. (3.29). As shown in Fig. (3.1), this delayed-NFFT (d-NFFT) will now span over two sections in the Monte-Carlo integration. In the accumulating phase, it will convolute the function-samples on the oversampled NFFT-grid. As a consequence, each measurement now boils down to a convolution, and the desired scaling linear $\mathcal{O}(m N_\tau)$ is obtained. Only after the Monte-Carlo integration, we will Fourier transform the oversampled function $M[\mathbf{r}, \tau_l]$. Notice that the delay of the FFT will not affect the accuracy, and the relative error will still decrease exponentially as a function of the oversampling. A second optimization can be obtained by replacing the exact evaluation of the kernel φ with an interpolated value. Evaluating a Gaussian distribution function involves the evaluation of trigonometric functions, which require many cycles to compute. A drastic improvement in the speed-up can be obtained when φ is interpolated, but generally at a loss of accuracy. The accuracy can be improved via an adequate tuning of the oversampling factor m . This is illustrated in Fig. (3.5), which shows the relative error E_2 for different interpolation schemes. As expected from the theory, one can observe an exponential decline if the kernel is evaluated exactly. For linear and cubic interpolated kernels, we observe that the error saturates as a function

of m , due to systematic errors. For linear interpolation, the errors saturates at $\approx 10^{-4}$, while in the cubic regime it saturates at machine precision. In Fig. (3.6) we show the speed-up of d-NFFT versus NDFT. Notice that the speed-up is of the order $\mathcal{O}(N_\omega) \sim 10^3$. Considering both the need for accuracy and speed-up, the most optimal choice for QMC cluster solvers seems to be a cubic interpolation scheme at $m = 8$. In this way, the error on the Fourier transform will always be two to three orders of magnitude smaller than a typical statistical error of a Monte-Carlo integration. The fully optimized d-NFFT algorithm is summarized in Alg. (1).

3.5.2 measurement of two-particle Greens-function G^{II}

The two-particle Greens-function G^{II} is obtained via a Quantum Monte Carlo Integration of a product of translation-noninvariant¹ single-particle TNSP Greens functions $G_\sigma^I[k_1, k_2]$,

$$G_{\sigma_1, \sigma_2}^{II}[k_1, k_2, q] = \left\langle G_{\sigma_1}^I[k_1, k_1 + q] G_{\sigma_2}^I[k_2 + q, k_2] - \delta_{\sigma_1, \sigma_2} G_{\sigma_1}^I[k_1, k_2] G_{\sigma_2}^I[k_2 + q, k_1 + q] \right\rangle. \quad (3.33)$$

Here, $\langle \dots \rangle$ represents the Monte Carlo Integration. Just as in the single-particle case, the (TNSP) Greens functions $G^{\{v\}\sigma}[k_1, k_2]$ can be computed straightforwardly from the N -matrix and its Hubbard-Stratonovitch configuration $\{v\}$.

$$\begin{aligned} G^{\{v\}\sigma}[k_1, k_2] &= \delta_{k_1, k_2} G^0[k_1] - G^0[k_1] M^{\{v\}\sigma}[k_1, k_2] G^0[k_2], \\ M^{\{v\}\sigma}[k_1, k_2] &= \sum_{\lambda_1, \lambda_2 \in \{v\}\sigma} (e_{\lambda_1, \lambda_2}^{V\{\varphi\}\sigma} - 1) N[\lambda_1, \lambda_2] \times e^{i(\omega_2 \tau_{\lambda_2} - \omega_1 \tau_{\lambda_1})} e^{i(\mathbf{k}_2 \mathbf{r}_{\lambda_2} - \mathbf{k}_1 \mathbf{r}_{\lambda_1})}. \end{aligned} \quad (3.34)$$

For this, the NFFT algorithm has to be generalized to two dimensions, which is straightforward. One constructs a fine 2D grid of the size mN_ω in both dimensions and convolutes the M-function with a 2D localized kernel. In our case, we simply used the product of two 1D Gaussian distributions. Just as in the 1D case, we apply the FFT on this fine equispaced grid, and renormalize each function-value in the Matsubara representation by the associated Fourier component of the localized kernel.

¹in time and space

Algorithm 2 A 2D-NFFT algorithm to compute the TNSP Greens-function in the CT-AUX.

Require: A set of samples $\{v\} = \{\{\tau_i, \tau_j, M_{i,j}\}\}$ of the 2D function $M(\tau_1, \tau_2)$ -function at random times in the interval $[-\beta, \beta] \times [-\beta, \beta]$.

Ensure: Return the corresponding TNSO Greens-function $G(\omega_1, \omega_2)$.

Define the function $\mathcal{M}(\tau_1, \tau_2)$ on the 2D-oversampled grid $\{\{\tau_1 = -\beta + l_1 \Delta\tau, \tau_2 = -\beta + l_2 \Delta\tau\} \mid l_1, l_2 \in \{0, \dots, m N_\omega\}\}$ and with $\Delta\tau = \frac{2\beta}{m N_\omega}$.

```

for  $\{\tau_i, \tau_j, M_{i,j}\} \in \{v\}$  do
   $I \leftarrow \frac{\tau_i + \beta}{\Delta\tau}$    {find the lower-index of  $\tau_i$  such that  $\tau(I) \leq \tau_i < \tau(I + 1)$ }
   $J \leftarrow \frac{\tau_j + \beta}{\Delta\tau}$    {find the lower-index of  $\tau_j$  such that  $\tau(J) \leq \tau_j < \tau(J + 1)$ }
  for  $\lambda_i = -m \rightarrow m$  do
     $\varphi_i \leftarrow \varphi(\tau(I + \lambda_i) - \tau_i)$ 
    for  $\lambda_j = -m \rightarrow m$  do
       $\varphi_j \leftarrow \varphi(\tau(J + \lambda_j) - \tau_j)$ 
       $\mathcal{M}(I + \lambda_i, J + \lambda_j) \leftarrow \mathcal{M}(I + \lambda_i, J + \lambda_j) + \varphi_i * \varphi_j * M_{i,j}$ 
    end for
  end for
end for

Compute  $\mathcal{M}(\omega_1, \omega_2) \leftarrow FFT[\mathcal{M}(\tau_1, \tau_2)]$ 
Compute  $M(\omega_1, \omega_2) \leftarrow \frac{\mathcal{M}(\omega_1, \omega_2)}{\varphi_1(\omega_1) * \varphi_2(\omega_2)}$ 

Compute  $G^I(\omega_1, \omega_2) \leftarrow \delta_{\omega_1, \omega_2} G^0(\omega_1) - G^0(\omega_1) M(\omega_1, \omega_2) G^0(\omega_2)$ 
    
```

In contrast to the 1D case, it is not possible to use a delayed FT scheme here. The TNSP Greens function needs to be computed every single time in order to evaluate Eq. (3.33). As a consequence, the measurement of a two-particle function is generally determined by the speed at which the FFT can be performed on the oversampled grid. We will therefore devote the rest of this section to tricks, which can speed up the FFT. First, we can take advantage of the fact that the function-values are real. This means that the function values in Matsubara representation will have a conjugate symmetry, and it is thus sufficient to compute only half of the Matsubara frequencies. This should speed up the FFT by a factor of two [23]. Another trick that should be used is pruning. Notice that we are actually only interested in a small subset of Fourier components of order $\mathcal{O}(N_\omega^2)$ instead of all them $\mathcal{O}(m^2 N_\omega^2)$. This essentially implies that we can skip the $(m - 1) N_\omega$ Fourier Transforms in the second dimension. The FFT in 2D is therefore not of the order $\mathcal{O}(m^2 N_\omega^2 \log(m^2 N_\omega^2))$, but rather of $\mathcal{O}(m^2 N_\omega^2 \log(m N_\omega) +$

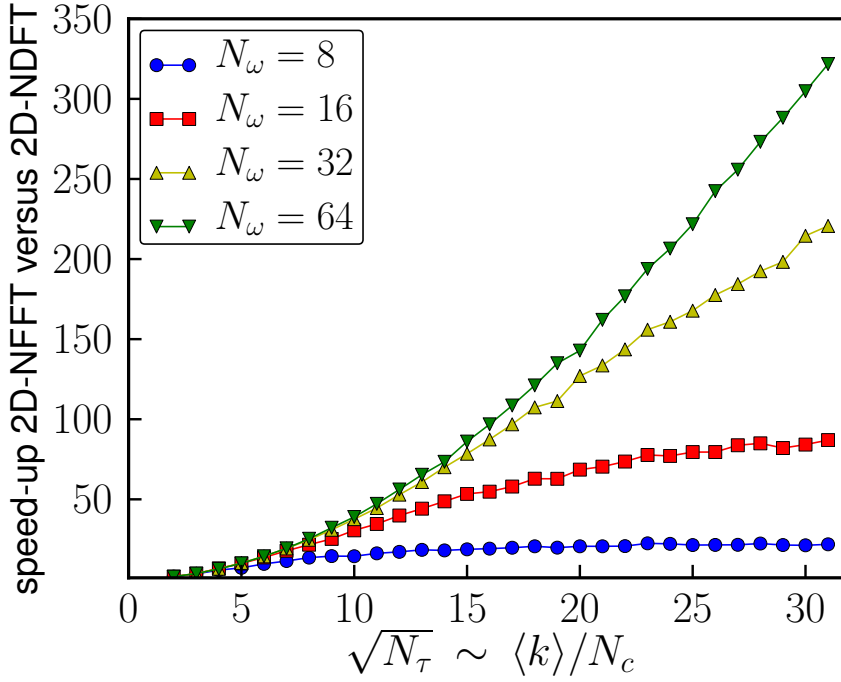


Figure 3.7: The speed-up of an optimized 2D-NFFT compared to NDFT in 2D for an oversampling factor $m = 6$, which corresponds to a relative error of $E_2 \sim 10^{-6}$. The method is clearly advantageous for large number of Matsubara frequencies ($N_\omega \gg 1$) in the strongly correlated region $\langle k \rangle \gg 1$.

$m N_\omega^2 \log(m N_\omega)$). The pruning of our FFT leads generally to an additional speed-up of roughly 2. In Fig. (3.7), we show you the combined speed-up of the NFFT method in 2D versus the NDFT. Due to its better scaling, the NFFT is clearly a good improvement in the case of a large number of vertices and a large number of Matsubara frequencies. The algorithm will therefore be hugely beneficial in the case of low temperatures and strong correlation.

Study of phase-diagram of the 2D Hubbard model.

Abstract

The DCA and DCA⁺ algorithms were developed to study the dominating physics of the high-temperature copper based superconductors. The simplest model that emulates these materials is the 2D Hubbard model on a square lattice with a strong repulsive interaction, i.e an on-site repulsion U that equates the width of the band-structure. In this chapter, we investigate the phase-diagram of the 2D Hubbard model with the DCA⁺ and show that the latter obtains the quantitatively and qualitatively the correct physics. We look in depth at the antiferromagnetic transition at half-filling and show that the transition has an s-wave symmetry and that the transition temperature T_N decays logarithmically, as expected by the Mermin-Wagner theorem. We investigate the pseudo gap region, which is located in the low hole-doped region of the phase-diagram and characterized by a partial suppression of the density of states at the Fermi energy at the antinodal points. We will show that the DCA⁺ can converge quantitatively the pseudo-gap temperature T^* , contrary to the DCA. We will also study the superconducting transition, both in the attractive and repulsive case. The investigation of the well-studied attractive Hubbard-model serve as a validation of the DCA⁺ algorithm as well as a strong indication that the superconducting transition exhibits the physics of a Klosterlitz Thouless transition. In the case of the repulsive Hubbard-model, we will show that the DCA⁺ algorithm can converge the superconducting transition temperature and that the wave-function of the Cooper pair has the distinctive d-wave momentum-structure. The quantitative convergence of T_c was up till now impossible with the DCA and an important step towards the phase-diagram calculations of the 2D Hubbard model.

relevant papers:

- P. Staar, T. A. Maier and T. C. Schulthess, *Dynamical cluster approximation with continuous lattice self-energy*, Phys. Rev. B 88, 115101 (2013)
- P. Staar, T. A. Maier and T. C. Schulthess, *Detecting phase-transitions in electronic lattice-models with DCA⁺*, to be submitted soon (2013)

4.1 Introduction

Since the discovery of the high-temperature copper based superconductors [11], the study of interacting electrons on a lattice has attracted a lot of attention. It was soon realized by Zhang and Rice [105] that these simple lattice models contained the essential physics of this novel class of superconductors and could potentially explain the pairing mechanism in these materials. The simplest lattice-model that exhibits qualitatively all the observed physical phases, is the single band Hubbard model [37]

$$H = \sum_{\vec{k}} \varepsilon(\vec{k}) c_{\vec{k}}^{\dagger} c_{\vec{k}} + U \sum_i n_i n_i \quad (4.1)$$

$$\varepsilon(\vec{k}) = -4t (\cos(k_x) + \cos(k_y))$$

Here, $c_{\vec{k}}^{(\dagger)}$ is the Fourier transform of the annihilation (creation) operator of an electron with spin σ on site i , while $n_{i,\sigma}$ corresponds to the occupation number operator. The dispersion $\varepsilon(\vec{k})$ describes the electrons on the lattice in the absence of any interactions. The parameters t and U represent respectively the hopping amplitude between the nearest neighbors on the lattice and the on-site Coulomb repulsion.

The DCA has been very successful in the qualitative explanation of the various well-known phases in the Hubbard model. It has shown that the hole doped model has a superconducting region where the superconducting gap has a d-wave symmetry [61]. In the low hole-doped region of the phase diagram, the DCA has also reproduced various tell-tale signs of the pseudo-gap physics [28], such as the momentum dependent gap formation.

The major challenge that the DCA currently faces, is its discrepancy on the solutions of the Bethe Salpeter equation for different clusters. If the self-consistency is obtained in the DCA with a Quantum Monte Carlo solver, the fermionic sign problem prevents us to solve large clusters at low temperatures. For large interaction strengths ($U/t \geq 4$), we are restricted to small clusters ($N_c \leq 32$) in order to solve the Hubbard model. In the DCA, the solutions of the Bethe-Salpeter equation for these clusters converge poorly [60].

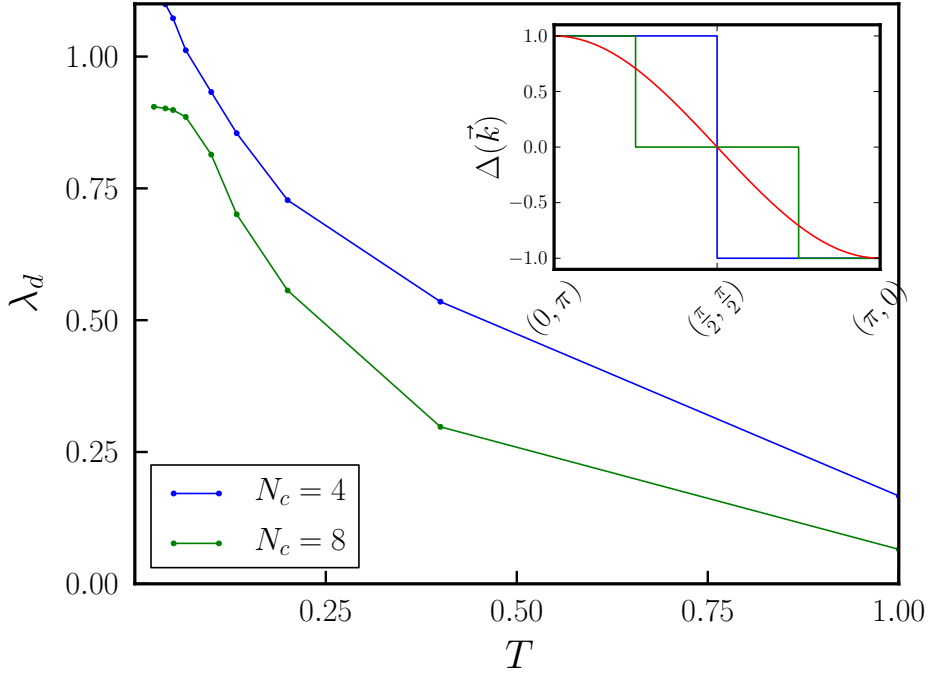


Figure 4.1: DCA description of the gap function $\Delta(k)$ in the 4- and 8-site cluster at 5% doping with $U/t = 8$. In the 4-site cluster, the gap will be either 1 or -1 along the Fermi-surface and thus clearly overestimate a d-wave gap of $\cos(k_x) - \cos(k_y)$ (red). In the 8-site cluster, a large section on the nodal area is zero, underestimating the d-wave gap. The overestimation in the 4-site leads to a superconducting phase transition (marked by a crossing of the leading eigenvalue through 1), while the underestimation of the gap in the 8-site cluster suppresses the superconducting phase transition.

This lack of convergence can be attributed to a purely geometric effect. Each cluster will evidently have a different number of k-points at different positions. In small clusters, these limited number of k-points can not adequately describe the superconducting gap-function $\Delta_{\vec{k}}$ in momentum space. Consequently, each cluster will overestimate the gap-function in certain areas of the Brillouin zone, while underestimate it in the other parts. This leads to very inconsistent transition temperatures for different clustersizes [60]. This geometric effect on the gap function is clearly illustrated in Fig. 4.1 by considering the two smallest clusters available. On the one hand, a 4-site cluster will overestimate a gap function with a d-wave symmetry, since the latter acquires its values at the extrema $[\pi, 0]$ and $[0, \pi]$. On the other hand, an 8-site cluster will underestimate the d-wave gap since the nodal area $[\pi/2, \pi/2]$ has to be zero due to the cluster-symmetry. Since the size of the gap-function

is proportional the transition temperature T_c , it is to be expected that the 4-site cluster overestimates the transition temperature, and the 8-site cluster underestimates the latter.

In the previous chapters, we have proposed algorithmic changes to the DCA self consistency loop as well as implementation changes to the CTAUX cluster-solver. In this chapter, we want to show how these improvements dramatically improve our capability to investigate the phase-diagram. We will focus in particular on the cluster-size dependence of the transition temperatures for anti-ferromagnetic and superconducting transition.

4.2 The anti-Ferromagnetic transition in the 2D repulsive Hubbard model.

For systems with a low dimensionality ($d \leq 2$), the Mermin-Wagner theorem states that a continuous symmetry can not be spontaneously broken at finite temperature. As a consequence, the observed antiferromagnetic phase transition at half filling in the DCA must be an anomaly, that arises from the finite size cluster approximation. A simple explanation can be given for this anomaly. As the temperature is lowered, the anti-ferromagnetic correlations grow exponentially and eventually cross the cluster-radius. At that point, the mean-field approximation breaks down and the DCA will report antiferromagnetic phase transition. A tell-tale sign for this phenomenon is the formation of large 'peaks' in the momentum space representation of the self-energy, around the anti-nodal points $\{\pm\pi, 0\}$ and $\{0, \pm\pi\}$. They induce a slow decay of the self-energy in real-space, which eventually will cross the cluster-radius. In the assumption that the correlations grow exponentially with temperature and that the cluster-radius can be approximated by $\sqrt{N_c}$, we expect that the Neel-temperature T_N will decay logarithmically,

$$\sqrt{N_c} \approx r_c \approx \alpha e^{\gamma/T_N} \rightarrow T_N \approx \frac{\gamma}{\log(\alpha^{-1} \sqrt{N_c})} \quad (4.2)$$

This picture is also valid in the case of the DCA⁺, and one should thus expect a logarithmic decay of the Neel temperature. In Fig. 4.2, we show the evolution of the Neel temperature T_N for increasing cluster-sizes and the accompanying logarithmic fit according to Eq. (4.2). In the inset of Fig. 4.2, we show the imaginary part of the self-energy at the anti-nodal-point $\{\pi, 0\}$ for various cluster-size at a temperature of $T = 0.25$. We observe that the divergence becomes stronger with increasing cluster-size, due to the inclusion of more correlations in the larger clusters.

4.3. Investigation of the pseudogap-region in the 2D repulsive Hubbard model.

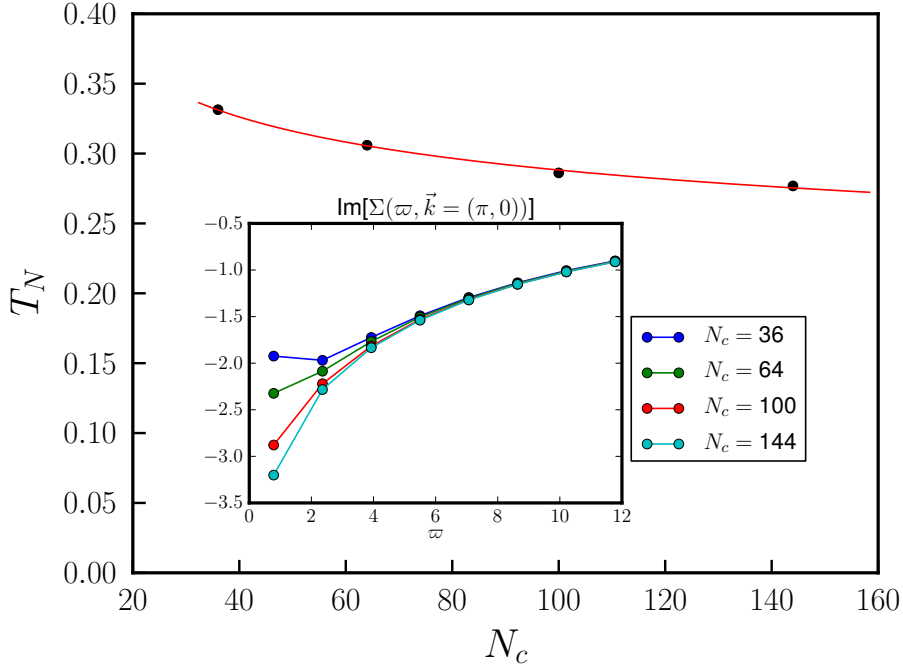


Figure 4.2: The Neel temperature T_N versus cluster-size for $U/t = 7$ at half-filling. Inset: the imaginary part of the self-energy at the anti-nodal point $\{\pi, 0\}$ for $T = 0.25$.

In order to show that the DCA⁺ captures the qualitative physics of the anti-ferromagnetic transition, we have plotted the antiferromagnetic gap-function, i.e. the eigenvector Φ associated with the leading eigenvalue, in momentum and frequency space in Fig. 4.3. Just as in the DCA [93], we can observe that the leading eigenvector is only mildly momentum-dependent along the Fermi-surface, which is indicative for a s-wave transition. For large Matsubara frequencies, we observe that the antiferromagnetic gap-function converges to a finite value. The anti-ferromagnetic transition can thus be characterized as a condensation of local particle-hole pairs (local magnetic moments). In addition, the eigenfunction has a clear finite asymptotic value. This reflects the instantaneous contribution of the Hubbard U to the effective interaction that leads to a magnetic moment formation.

4.3 Investigation of the pseudogap-region in the 2D repulsive Hubbard model.

One of the most distinctive features of the hole-doped cuprates is the emergence of a pseudogap [72], i.e. a partial suppression of the density of states

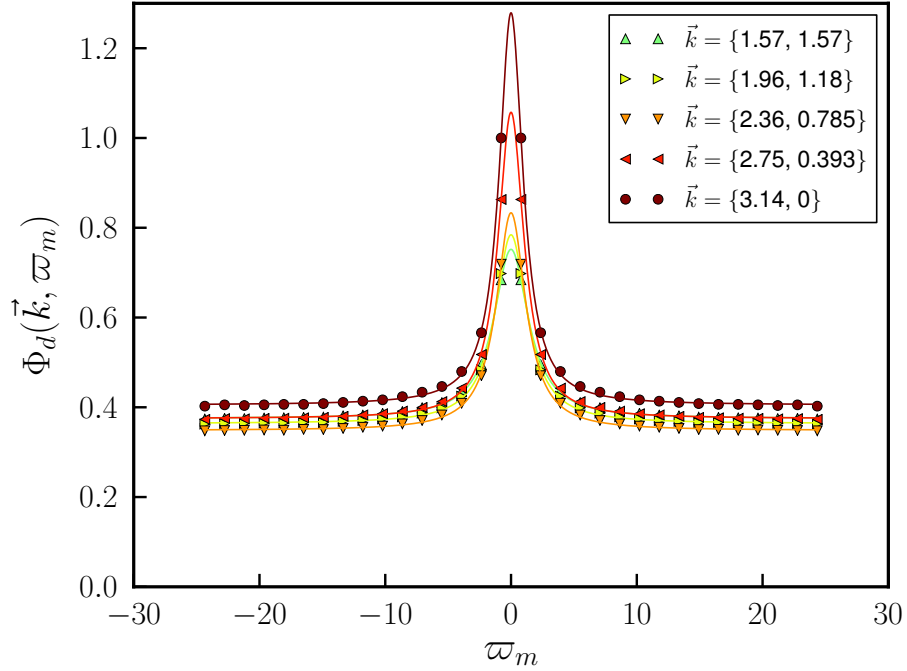


Figure 4.3: The leading eigenvector in the particle-hole channel for $U/t = 7$, $N_c = 144$ at half-filling close to the Neel transition.

at the Fermi energy at the antinodal points $(\pi, 0)$ and $(0, \pi)$ in the Brillouin zone. This state appears below a temperature T^* , which rises with decreasing hole doping as the Mott insulating half-filled state is approached. The detailed relation between the pseudogap and superconductivity remains controversial. Since superconductivity arises from the pseudogap state, it is generally believed that understanding this unusual phenomenon is an important prerequisite to understanding the pairing mechanism. Recent debate has been centered around the question of whether the pseudogap is a signature of superconducting fluctuations above T_c [21, 100] or whether it is a competing phase [95, 31].

Cluster dynamical mean field studies of the single-band Hubbard model have found a similar pseudogap opening up at the antinodal points at low temperatures in the low doping regime [62, 58, 77, 52, 13, 28]. In these calculations, the pseudogap originates from a strong momentum-space variation of the single-particle self-energy, which, as shown in recent DCA calculations by Gull et al. [28], gives rise to a momentum-sector-selective metal-insulator transition. The DCA⁺ improves upon the DCA algorithm in that it gives a self-energy with smooth and therefore more physical momentum dependence, and can therefore provide new insight into this problem. In

4.3. Investigation of the pseudogap-region in the 2D repulsive Hubbard model.

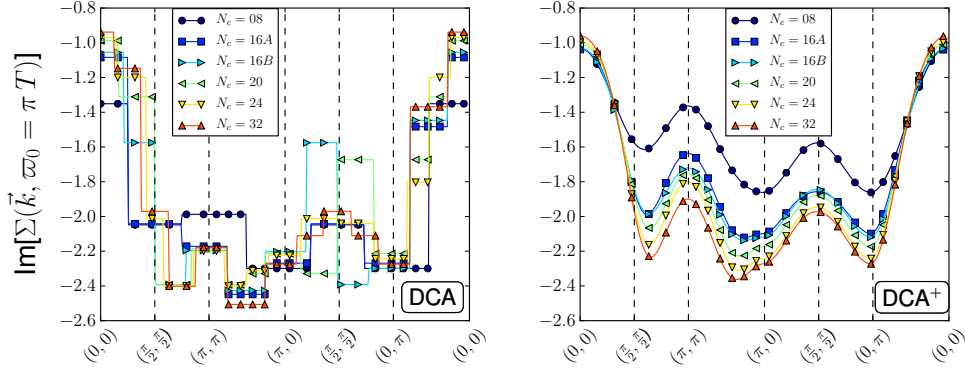


Figure 4.4: The imaginary part of the lattice self-energy for different clusters at a temperature of $T = 0.33$ with a hole-doping of 5% ($U/t = 7$ and $t'/t = -0.15$). Two key observations can be made. The DCA^+ produces for all clusters a lattice self-energy which follows the lattice symmetry. This is not true in the case of the DCA, which is illustrated in the region of $(\pi, 0)$ to $(0, \pi)$ for the clusters 16B, 20 and 24. One can also observe that the DCA^+ converges monotonically. The self-energy increases systematically with increasing cluster size as longer range correlations are taken into account. This systematic growth of the self-energy is harder to detect in the DCA. Therefore, we expect that the DCA^+ will lead to a more systematic convergence of other physical quantities, such as the pseudo gap transition temperature.

addition, since previous studies were limited to relatively small clusters up to 16 sites, it is important to explore whether the self-energy and pseudogap physics is converged on such clusters.

In Fig. 4.4, we plot the imaginary part of the lattice self-energy at the smallest Matsubara frequency $\omega_0 = \pi T$ for various clusters, computed with the DCA (left panel) and the DCA^+ (right panel). One immediately observes the much more physical smooth momentum dependence of the DCA^+ results versus the step-function-like nature of the DCA results for the self-energy. At closer inspection, one notices a much more systematic convergence of the DCA^+ results with different cluster size and geometry. While the DCA results for $\text{Im}\Sigma(\vec{K})$ show smaller spread at a given \vec{K} -point (e.g. at $\vec{K} = (\pi, 0)$), their cluster dependence is non-monotonic. In DCA^+ , in contrast, $|\text{Im}\Sigma(\vec{K})|$ monotonically increases with cluster size – a sensible result as longer ranged correlations are systematically taken into account.

Another striking feature of the DCA results is the asymmetry for clusters that do not have the full lattice symmetry such as the 16B, 20 and 24 site clusters. e.g., in the 16B cluster, the asymmetry around $(\pi/2, \pi/2)$ as one

4. STUDY OF PHASE-DIAGRAM OF THE 2D HUBBARD MODEL.

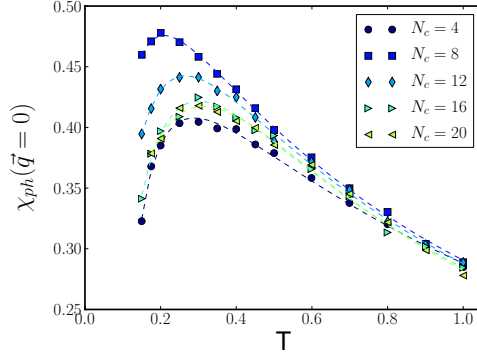


Figure 4.5: Uniform spin χ_{ph} susceptibilities vs temperature for different cluster computed in the DCA at 5 percent doping ($U/t = 7$ and $t'/t = -0.15$).

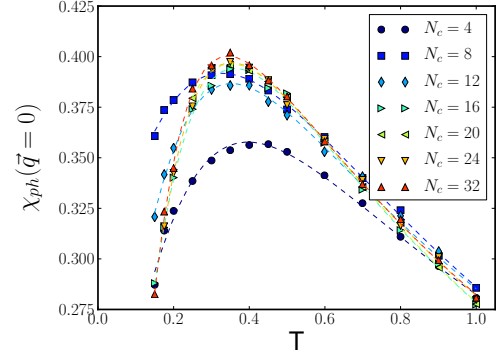


Figure 4.6: Uniform spin χ_{ph} susceptibilities vs temperature for different cluster computed in the DCA⁺ at 5 percent doping ($U/t = 7$ and $t'/t = -0.15$).

moves along the line from $(\pi, 0)$ to $(0, \pi)$ is apparent and the results in these regions are significantly different from those for the symmetric 16A cluster. This asymmetry results from the asymmetric arrangement of the two cluster K-points closest to $(\pi/2, \pi/2)$ with respect to $(\pi/2, \pi/2)$ (see right hand side of Fig. 2.1). This asymmetry is completely removed in the DCA⁺.

In addition, with the exception of a small region around (π, π) , the DCA⁺ results for the asymmetric 16B cluster are almost identical to the results of the fully symmetric 16A cluster. The DCA⁺ algorithm restores the full lattice symmetry in the results obtained from clusters that do not have the full symmetry and thus makes studies on these clusters much more useful. This, combined with the improved convergence as a function of cluster size allows for much more systematic and precise extrapolations to the exact infinite cluster size.

To further illustrate this point, we now turn to a study of the temperature T^* below which the pseudogap starts to form. Here, we define T^* as the maximum in the temperature dependence of the bulk ($q = 0$) magnetic (particle-hole, spin $S = 1$) susceptibility $\chi_{ph}(q = 0, T)$. The downturn in this quantity below T^* with decreasing temperature signals the suppression of low-energy spin excitations, which is also observed in experiments to accompany the opening of the pseudogap in the single-particle spectral weight. In the DCA and DCA⁺ algorithms, χ_{ph} is computed from the single and two-particle Greens-function G_{ph}^{II} obtained from the cluster-solver. Using the notation $K = (\vec{K}, \omega)$, the bare two-particle Greens-function $G_{0,ph}^{II}$ is constructed

4.3. Investigation of the pseudogap-region in the 2D repulsive Hubbard model.

from a pair of interacting cluster Greens functions (for $\vec{q} = 0$)

$$G_{0,ph}^{II}(K) = G(K) G(K),$$

while the fully renormalized two-particle Green's function G_{ph}^{II} is computed as

$$G_{ph}^{II}(K, K') = \left(\prod_{l=1}^4 \int_0^\beta d\tau_l \right) e^{i\omega_1(\tau_1 - \tau_2)} e^{i\omega_2(\tau_3 - \tau_4)} \\ \times \sum_{\sigma, \sigma' = \pm} \langle c_\sigma^\dagger(\vec{K}, \tau_1) c_\sigma(\vec{K}, \tau_2) c_{\sigma'}^\dagger(\vec{K}', \tau_3) c_{\sigma'}(\vec{K}', \tau_4) \rangle.$$

The irreducible cluster vertex function $\Gamma_{ph}(\vec{Q} = 0, \vec{K}, \vec{K}')$ is then obtained by inverting the Bethe-Salpeter equation on the cluster

$$\Gamma_{ph} = [G_{0,ph}^{II}]^{-1} - [G_{ph}^{II}]^{-1}, \quad (4.3)$$

where we used a matrix notation in the cluster momenta \vec{K} and \vec{K}' . The uniform lattice spin susceptibility $\chi_{ph}(q = 0)$ is then calculated from

$$\chi_{ph} = \sum_{K_1, K_2} \chi^0 [\mathbb{1} - \Gamma \chi^0]^{-1}.$$

Here, χ^0 is the coarse-grained bare susceptibility of the lattice,

$$\chi^0(K) = \int d\vec{k} \varphi_K(\vec{k}) G(\vec{k}) G(\vec{k})$$

This procedure to compute the uniform lattice spin susceptibility $\chi_{ph}(\vec{q} = 0)$ is the same in the DCA⁺ as in the DCA [39]. The quantities that enter these equations, however, are different between both approaches. In the DCA⁺, for thermodynamic consistency, one should apply the same interpolation procedure to the vertex function $\Gamma_{ph}(K, K')$ as is done for the self-energy. Here however, for the sake of simplicity and in order to focus on the effects of the self-energy, we keep the piecewise constant dependence of $\Gamma_{ph}(K, K')$ that is naturally obtained from its extraction from the cluster quantities in Eq. (4.3) as in the DCA. In the $S = 1$ particle-hole channel, where the leading correlations are antiferromagnetic and have only weak internal \vec{K} -dependence [17], we expect this to be a good approximation.

In Fig. 4.5, we show results for $\chi_{ph}(\vec{q} = 0)$ obtained with the DCA for different clusters. One observes a strong cluster size dependence and the results are not converged even for the largest cluster that can still be simulated before the fermionic sign problem begins to make the QMC sampling exponentially difficult. The corresponding DCA⁺ results are displayed in Fig. 4.6.

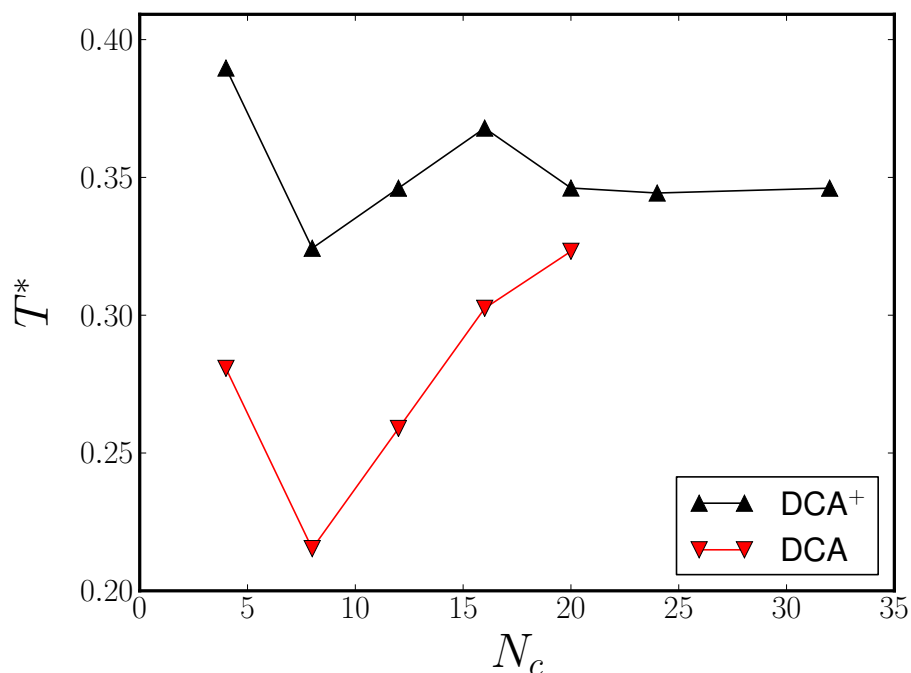


Figure 4.7: T^* versus clustersize computed in the DCA and DCA⁺ at 5 percent doping ($U/t = 7$ and $t'/t = -0.15$).

Here, convergence is reached much sooner. The location of the maximum in temperature dependence, T^* , is essentially independent of the cluster for $N_c \geq 8$ (see Fig. 4.7). As discussed previously, this directly results from the improved convergence of the self-energy in the DCA⁺. From these results, once the effects of cluster geometry are removed in the DCA⁺, it becomes clear that the underlying correlations that lead to the pseudogap formation are short-ranged and well contained in clusters of size 8.

4.4 Superconducting transition temperature T_c in 2D attractive Hubbard model.

The attractive Hubbard model has been studied extensively [67, 104] over the past three decades. Following the discovery of the high-temperature cuprates, this nontrivial toy-model has been used to shed light on the formation of Cooper pairs [88] and other exotic states of matter which arise from the correlation between electrons [70]. As this model does not suffer from a fermionic sign problem, large clusters can be solved and the phase diagram can be obtained accurately through a finite size scaling procedure.

4.4. Superconducting transition temperature T_c in 2D attractive Hubbard model.

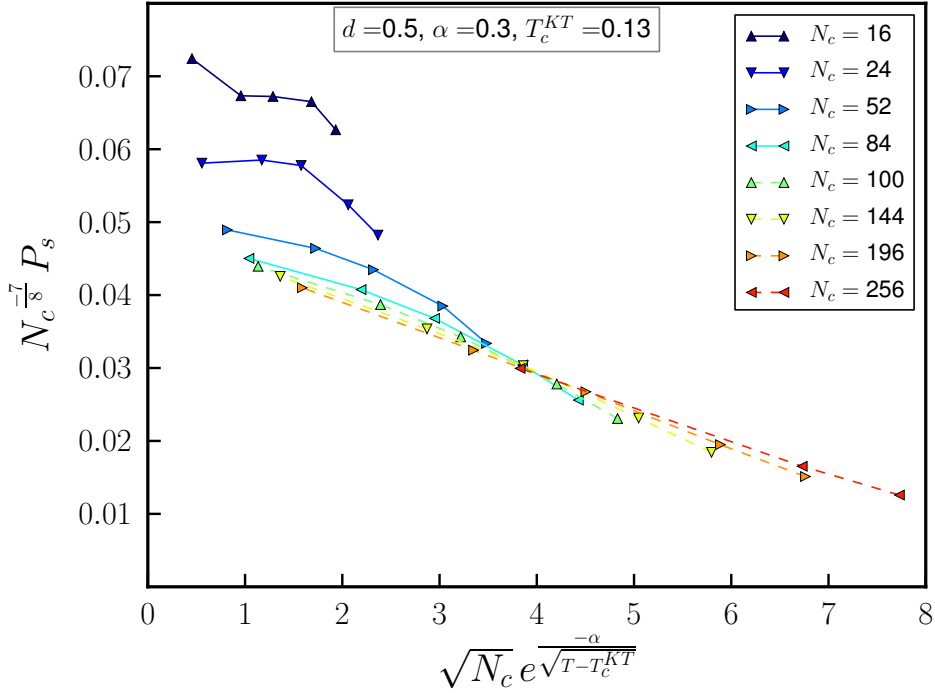


Figure 4.8: Data-collapse of the cluster-susceptibility P_s using a Klosterlitz-Thouless scaling law for a density of $d = 0.5$. We can observe a clear data-collapse for clusters with a cluster-size larger than 84.

The phase-diagram of the attractive Hubbard model with a interaction of $U = -4$ has been studied in detail by Paiva et. al. [76], using a determinantal QMC cluster solver [15, 87]. They used two independent observables to nail down the superconducting transition temperature T_c , namely a data-collapse of the cluster-susceptibility at the correct T_c due to the Klosterlitz-Thouless scaling-law and the universal-jump relation involving the helicity modulus of a two-dimensional superfluid [71]. Since both observables lead to the same transition temperatures, we can safely conclude the reported transition temperatures are valid reference points for this model.

The Klosterlitz-Thouless scaling-law dictates a data-collapse of the cluster-susceptibility versus cluster-size on the parametric curve \mathcal{C} for large enough clusters:

$$\mathcal{C} = \{ \sqrt{N_c} \exp(-\alpha/\sqrt{T - T_c^{KT}}), N_c^{-7/8} P_s \} \quad (4.4)$$

Here, the two parameters α and T_c^{KT} are fitting parameters, that are found

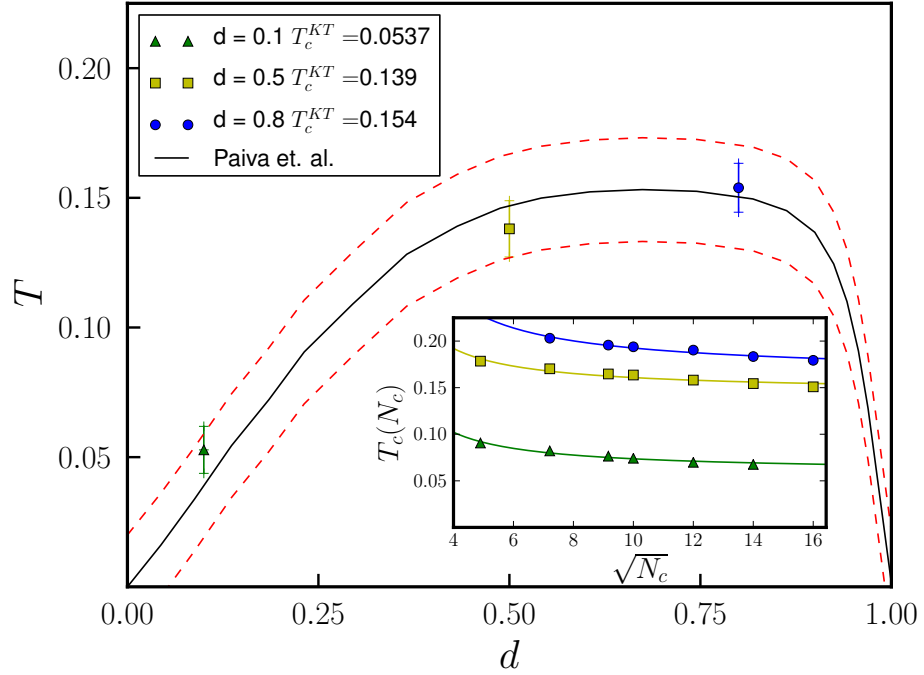


Figure 4.9: The phase-diagram of the attractive Hubbard model with $U = -4$. The DCA⁺ results lie within the error-bars (red-dotted lines) of previously reported values by Paiva et al.

by minimizing the spread of the data, in order to obtain the best data-collapse. This method has the advantage that it does not require us to compute the lattice-susceptibility. We can thus avoid the inversion of the vertex coarsegraining in Eq. (2.44). The cluster susceptibility P_s can be obtained by directly summing the two-particle cluster Greens functions G^{II} over all momentum and frequency variables. In Fig. 4.8, we have plotted the best data-collapse of the cluster-susceptibility P_s at 50% doping. The critical temperature $T_c^{KT} = 0.13$ obtained by the data-collapse is equal to the value obtained by Paiva et. al. The discrepancy on the α parameter (0.3 versus 0.1) can most likely be attributed to the mean-field character of the DCA algorithm.

In Fig. 4.9, we show the phase-diagram of the attractive Hubbard model with $U = -4$. The critical temperatures at the densities $d = 0.1, 0.5$ and 0.8 are obtained by fitting the Klosterlitz-Thouless scaling law of the critical temperature versus cluster-size:

4.5. Superconducting transition temperature T_c in 2D repulsive Hubbard model.

$$T_c(N_c) = T_c^{\text{KT}} + \frac{A}{(B + \log(\sqrt{N_c}))^2} \quad (4.5)$$

The fits are shown in the inset of Fig. 4.9. We can clearly observe a decay of the critical temperature with cluster-size. To investigate the robustness of the fit, we investigate the spread of the T_c^{KT} by omitting each data-point once from the data-set $\{N_c, T_c(N_c)\}$. This results in 6 slightly different T_c^{KT} for each density, from which we can compute the standard deviation. We represent this standard deviation as the error-bar on the T_c^{KT} fits in Fig. 4.9.

From Fig. 4.8 and Fig. 4.9, we can come to two important conclusions. First, the transition temperature that we obtain with the data-collapse of the cluster-susceptibility is in good agreement with the transition temperature obtained by the two-particle framework of the DCA^+ . We therefore obtain the same transition temperature with two different methods, one solely based on cluster-quantities (i.e. the single and two-particle Greens functions) and one based on the lattice-quantities, which are essentially obtained by inverting Eq. (2.32) for the lattice self-energy and Eq. (2.44) for the lattice vertex. As such, we can conclude that the proposed algorithm to invert the two-particle coarsegraining condition in Eq. (2.44) works correctly. Secondly, we can reproduce the phase-diagram of the attractive Hubbard model with a interaction of $U = -4$ presented by Paiva. As such, the two-particle framework of the DCA^+ is consistent with the literature for the attractive Hubbard model, which is a strong indication that framework works correctly.

4.5 Superconducting transition temperature T_c in 2D repulsive Hubbard model.

4.5.1 The superconducting transition for 10% hole doping at $U/t = 4$.

Through a careful investigation of the evolution of T_c versus the cluster size N_c , the DCA had predicted [60] a superconducting transition temperature T_c of approximately $0.023t$ in the 2D single band Hubbard model with a repulsive interaction of $U/t = 4$ and 10% percent hole-doping. In Fig. 4.10, we compare this evolution of T_c versus N_c with newly obtained results for the transition temperature with the DCA^+ . We can make three clear observations. First, the transition temperatures of the six largest clusters in the DCA^+ agree very well with the observed transition temperatures of the three largest clusters in the DCA. Consequently, the DCA^+ does not contradict quantitative results of the DCA, but rather confirms and clarifies earlier findings. Next, the DCA^+ can access much larger clusters than the

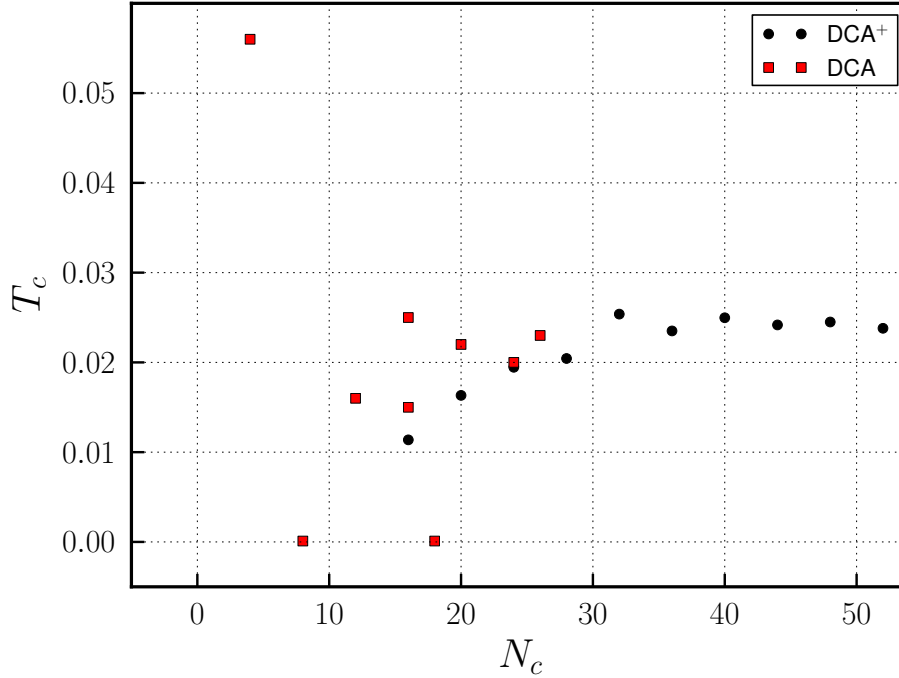


Figure 4.10: The superconducting transition temperature T_c versus cluster-size computed with the DCA and the DCA⁺. Due to a more favorable sign-problem in the DCA⁺, we can observe a consistent growth of T_c towards the extrapolated value of the DCA.

DCA. This is mainly due to the improved fermionic sign problem of the DCA⁺ algorithm. The access to larger clusters allows us to treat non-local correlations more accurately and thus implicitly converge T_c better. Third, we can observe a much more systematic convergence of T_c in the DCA⁺, a property already observed during the study of pseudo-gap temperature T^* . The transition temperature T_c in the interval of $N_c = 16$ to $N_c = 32$ rises monotonously and becomes flat for clusters with $N_c \geq 32$. If the effective T_c for the 16-site DCA-cluster is assumed to be the mean of the 16A and 16B site clusters in Fig. 4.10, the monotonic rise of T_c seems to be also present in the DCA with a little imagination. However, due to the inaccessibility of larger clusters with the DCA, it is very hard to judge whether the DCA transition temperatures are converged, or still rising. With the new DCA⁺ results, it becomes clear that T_c saturates around 0.024 ± 0.01 .

The monotonic rise of T_c can be attributed mainly to two factors. The smaller the cluster, the more the coarsegraining reduces the non-local correlations and thus lowers the transition temperature. This idea is enforced

4.5. Superconducting transition temperature T_c in 2D repulsive Hubbard model.

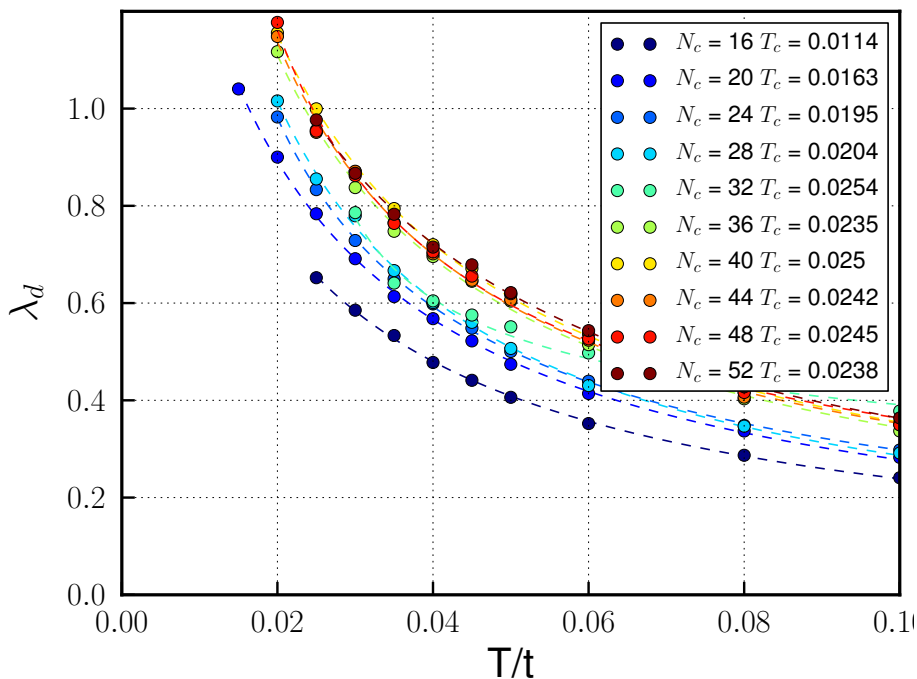


Figure 4.11: The leading eigenvalue at 10% doping for $U/t = 4$. The critical temperature T_c converges to $T_c \approx 0.024$ for clusters larger than 36.

by Fig. 4.11, where we show the leading eigenvalue versus temperature for various cluster-sizes. We can clearly observe a systematic growth of the leading eigenvalue for increasing cluster-size over a wide range of temperatures. Another factor that influences the transition temperature is the coherence length, i.e the 'size' of a Cooper pair. Recently, It was argued that the coherence length is relatively large for small interactions [59]. This could explain the discrepancy between the optimal charge-modulation wave-vector found in experiments and theory [59]. The large coherence length could also explain why there seem to be two regimes in Fig. 4.10, namely monotonic rise of T_c for $N_c \leq 32$ and a flat T_c for $N_c \geq 32$. In the first regime, the linear cluster size $L_c \approx \sqrt{N_c}$ is smaller than the coherence length. As such, the DCA⁺ neglects (spatial) phase fluctuations between Cooper-pairs completely, which would suppress T_c . But since pairs are correlated over larger distances than L_c , increasing L_c takes into account longer ranged pair-field correlations and therefore the pair-field susceptibility and thus T_c increases. This process is similar to what one observes in finite size calculations for the cluster correlation function [76], which increases monotonically with cluster size. In the second regime, linear cluster size L_c is larger than coherence length. In this regime, increasing L_c does not increase the pair-field suscep-

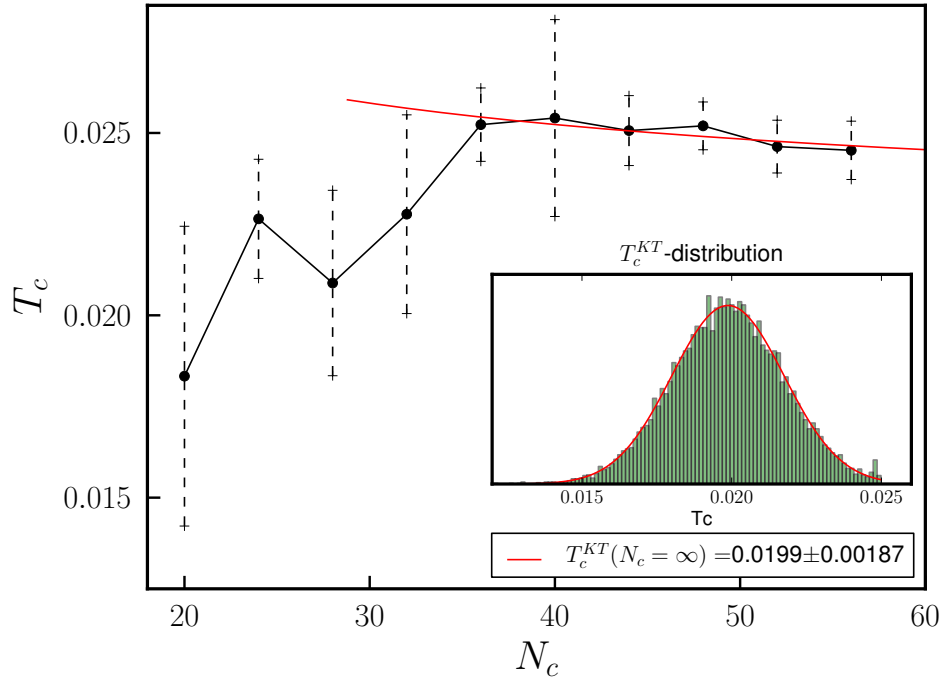


Figure 4.12: For each cluster-size, we show the average and standard-deviation of the superconducting transition temperature T_c of four different cluster-orientations ($U/t = 4$ and 10% doping). The red line shows the average fit of the Klosterlitz Thouless scaling law, given by Eq. (4.5). Inset: By generating random transition temperatures, which are Gaussian distributed around the mean value and lie within the standard-deviation, we can generate a distribution function for T_c^{KT} . This distribution is then used to obtain an estimate for the lattice transition temperature $T_c^{KT}(N_c = \infty) = 0.0199 \pm 0.002$.

tibility since pairs are correlated only over smaller distances than those set by L_c . But increasing L_c will take into account longer-ranged phase fluctuations and therefore T_c decreases with cluster size according to the Klosterlitz-Thouless scaling law given by Eq. (4.5). In the attractive Hubbard model, we can demonstrate this logarithmic decay clearly, because we can access very large clusters in the absence of the fermionic sign problem. In the repulsive case, the sign problem does not allow us to access such large clusters, in which case it is very hard to distinguish between a logarithmic decay or a simple constant function due to the limited range of available clusters.

With this picture in mind, the crossover between both regimes can give us a good estimate for the coherence length. If we assume that the transition tem-

perature becomes a constant once the cluster-radius exceeds the coherence-length, we could deduce from Fig. 4.10 that the coherence length is approximately $\sqrt{32/\pi} \approx 3.19$ lattice-spacings. Future work will indicate whether this *back-of-the-envelope* calculations are accurate estimates. Note that this estimate for the coherence length seems roughly consistent with the recent calculations of the striped clusters [59]. For the striped system, the enhancement of T_c is expected when the correlation length is equal to the stripe periodicity. For $U/t = 4$, one found an enhancement for a period of eight stripes, but not for a period of four stripes.

4.5.2 Signatures of a Klosterlitz-Thouless transition.

Phase transitions in strictly two-dimensional systems have been studied extensively in various models, such as the rotator model or the lattice Coulomb gas. By now, it is commonly accepted that phase transitions in two dimensions are of the Klosterlitz Thouless type[46]. In short, a Klosterlitz Thouless transition is characterized by the difference of the decay-rate of the correlation length above and below the transition temperature[24]. Above the transition temperature, we have an exponential decay of the correlation length, while below the transition temperature one observes a power-law decay of the correlation length. In finite size systems, this leads to a specific dependency of the transition temperature T_c as a function of the system-size or in our case the cluster-size N_c . The specific dependency is given by Eq. (4.5).

We would now like to make a connection between these theoretical findings and the superconducting transition observed with the DCA⁺ for the repulsive Hubbard model. Unlike the attractive model, where we could compute the transition temperatures for very large clusters and thus establish a strong indication for a KT-transition, we can only obtain the transition temperatures in the repulsive model for clusters with a size less than 56. Furthermore, the clusters with a size of 32 or less are in the regime where the coherence length is larger than the cluster-size and can thus not be used in order to establish a KT-transition. Consequently, we can only use clusters in the range of 36 to 56 to show a logarithmic decay of the transition, which is highly non-trivial. In Fig. 4.12, one can observe a small decay in T_c for $N_c \in \{32, \dots, 56\}$, but it would be too simplistic to simply fit Eq. (4.5) to this data in order to obtain T_c^{KT} , since we have very few data-points in a limited range. Furthermore, we would not know the error on the fitted T_c^{KT} . To address this issue, we compute for each cluster-size the transition temperature of four different clusters with a very small deconvolution cut-off for $\sigma^\varphi = 0.1$ (typically, we use a value of $\sigma^\varphi = 0.5$). By taking a small deconvolution cut-off, we amplify the cluster-dependency of the transition-temperature. Next, we compute the mean and standard deviation of the four transition temperatures to eliminate specific cluster-shape dependencies and

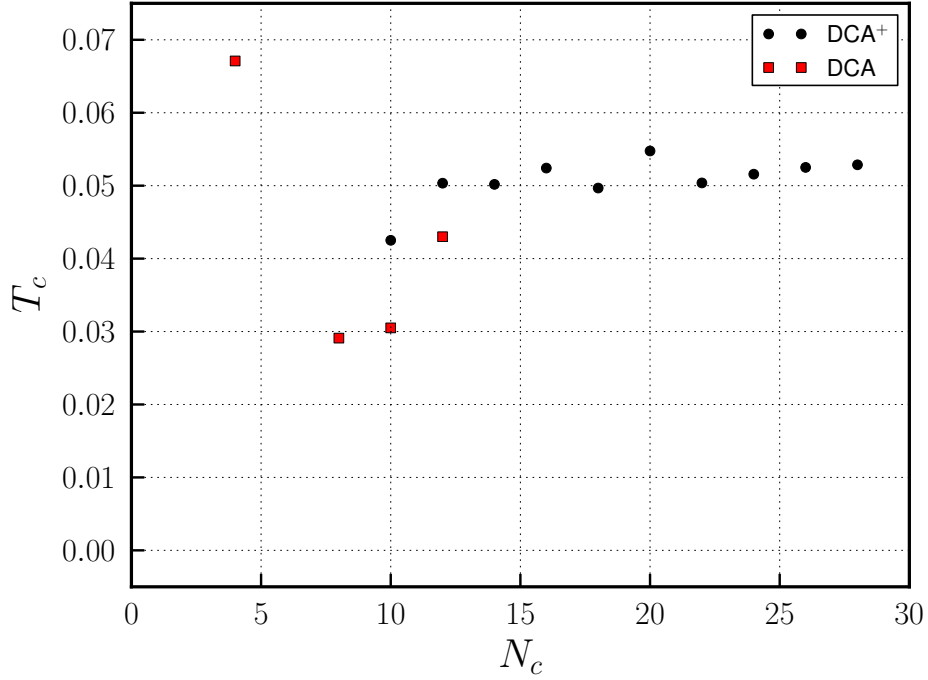


Figure 4.13: The superconducting transition temperature T_c versus cluster-size for $U/t = 7$ and 10% doping.

thus obtain a clean system-size dependent transition temperature, as well as its confidence intervals. The results are shown in Fig. 4.12, where the mean values are represented by the dots and the confidence intervals are given by a dashed line. In order to obtain an estimate for T_c^{KT} and its error, we now generate new transition temperatures for each cluster-size, which are gaussian distributed around the mean and lie in the confidence interval. For each of these newly generated set of transition temperatures, we perform a fit with Eq. (4.5) in order to obtain a T_c^{KT} . As such, we obtain a distribution for T_c^{KT} , which we show in the inset of Fig. 4.12. The obtained distribution for T_c^{KT} can be fitted perfectly with a Gaussian distribution with a mean of 0.0199 and a standard deviation of 0.002. The latter can be interpreted respectively as the superconducting transition temperature of the lattice and its respective error: $T_c^{KT}(N_c = \infty) = 0.0199 \pm 0.002$. The average fit to the data is shown in Fig. 4.12 with the red line.

4.5. Superconducting transition temperature T_c in 2D repulsive Hubbard model.

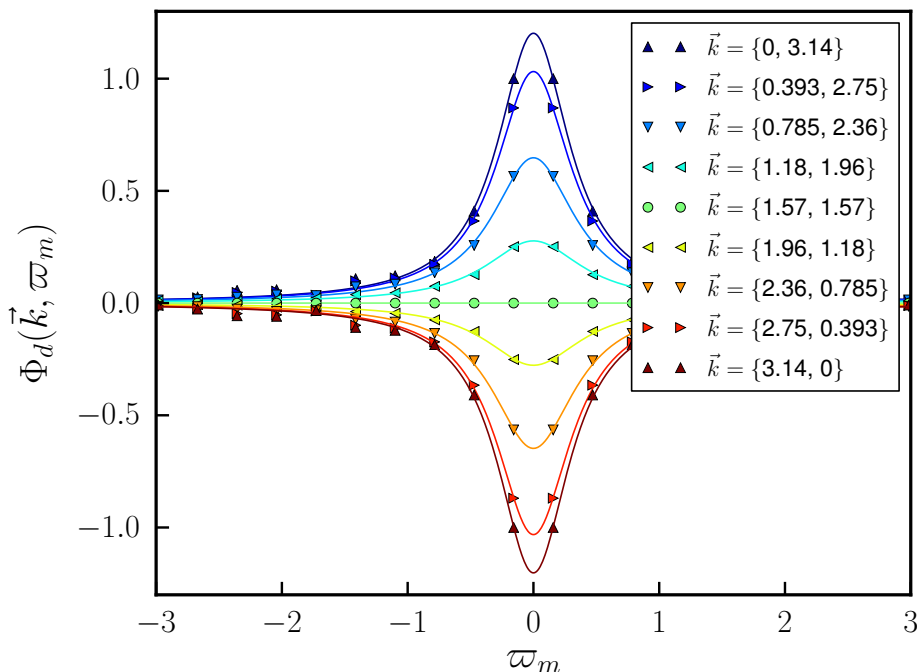


Figure 4.14: The leading eigenvector in the particle-particle channel for $U/t = 7$, $\beta = 20$, $N_c = 28$ and 10% doping. The d-wave structure is clearly visible.

4.5.3 The superconducting transition for 10% hole doping at $U/t = 7$.

In this section, we investigate the superconducting transition in the 2D Hubbard-model with a strong repulsive interaction of $U/t = 7$ and a finite hole-doping of 10%. This region of the phase-diagram is inaccessible with the DCA, due to an exponentially increasing fermionic sign problem [55]. For clusters with a size less than 28, the sign problem in the DCA⁺ is sufficiently delayed and becomes only problematic after T_c is reached. For this reason, it is impossible to compare the following results with previously published data.

In Fig. 4.13, we show the superconducting transition temperature T_c versus cluster-size. Just as in the weakly interacting case with a $U/t = 4$, we observe that the smallest cluster-sizes have a slightly smaller transition temperature, due to the coarser averaging of the lattice self-energy and lattice Greens-function. This reduces correlations on the finite size cluster and thus also T_c . Interestingly, we observe that the transition temperature T_c converges much faster with cluster-size N_c in the strongly interacting limit.

This is consistent with the coherence length picture we introduced in the last section. Intuitively, one would expect that the radius of the Cooper-pairs becomes smaller with increasing interaction strength, since the electrons become more localized. Following the same line of reasoning as in the weakly interacting regime, we estimate the coherence length to be of the order $\xi \approx \sqrt{12/\pi} = 1.95$ lattice-spacings.

In Fig. 4.14, we show the leading eigenvector $\Phi(\vec{k}, \omega)$, obtained after solving the Bethe-salpeter equation on a fine mesh of 128 k-points. We can clearly observe the d-wave structure along the Fermi-surface. The original goal of the paper, i.e. reduce the cluster-shape dependence of the leading eigenvector $\Phi(\vec{k}, \omega)$ in order to minimize fluctuations of the transition temperature, is thus achieved. Fig. 4.14 also illustrates nicely the frequency dependence of $\Phi(\vec{k}, \omega)$, which follows the typical bell-curve [61]. Although the leading eigenvector $\Phi(\vec{k}, \omega)$ is not a measurable quantity, its momentum and frequency dependence can reveal the structure of the pairing interaction that drives the formation of Cooper pairs in the superconducting state. Close to T_c , the effective pairing interaction can be reconstructed [63] from the the leading eigenvector $\Phi(\vec{k}, \omega)$,

$$\Gamma(\vec{k}, \omega, \vec{k}', \omega') \approx \alpha \Phi(\vec{k}, \omega) \Phi(\vec{k}', \omega') \quad (4.6)$$

Here, the parameter α is a fitting parameter, which indicates the strength of the interaction. After plugging in the approximation to $\Phi \approx (\cos(k_x) - \cos(k_y)) / (\gamma^2 + \omega^2) \equiv \varphi_d$, we obtain

$$\Gamma(\vec{k}, \omega, \vec{k}', \omega') \approx \alpha \frac{(\cos(k_x) - \cos(k_y)) (\cos(k'_x) - \cos(k'_y))}{(\gamma^2 + \omega^2)(\gamma^2 + \omega'^2)} \quad (4.7)$$

The vertex can now be Fourier transformed and we obtain a short-range, retarded effective interaction,

$$\begin{aligned} \Gamma(\vec{r}, \tau, \vec{r}', \tau') &\approx \alpha e^{-\gamma(|\tau|+|\tau'|)} \Delta(\vec{r}) \Delta(\vec{r}') \\ \Delta(\vec{r}) &= \frac{1}{2} \sum_{i=\pm 1} \delta(r_x - i) \delta(r_y) - \delta(r_x) \delta(r_y - i) \end{aligned} \quad (4.8)$$

After fitting φ_d to the leading eigenvector, we obtain a γ of approximately 0.5 ± 0.1 , which is in the range of $4t^2/U \approx 0.57$, predicted by Zhang and Rice.

Scaling and performance of DCA⁺ on leadership systems.

Abstract

In this chapter, we show how the DCA⁺ can be efficiently implemented on leadership systems. We discuss in detail how the application can be ported to multi-core and hybrid CPU-GPU systems and how this affects the scalability, performance and time or energy to solution. Furthermore, we discuss how the algorithmic improvements of the DCA⁺, i.e the incorporation of a continuous self-energy, lead to a better fermionic sign problem in the DCA⁺ than in the DCA. Due to this property, we estimate that the DCA⁺ improves the time-to-solution with a factor of 10^9 compared to the DCA in the case of a 28 site cluster in the 2D Hubbard model with $U/t = 7$. When running at scale on Titan at ORNL, the production runs scale optimally to 18,600 nodes for this set of parameters and we have measured sustained performance of up to 15.4 peta-flops, on Titan, which has a peak-performance of 27 peta-flops and Linpack performance of 17,6 peta-flops.

relevant papers:

- G. Alvarez, M. S. Summers, D. E. Maxwell, M. Eisenbach, J. S. Meredith, J. M. Larkin, J. Levesque, T. A. Maier, P. R. C. Kent, E. F. D'Azavedo and T. C. Schulthess. *New algorithm to enable 400+ tflop/s sustained performance in simulations of disorder effects in high- T_c superconductors*, Proceedings of the 2008 ACM/IEEE conference on Supercomputing, SC 2008, pages 61:161:10.
- P. Staar, T. A. Maier, R. Solca, G. Fourestey, M. Summers, T. C. Schulthess, *Taking a Quantum Leap in Time to Solution for Simulations of High- T_c Superconductors.*, accepted and to be published soon (2013)

5.1 Introduction

The rapidly increasing capability of computers in conjunction with the growing sophistication and efficiency of quantum Monte Carlo solvers has pushed the limits of simulations to larger cluster sizes and interaction strengths, as well as lower temperatures. As a result, the only serious barrier for quantum Monte Carlo calculations at low temperatures and away from certain parameter regimes (such as half-filling in the single-band Hubbard model) that remains is the fermionic sign problem[98], which leads to an exponentially growing statistical error with increasing system size and interaction strength, and decreasing temperature.

The sign problem has posed an insurmountable challenge to quantum Monte Carlo calculations of fermionic systems, especially for simulations of finite size systems, and remains a problem in the DCA approach. The DCA, however, was shown to have a less severe sign problem than finite size calculations [39], which, in the absence of a rigorous mathematical justification, was attributed to the action of the mean-field host on the cluster. This has enabled simulations of larger clusters at lower temperatures than those accessible with finite size simulations and thus has opened new possibilities for gaining insight into low temperature phenomena in correlated systems.

The DCA⁺ approach is different from the DCA in that it generates a more physical self-energy with smooth momentum dependence, and the correlations described by this self-energy are therefore shorter-ranged than those in the DCA. Hence, it is therefore not unreasonable to expect a difference in the severity of the sign problem between DCA⁺ and DCA.

In Fig. 5.1 we compare the fermionic sign σ_{qmc} between the DCA and the DCA⁺ for a 32-site cluster and $U = 7t$ for a doping of 5%. At low temperatures, the average sign in the DCA⁺ simulation is significantly larger than that of the DCA simulation. As indicated above, we attribute this improvement to the smooth momentum dependence of the DCA⁺ self-energy as compared to the step function dependence of the DCA self-energy. From Fourier analysis, one knows that the smoothness of a function is related to the rate of decay of its Fourier coefficients[43]. More precisely, if a function f is p times differentiable, then its Fourier components f_n will decay at least at a rate of $1/n^{p+1}$

$$f \in C^p \quad \rightarrow \quad |f_n| \leq \frac{|f^{(p)}|_1}{n^{p+1}}. \quad (5.1)$$

Since the DCA⁺ self-energy has smooth momentum dependence and not the step discontinuities of the DCA, its Fourier-transform to real space is

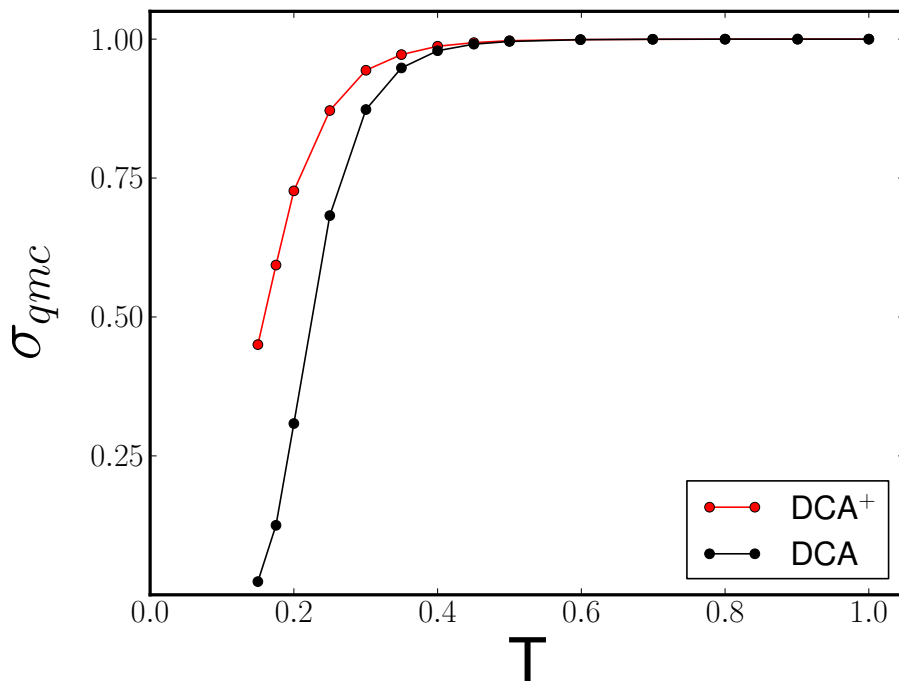


Figure 5.1: Temperature dependence of the average fermionic sign for $N_c = 32$ at 5 percent doping ($U/t = 7$ and $t'/t = -0.15$).

shorter-ranged than that of the DCA and the correlations it describes are shorter-ranged. We believe that it is this removal of unphysical long-range correlations, which reduces the sign problem in the DCA⁺. In any case, with this significant reduction in the severity of the sign problem, it is possible to study the physics of fermionic systems in even larger clusters and at lower temperatures than accessible with the DCA.

5.2 Implementation and method of performance measurements

Just as in state of the art DCA, the heart of the DCA⁺ simulations is the CT-AUX algorithm [29] with submatrix updates [33] and accumulation of measurements with non-equidistant fast Fourier transforms [93]. The usual way to parallelize Monte Carlo algorithms is to assign a Markov chain to every MPI rank, and one rank per compute core of a parallel computer. Measurements are performed in order with the Monte Carlo updates and accumulated on every core. Communication between ranks is limited to a reduction operation at the end of the Monte Carlo simulation – note that in

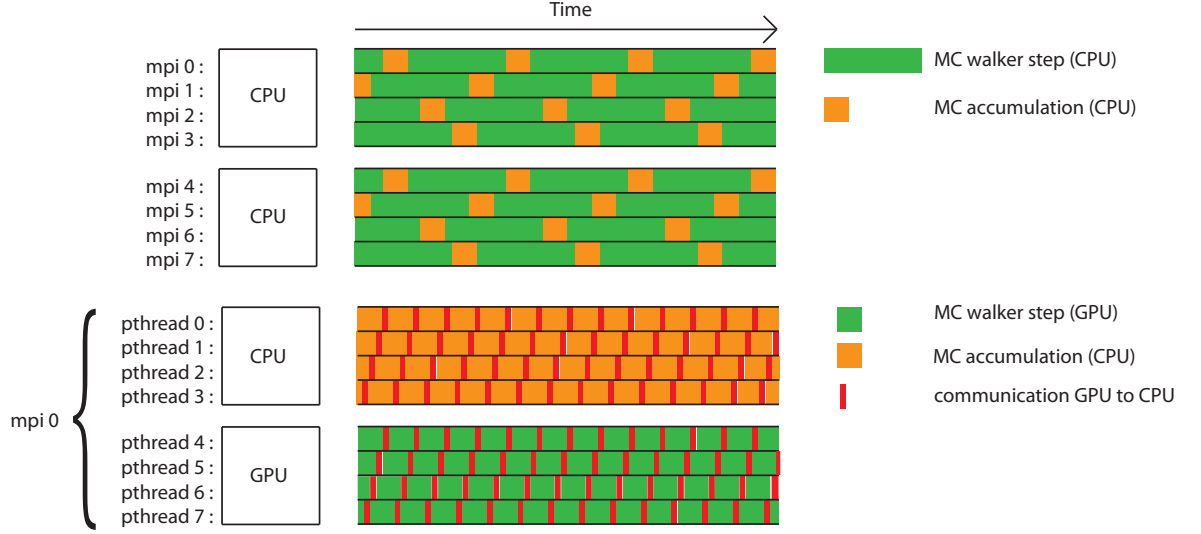


Figure 5.2: Schematic representation of the on-node parallelization of a conventional node ($2 \times \text{CPU}$) versus a hybrid-multicore node ($1 \times \text{CPU}$ and $1 \times \text{GPU}$).

the present case, the quantum Monte Carlo simulation is just one step inside the respective DCA and DCA⁺ iterations (see Algorithms 1 and 2). In light of modern machines with hybrid nodes consisting of multi-core CPU and GPU, we use a different implementation strategy. We run one MPI rank for each node and use $N_w + N_a$ pthreads per node, where N_w and N_a are, respectively, the numbers of walker and accumulator threads running on each node. On a multi-socket CPU node, the walker and accumulator threads are distributed evenly over the processors. On hybrid nodes, the compute intensive walker threads run on the GPU, since they consist mostly of matrix multiplications (see Fig. 3.2). The accumulators that execute measurements, which typically are more complex operations that benefit from latency optimized cores, run on the multi-core CPU. When a simulation starts up, all walkers begin from a random configuration running updates until the average expansion order $\langle k \rangle$ converges, at which point the particular walker is thermalized. At this point the stochastic sampling of the Green's function and other observables begins. Walkers send their data (the N -matrix) over to the pool of accumulator threads, where the measurements are processed asynchronously. On a hybrid system this involves transferring data from the GPU to the CPU over the PCIe bus. Should all accumulators be busy, the walker continues to update its configuration. However, given the speed of the measurements with non-equidistant fast Fourier transforms, the accumulators are typically ready to take on measurements before the

walkers are done with a minimum sweep of $\langle k \rangle$ updates required between measurements. This implementation as it runs on a hybrid CPU-GPU node is sketched in Fig. 5.2 and summarized in algorithm 3.

Algorithm 3 Hybrid-multicore implementation

```
1: Start with  $N_w$  walkers and  $N_a$  accumulators.
2: while walker is not thermalized do
3:   1 submatrix-update (GPU)
4: end while
5: repeat
6:   if walker then
7:     do  $\langle k \rangle / k_s$  submatrix-updates (GPU)
8:     while all accumulators are busy do
9:       1 submatrix-update (GPU)
10:    end while
11:   end if
12:   copy configuration from the walker (GPU) to the accumulator (CPU)
13:   if accumulator then
14:     do measurement (NFFT on CPU)
15:   end if
16: until all accumulators are finished
```

On the CPU only version of the code, the floating point performance is measured by counting all floating point operations with PAPI counters and dividing by the entire wallclock time of the *entire* simulation. Since such counters are not available on GPUs, a lower bound for the floating point operations performed when running simulations on a hybrid CPU-GPU system is computed analytically from the matrix dimensions used on the submatrix updates of the CT-AUX algorithm. Three DGEMM and one DTRSM operation are necessary for a submatrix update in each of the two spin channels. Two of these DGEMM are initialization steps. The actual update, represented in Fig. 3.2B, involves one DGEMM and one DTRSM. Each DGEMM will contribute $2k_s \langle k \rangle^2$ FLOPs, while the DTRSM accounts for $k_s^2 \langle k \rangle$ FLOPs. Comparing this lower bound estimate with identical simulations running on CPU-only system where we measure all floating point operations, we observe that the discrepancy is never larger than 5%.

5.3 Computer systems and performance model

We use a single code base for the implementation of the DCA and DCA⁺ algorithms (outer loop see algorithm 1 and 2), as well as the quantum Monte

Carlo cluster solver described in the previous section, on distributed multi-core and hybrid CPU-GPU systems. The code is implemented in C++ with template meta-programming techniques to hide architectural complexities in the quantum Monte Carlo implementation. We use MPI for inter-node parallelization, pthreads for the multi-threading on the nodes, and CUDA for the hybrid implementation. The simulations reported in this work have been executed on distributed multi-core and distributed hybrid CPU-GPU architectures. The following computer systems are used for the performance results we report in this and the next section:

Monte Rosa is a Cray XE6 distributed multi-core system at the Swiss National Supercomputing Center (CSCS) consisting of 1,496 compute nodes with two AMD Interlagos processors running at 2.1 GHz and 16 cores each. Each node is equipped with 32 GB DDR3-1600 RAM.

Todi is a Cray XK7 distributed hybrid CPU-GPU system at CSCS consisting of 272 compute nodes with one 16 core AMD Interlagos processor running at 2.1 GHz, and one NVIDIA K20X GPU that has 14 streaming multi-processors running at 732 MHz. The compute nodes are equipped with 32 GB DDR3-1600 memory and the GPU has 6 GB GDDR5 memory.

Titan is a Cray XK7 distributed hybrid CPU-GPU system at ORNL consisting of 18688 compute nodes with one 16 core AMD Interlagos processor running at 2.2 GHz, and one NVIDIA K20X GPU that has 14 streaming multi-processors running at 732 MHz. The compute nodes are equipped with 32 GB DDR3-1600 memory and the GPU has 6 GB GDDR5 memory.

Practically all the time of a fully self-consistent DCA⁽⁺⁾ calculation is spent in the CT-AUX cluster solver. In order to understand the performance of the code on different architectures, it is thus sufficient to analyze the quantum Monte Carlo (QMC) simulations. As discussed in the previous section, these simulations consist of a thermalization phase in which no measurements are done, and a measurement phase in which measurements of Green's function and other observables (such as the two particle vertex) are accumulated. At a given cluster size N_c and temperature T , the QMC simulation is thermalized when the average expansion order $\langle k \rangle$ stabilizes – note that $\langle k \rangle \propto N_c^3 T^{-3}$. Furthermore, in order to decorrelate the configurations between individual measurements, $\langle k \rangle$ updates have to be performed to the Green's function. Thus, the time needed to perform a QMC integration is characterized by the expansion order $\langle k \rangle$, the number of measurements needed to reach a desired accuracy, and the number of nodes that are available on the machine. We can empirically determine the thermalization time $\Delta_t(\langle k \rangle)$ and the time per measurement $\Delta_m(\langle k \rangle)$, i.e. time for $\langle k \rangle$ updates to the Green's function plus time for actual measurement. The parallel efficiency E for a given mean expansion order $\langle k \rangle$, number of nodes N_n , and necessary number of

measurements N_m is then given by

$$E(N_n, N_m, \langle k \rangle) = \frac{1}{N_n} \frac{\Delta_t(\langle k \rangle) + N_m \Delta_m(\langle k \rangle)}{\Delta_t(\langle k \rangle) + \frac{N_m}{N_n} \Delta_m(\langle k \rangle)}. \quad (5.2)$$

Consequently, the parallel efficiency remains high only as long as the number of measurements is large compared to the number of nodes used in the simulations. This is a typical Amdahl's Law behavior, where at large node counts the parallel efficiency drops at the moment that the parallel phase (measurements) becomes comparable to the serial phase (thermalization) of the simulation. A detailed comparison between this performance model and the real simulations at scale is given in Fig. 5.6 that will be discussed in the next section.

In Fig. 5.3 we show the time per measurement Δ_m when the algorithm is running on the CPU-only nodes of Monte Rosa and the hybrid CPU-GPU nodes of Todì. To be precise, the speed-up is the ratio between between Δ_m on an XE-6 node and an XK7 node.

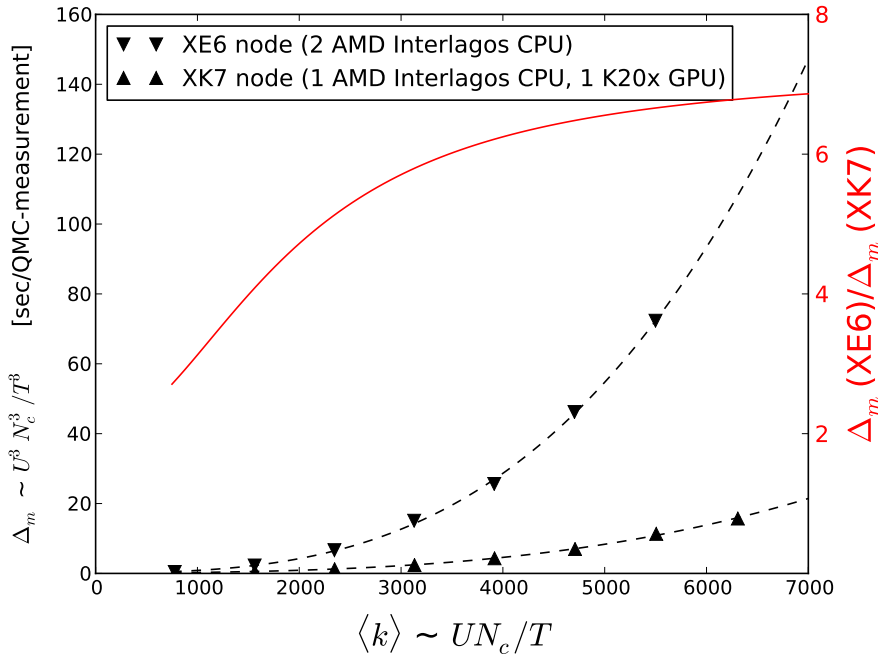


Figure 5.3: The seconds per measurement needed on a XE6 node (Monte Rosa) versus an XK7 node (Todì). The dotted lines are cubic fits to the data-points.

For any given cluster size, we have to run a sequence of $DCA^{(+)}$ simulations, starting at high temperature and cooling down to temperatures below T_c , as we can only determine the critical temperature from the point where the leading eigenvalue of the two-particle vertex equals unity and the pair-field susceptibility diverges. From Fig. (5.3), it becomes clear that running the simulations on the hybrid CPU-GPU architectures is in almost all cases preferable. With the exception of small expansion order $\langle k \rangle$ where the N-matrices fit into the cache of the CPU, we obtain a considerable speed-up with the hybrid-multicore implementation, mainly due to the superior performance of DGEMM on the GPU compared to on a CPU. In particular when the mean expansion order is high ($\langle k \rangle \geq 1000$), i.e. at low temperature and large cluster sizes, we observe a very significant speed-up on the hybrid system. Since this is the region where the superconducting transition occurs and where a large number of measurements are needed to suppress the sign problem for large clusters, we have to focus our efforts to obtain a maximum speed-up and efficiency in this parameter regime. Hence, running the simulations on hybrid CPU-GPU nodes pays off from a time to solution perspective. This is even more the case from an energy to solution perspective. We find that despite the higher performance, the energy consumption of the XK7 cabinet is about equal to that of the XE6.

A detailed comparison of the energy to solution, normalized per node and measurement, is given in Fig. (5.4), where the results are determined from power measurements of the entire cabinet (thus including network and all cooling devices) taken at millisecond intervals and integrated over the entire simulation cycle. Using the GPU-based XK7 dramatically reduced the energy cost of the simulation. Thus, all simulations to produce the results plotted in figure 4.13 and those we will analyze in the next section, were done on the Cray XK7 supercomputers Todi and Titan.

5.4 Performance results at scale

The most important benefit of the DCA^+ algorithm is the improvement of the fermionic sign problem for larger clusters at lower temperatures. It allows us to converge the superconducting transition temperature T_c as a function of cluster size N_c . This was discussed in detail in the previous chapter and the results for T_c are plotted in figure 4.13. We will now discuss how the simulations to compute T_c were done on the large-scale computer systems with the implementation we have discussed in section 5.2. Since the implementation is portable to multi-core and hybrid CPU-GPU systems and the performance model of section 5.3 is generic, our present discussion should apply to all of high-end computing systems in operation today.

The reduction of the sign problem is of crucial importance to the time to

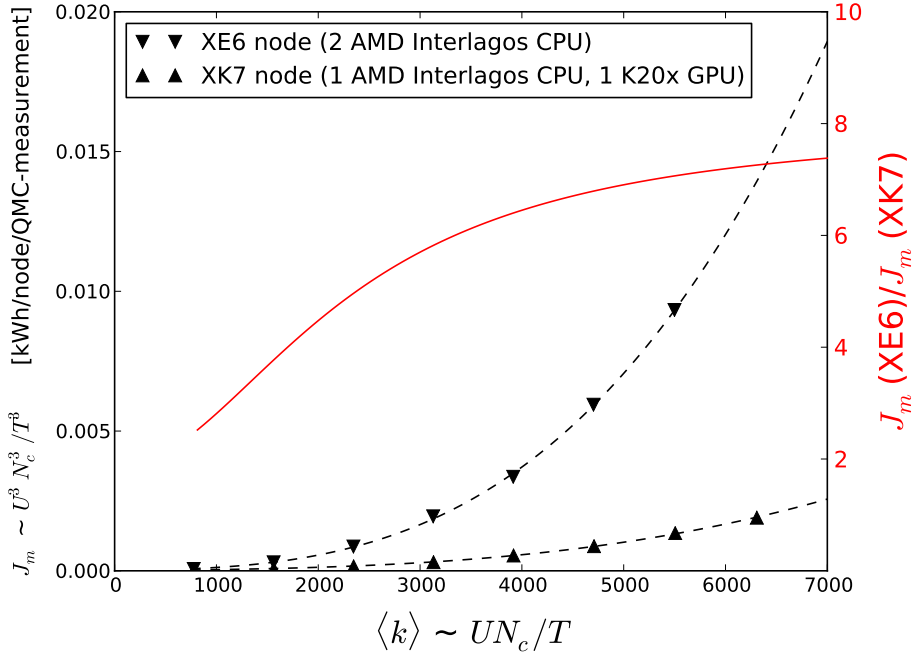


Figure 5.4: Energy (normalized by node and QMC measurement) needed to do a simulation on a XE6 (Monte Rosa) versus an XK7 node (Todi). The dotted lines are cubic fits to the data-points.

solution. From the central limit theorem, we know that the standard deviation on an accumulated observable, i.e. the accuracy, is proportional to the inverse square root of the number of measurements. In QMC simulations, the fermionic algebra introduces contributions with a negative weight, often interpreted as a negative probability. To take these negative weights into account, we need to divide the accumulated observable with the average sign of the weights. This becomes problematic in the case of a small average sign. If we assume a standard deviation on our observable of the order of $\sigma_O \approx 1$, a reasonable assumption since all observables have a magnitude of the order of 1, we obtain that the number of measurements needed for a desired accuracy ε is

$$N_m = \left(\frac{\sigma_O}{\sigma_{\text{QMC}} \varepsilon} \right)^2 \quad (5.3)$$

In order to obtain an estimate for the time-to-solution, we have to estimate two quantities: the time per measurement Δ_m and the fermionic sign. We know that the complexity of the time per measurement is cubic with inverse temperature $\Delta_m \propto T^{-3}$. In order to predict the fermionic sign, we fit a

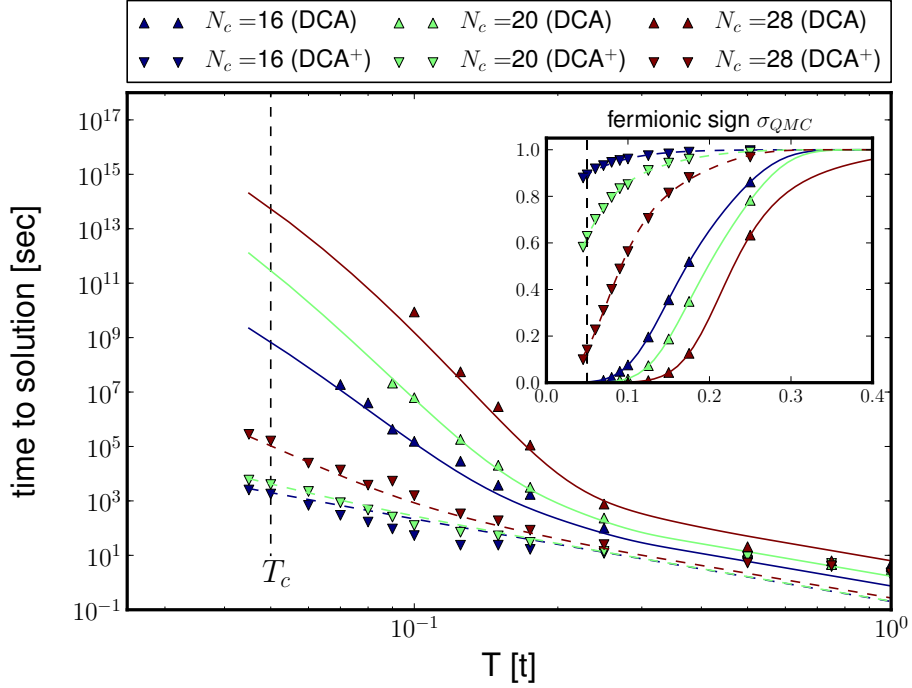


Figure 5.5: Comparison of the time to solution in the DCA and DCA⁺ for various clusters at an accuracy of $\varepsilon = 0.01$, at $U/t = 7$ and 10% doping. The solid and dotted lines are the estimated TTS according to Eq. (5.4). Inset: the evolution of the fermionic sign with temperature. The solid and dotted lines are the fits, used to generate the estimated TTS-curves.

Fermi-Dirac like function $(1 + \exp(-a(T - b)))^{-1}$ to the measured average sign, which sets the positive parameters a and b (see inset of Fig. [5.5]). By multiplying the *time per measurement* with the desired number of measurements to obtain an accuracy of ε , we arrive at an empirical formula for the time-to-solution (TTS) for a desired accuracy ε at a given temperature T ,

$$\text{TTS}(T, \varepsilon) \propto T^{-3} \left(\frac{\sigma_O}{\varepsilon} \right)^2 (1 + e^{-a(T-b)})^2 \quad (5.4)$$

There are two temperature regimes for the TTS. If $T > b$, the TTS will grow proportional T^{-3} since the fermionic sign will be close to 1. For $T < b$, the exponent will become more important and the TTS will grow exponentially. This can be clearly seen in figure 5.5, where the parameter b is approximately $\approx 0.2 - 0.25$ in the case of the DCA. Consequently, we can observe a kink in the log-log plot of the TTS for the DCA-simulations at those temperatures. In essence, the DCA⁺ moves the transition between polynomial to exponential TTS to lower temperature due to its favorable sign and thus

Table 5.1: Effect of the number of measurements on the error of the self-energy $\Sigma_{\vec{k}}$ and T_c for $N_c = 28, U/t = 7$.

# measurements	accuracy on $\Sigma_{\vec{k}}$	T_c
500k	0.03	0.0484 ± 0.004
10M	0.0074	0.0518 ± 0.0014

vastly improves the time to solution. Since we will never be able to run the DCA simulations at $U/t = 7$ and cluster sizes of $N_c = 12$ or larger with the machines we have available, we will have to estimate the TTS of the DCA from extrapolation down to T_c in figure 5.5. A comparison of the predicted TTS for the DCA⁺ runs with actual TTS in actual $N_c = 28$ runs at $T \approx T_c$, shows that we have the correct order of magnitude. We estimate that *the DCA⁺ algorithm improves the TTS of these runs by about 9 orders of magnitude compared to the state-of-the-art DCA runs*, using the same cluster solver and implementation in both methods.

The number of measurements necessary to reach a desired accuracy of $\varepsilon = 0.01$ in the DCA⁺ iterations at T_c , as estimated from eq. (5.3), is 10 million for $N_c = 28$ and $U/t = 7$, and 2.5 million for $N_c = 52$ and $U/t = 4$. These are the two largest, most time consuming runs we performed to produce the results plotted in figure 4.13. In table 5.1 we show for the measured ε_{QMC} is indeed in agreement with the desired value $\varepsilon = 0.01$ that we used in the measurements, and that this value is indeed reasonable to reach an accuracy on T_c of a few percent. If only 500 thousand measurements were used, the error on T_c would be closer to 10%. The error on T_c shown in the table where determined from five independent runs with different seeds.

We have measured the parallel efficiency by running two sets of simulations, one with 500 thousand and one with 10 million measurements for $N_c = 28$ and $U/t = 7$ parameter-set. In figure 5.6 we compare the actual TTS of these simulations with the predictions from equation (5.2) for various number of nodes. We can conclude that the scaling limitations of the simulations are entirely driven by Amdahl's law and the relative time taken by the thermalization in the QMC cluster solver.

For the remainder of this analysis, we use the ($N_c = 28, U/t = 7$) and ($N_c = 52, U/t = 4$) simulations to study the strong- and weak-scaling behavior. As indicated above, in order to reach a desired accuracy of $\varepsilon = 0.01$, we have to run 10 million measurements for the former and 2.5 million for the latter. The corresponding strong scaling plot is shown in Fig 5.7. The measured parallel efficiency for the ($N_c = 28, U/t = 7$) run at 18,600 nodes

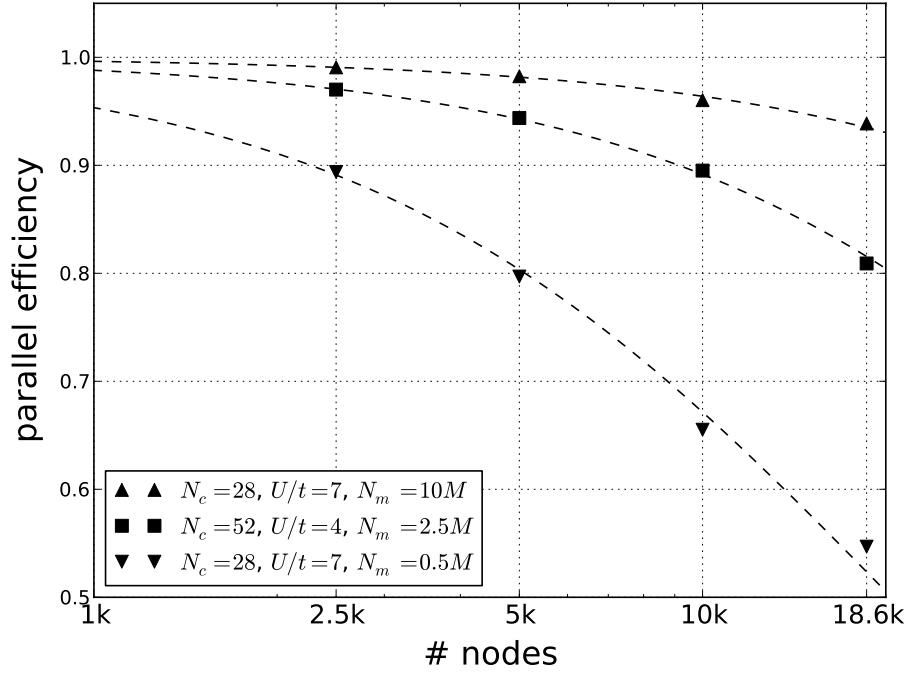


Figure 5.6: The parallel efficiency measured for different numbers of measurements in the strong ($U/t = 7$) and weak ($U/t = 4$) interaction limit. The dashed lines show the predictions of Eq. (5.2).

is 0.94, in good agreement with estimates based on Eq. (5.2). A floating point performance plotted was determined with the method discussed in section 5.2. At 18,600 nodes, the floating point performance is determined to be 0.94 for the 28 site cluster runs and 0.82 for the 52 site clusters. The relative difference in sustained performance is consistent with respective average expansion order $\langle k \rangle$ and corresponding matrix sizes used in the CT-AUX cluster solver.

For completeness, we also show weak scaling plots in figure 5.8. Here we start from the runs discussed above and same configurations used at 2,500 nodes in weak scaling experiments. The number of measurements are scaled proportionally with the number of nodes up to a maximum of 18,600. As expected, the time to solution remains constant. The sustained performance is 13.6 petaflops in the case of $N_c = 52$ and 9.7 petaflops when $N_c = 28$. The weak scaling plot indicate what we would have to do, if we ran with even larger clusters. In that case, we would have to increase the number of measurements even further to suppress the sign-problem. For example, if we were to run a 32-site cluster with $U/t = 7$, we estimate that we would need 100 million measurements, even more than the 10 million we used at 18,600 nodes in the strong scaling plot for $N_c = 28$. Furthermore, the 32-site

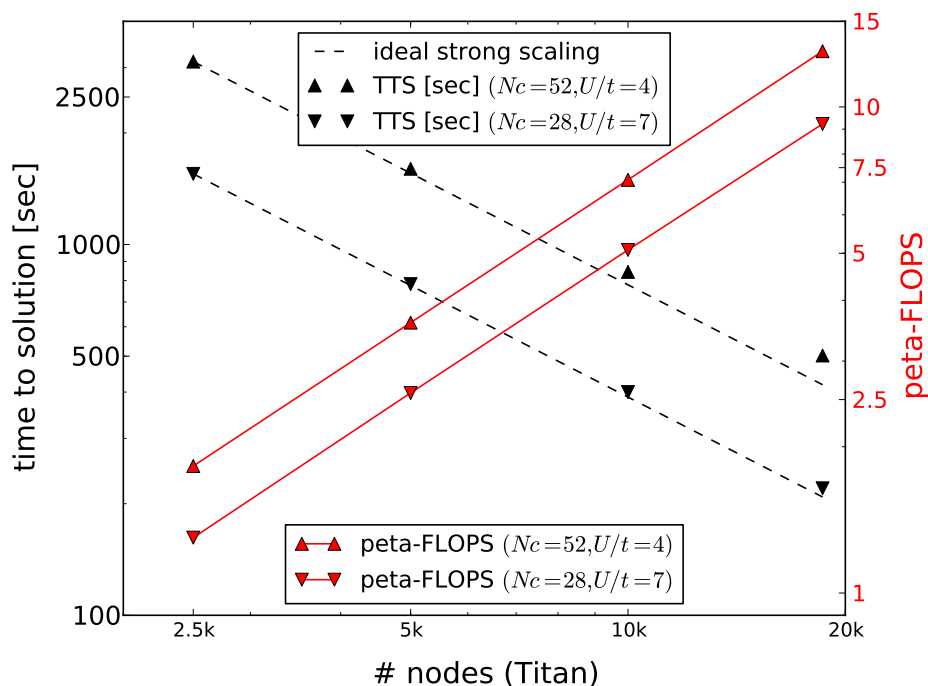


Figure 5.7: Strong scaling behavior for the largest clusters in the weak and strong interacting regime. The required 10 and 2.5 million measurements were used for $N_c = 28$ and $N_c = 52$, respectively, in order to reach a desired accuracy of $\varepsilon = 0.01$ in the DCA^+ iterations

runs will have a larger average expansion order and would thus take longer. We estimate that they would run for 100 minutes on 18,600 nodes on Titan.

The highest sustained performance in a full production run we have measured so far was 15.4 petaflops. This simulations ran on Titan (18,600 nodes) for 2250 seconds with a total energy consumption of 4300 kWh. It was recorded just prior to submission of the camera ready manuscript, while simulating the low doping region (5% hole-doping) of the Hubbard model in a 52-site cluster with $U/t = 7$. In this region of the phase-diagram, the lattice self-energy becomes strongly momentum dependent, thus requiring large clusters in order to have adequate momentum resolution. Had we done this run on a Cray XE6 with the same number of nodes but with multi-core processors only, we would have consumed 33,580 kWh and the time to solution would have been more than six hours.

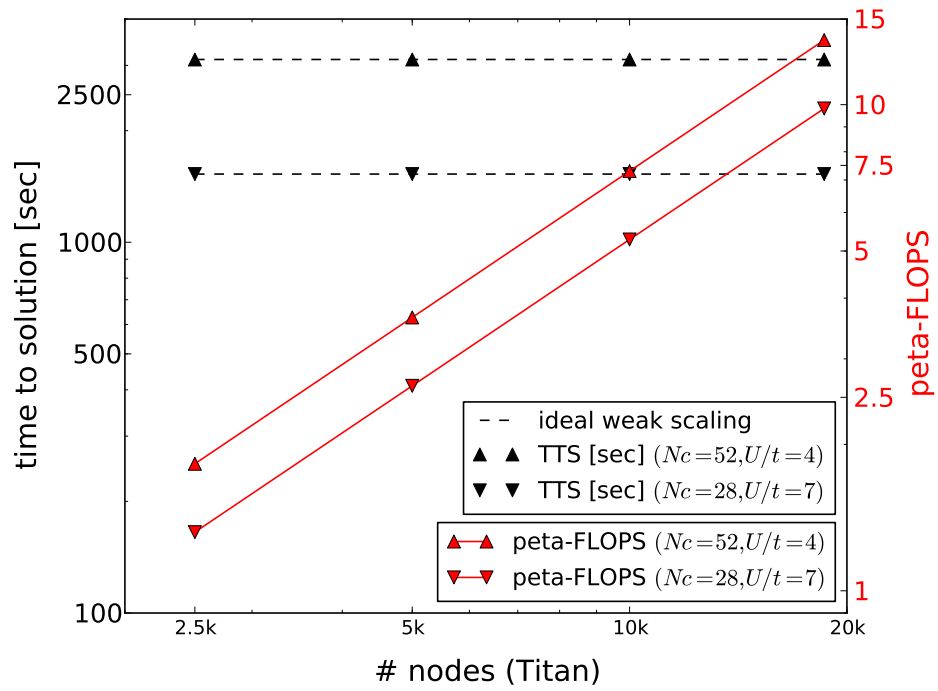


Figure 5.8: Weak scaling behavior for the largest clusters in the weak and strong interacting regime. The number of measurements are scaled proportionally with the number of nodes, with starting values at 2,500 node of 10 and 2.5 million for the $N_c = 28$ and $N_c = 52$ configurations, respectively.

Continuous-Pole-Expansion: A novel method to obtain the spectrum of electronic lattice models.

Abstract

Motivated by the development of the continuous time Quantum Monte Carlo impurity solvers that can directly accumulate the self-energy on the Matsubara frequencies, we present the continuous pole expansion algorithm (CPE). It can perform an analytical continuation of the self-energy located on the Matsubara frequencies to the real axis, which in turn allows us to probe the spectrum of the lattice-model, on which the original impurity-problem is modeled. Starting from the well-known analytical properties of the self-energy, the CPE rephrases the analytical continuation problem into a minimization problem with linear constraints. This minimization problem is inherently numerically stable and can be solved easily with the use of standard minimization methods. We approach the validation of the CPE in two different ways. First, we investigate how the self-energy and spectrum compare to exact diagonalization results on the real axis. In this way, we can identify the strengths and weaknesses of the proposed algorithm. Next, we will investigate some well-known problems which have been discussed in the literature in detail. To illustrate how the CPE can be used to investigate the momentum dependency of the spectrum, we apply the CPE in the 2D Hubbard model at half-filling and confirm the momentum dependent gap formation. Next, we illustrate the use of the CPE in real materials calculation, by computing the spectrum of NiO and comparing it with combined XPS, XES and BIS measurements.

relevant papers:

- P. Staar, B. Ydens, A. Kozhevnikov, J.-P. Locquet and T. C. Schulthess, *Continuous-Pole-Expansion: A novel method to obtain the spectrum of electronic lattice models.*, to be published soon (2013)

6.1 Introduction

One of the main tasks of modern condensed matter physics is the investigation of electronic lattice models with intermediate to strong correlations. Many of these systems are not tractable with controlled analytic approximations in the regimes of interest, so that numerical simulations need to be employed. Currently, the dynamical mean field theory (DMFT) [26] is the method of choice to investigate these type of problems. For practical purposes, the DMFT does not describe these models in real time, but rather in imaginary time. As a consequence, we can only indirectly access quantities on the real axis via an analytic continuation from the imaginary axis to the real axis.

There are currently two widely used methods to do an analytic continuation. The simplest and most unreliable one is the Pade-approximation[99, 6]. In this method, one fits a fractional polynomial to the data on the Matsubara frequencies. The analytic continuation is then obtained by simply evaluating the polynomial on the real axis, instead of the imaginary axis. In order to obtain interesting features, one generally needs a large fractional polynomial, which are notoriously unstable and violate the known analytical properties of the function. The second and much more successful method is the Maximum Entropy Method (MEM)[27, 40, 91]. This method analytically continues the imaginary time Greens function to the real frequency axis in order to obtain the spectrum \mathcal{A} . It is based on the relationship

$$G(\tau) = \frac{-1}{\pi} \int d\omega \underbrace{\frac{e^{-\tau\omega}}{1 + e^{-\beta\omega}}}_{=K(\omega,\tau)} \mathcal{A}(\omega). \quad (6.1)$$

A straightforward (numerical) inversion of Eq (6.1) is impossible, since the spectrum at large frequencies ($\omega \gg 1$) has only an exponentially small contribution to the imaginary time Greens function. Given a finite numerical precision, this means that there are many different spectral functions that all satisfy Eq (6.1). Without going into too much detail, the central idea in a MEM approach is to search a spectral function that satisfies Eq (6.1) and maximizes the information entropy \mathcal{S} [89], relative to a positive definite function $m(\omega)$ which has the correct high-frequency behavior

$$\mathcal{S} = - \int d\omega \mathcal{A}(\omega) - m(\omega) - \mathcal{A}(\omega) \log(\mathcal{A}(\omega)/m(\omega)). \quad (6.2)$$

The $m(\omega)$ function serves as the default model. In the absence of the constraint in Eq (6.1), maximizing the entropy will result in a spectrum $\mathcal{A}(\omega)$

equal to $m(\omega)$. For unknown systems, finding a good default model is not always a trivial matter.

With the introduction of continuous time Monte Carlo solvers [84, 101, 103, 29, 30], we are able to directly measure the self-energy on the Matsubara axis with unprecedented speed [33] and accuracy [93]. This motivated us to investigate the possibility of an analytic continuation of the self-energy directly in frequency space, using the relationship

$$\Sigma(z) = \Sigma_0 + \frac{1}{2\pi} \int_{-\infty}^{\infty} d\omega \underbrace{\frac{1}{\omega - z}}_{=T(\omega,z)} \text{Im}[\Sigma(\omega)]. \quad (6.3)$$

Performing the analytic continuation in frequency space is advantageous, since the ill-defined high-frequency behavior caused by the exponential decay in Eq. (6.1) can be avoided. This is easily demonstrated. We know that the high frequency part of the self-energy on the matsubara axis behaves like

$$\Sigma(\omega \gg 1) \approx \Sigma_0 - i \frac{\Sigma_1}{\omega} + \dots, \quad \Sigma_0, \Sigma_1 \in R \quad (6.4)$$

By performing a high-frequency expansion on the right hand side of Eq. (6.3) and equating this to Eq. (6.4), we can conclude that

$$\Sigma_1 = \int_{-\infty}^{\infty} d\omega \text{Im}[\Sigma(\omega)], \quad \text{Im}[\Sigma(\omega)] \leq 0. \quad (6.5)$$

Hence, the imaginary part of the self-energy has a finite L_1 -norm, since we also know from standard field theory [1] that the the imaginary part of the self-energy is strictly negative on the real axis. As such, we can conclude that it must decay fast on the real axis for large frequencies. Hence, the exponential decay of the transfer function $K(\omega, \tau)$ for large large frequencies is replaced by a polynomial decay of the new transfer function $T(\omega, \omega)$, simply by keeping the analytic continuation completely in the frequency domain. Despite the improvement to the ill-conditioned high-frequency problem on the real axis, inverting Eq. (6.3) can still not be done in a straightforward way. First of all, the numerical inversion of the transfer-matrix $T(\omega_i, \omega_j)$ is very unstable. Secondly, the self-energy is obtained in this paper using a Monte-Carlo algorithm. Therefore, the algorithm has to be robust enough to not be affected by statistical errors on the data and should not extract information

for the self-energy on the real axis from simple statistical noise. Thirdly, we know that the imaginary part of the self-energy has to be negative. Such a constraint is extremely difficult to enforce, while solving a linear system. For these reasons, we translate the inversion-problem of Eq. (6.3) into a minimization problem in this paper. The minimization function Λ is constructed as the L2-norm between the QMC-data and the computed self-energy on the Matsubara frequencies from a given strictly positive, real function f on the real axis. As such, the solution that corresponds to the minimum of the norm Λ corresponds also to the solution of Eq. (6.3). The advantage of translating the inversion problem into minimization algorithms, is not only with regard to the intrinsic robustness of these algorithms towards numerical errors, but also the relative ease with which strong constraints can be imposed on the solution. The goal of this paper is to investigate how to parametrize the function α in an efficient way and consequently present a viable implementation that can solve the constrained minimization problem.

A significant part of the paper will be spent on the validation of the CPE algorithm. Since the analytic continuation of a complex function is a non-trivial operation, we want to compare how the CPE performs, and observe its weaknesses as well as its strengths. First, we will validate the method via Exact Diagonalization (ED) on isolated clusters. As the name suggests, the ED allows us to compute the exact self-energy function on the imaginary and real axis for simple problems. A straightforward comparison is thus possible. Next, we want to apply the CPE to reproduce the spectrum of the single-band Hubbard model [37] at half-filling on a 32-site cluster in the DCA[35, 34, 39, 62]. We will validate a formula that is commonly used in the literature to probe the spectral density at the Fermi-energy. To illustrate how the CPE can be used to inspect the momentum-dependency of the spectrum, we will also investigate the momentum dependent gap formation. This topic has been recently investigated on small clusters [102, 32, 28], but without any conclusions on the spectral functions. We will show that the CPE arrives at the same conclusions as in the literature and investigate the spectral functions more closely. At last, we apply the CPE to the NiO compound, a well studied material. As such, we demonstrate how the orbital dependent spectrum can be computed with the CPE. We will also validate the results of the CPE versus XPS, XES and BIS measurements. As there are no exact results for the impurity problem, experimental data is the next best thing to validate the CPE algorithm. We will show a remarkable good agreement between theory and experiment.

6.2 Analytical properties of Fermionic Green's function and self-energy

We shortly review the analytical properties of the single-particle Greens-function and self-energy for Fermionic systems. We follow closely the argumentation of Abrikosov, Gorkov and Dzyaloshinski[1]. These properties will be used in the next section to motivate the Continuous Pole Expansion (CPE) of the self-energy. As is well known in field theory, the single-particle propagator G is defined as

$$G(\vec{k}, \tau) = \langle T_\tau [c_{\vec{k}}^\dagger(\tau) c_{\vec{k}}(0)] \rangle. \quad (6.6)$$

Here, τ represents the imaginary time and lives in the interval $[-\beta, \beta]$. For notational convenience, we will omit the momentum vector \vec{k} , as it does not contribute to the argument. For a Fermionic Greens-function, the value for $\tau < 0$ is related to the value for $\tau > 0$ via the simple relationship $G(\tau + \beta) = -G(\tau)$, due to the time-ordering operator. Consequently, the Fourier transform of the Fermionic Greens-function is only non-zero on the Matsubara frequencies $\omega_m = \pi/\beta (2m + 1)$ with $m \in \mathbb{Z}$ and we have that

$$G(\omega_m) = \int_0^\beta d\tau e^{i\omega_m \tau} G(\tau). \quad (6.7)$$

Standard complex analysis teaches us that there exists a unique, analytical function that coincides the infinite sequence $\{i\omega_m, G(\omega_m)\}$ in the complex plane¹. As such, we define the Greens-function $G(z)$ on the entire complex plane as the unique analytical continuation of this infinite sequence. Furthermore, a straightforward expansion of Eq. (6.6) in terms of the eigen-energies and eigen-basis of the system reveal that there exists a positive, integrable, real function $\rho(\omega)$ such that the Greens-function on the real axis can be obtained as,

$$G(\omega_m) = \int_{-\infty}^{+\infty} d\omega' \frac{\rho(\omega')}{\omega' - \omega_m}. \quad (6.8)$$

¹We refer here to the interior uniqueness properties of single valued complex functions from <http://www.encyclopediaofmath.org>: Let \mathcal{D} be a domain in the complex plane \mathbb{C} . The classical interior uniqueness theorem for holomorphic, i.e. single-valued analytic, functions on \mathcal{D} states that if two holomorphic functions $f(z)$ and $g(z)$ in \mathcal{D} coincide on some set $\mathcal{E} \subset \mathcal{D}$ containing at least one limit point in \mathcal{D} , then $f(z) = g(z)$ everywhere in \mathcal{D} .

6. CONTINUOUS-POLE-EXPANSION: A NOVEL METHOD TO OBTAIN THE SPECTRUM OF ELECTRONIC LATTICE MODELS.

Due the uniqueness property, we can generalize Eq. (6.8) to anywhere in the (upper) complex plane and obtain

$$G(z) = \int_{-\infty}^{+\infty} d\omega' \frac{\rho(\omega')}{\omega' - z}. \quad (6.9)$$

Since ρ is a real and positive function, we can logically deduce from Eq.(6.9) that the following analytical properties hold for the Greens-function,

$$\begin{aligned} \text{Im}[G(\omega + i\varpi)] &< 0 \text{ if } \varpi > 0. \\ G^I(i\varpi) &= \overline{G^I(-i\varpi)} \end{aligned} \quad (6.10)$$

As such, one notices that the single particle propagator can only have complex zeros on the real axis. The self-energy Σ is related to the Greens-function via the Dyson equation,

$$\Sigma(z) = G_0^{-1}(z) - G^{-1}(z). \quad (6.11)$$

Since $G(z)$ and $G_0(z)$ have no zero's in the upper complex plane, we know that their inversion can not introduce any poles in the upper plane of the self-energy. Hence, the self-energy is also analytic in the upper complex plane, with the possible exception on the real axis. The lack of poles in the upper complex plane allows us to use the residue theorem

$$\Sigma(z) = \frac{1}{2\pi i} \lim_{\delta \rightarrow 0^+} \int_{-\infty}^{\infty} d\omega \frac{\Sigma(\omega + i\delta)}{\omega - z}. \quad (6.12)$$

From the causality requirement on the self-energy, we also know that the imaginary part of the self-energy must be negative anywhere in the upper complex plane. The causality property, combined with the Kramers-Kronig relationships then result in the identity,

$$\begin{aligned} \Sigma(z) &= \frac{1}{2\pi} \lim_{\delta \rightarrow 0^+} \int_{-\infty}^{\infty} d\omega \frac{\text{Im}[\Sigma(\omega + i\delta)]}{\omega - z}, \\ \lim_{\delta \rightarrow 0^+} \text{Im}[\Sigma(\omega + i\delta)] &< 0 \end{aligned} \quad (6.13)$$

6.3 Continuous pole expansion for the self-energy

Motivated by Eq. (6.13), we can parametrize the self-energy on the Matsubara frequencies with a positive, real function f ,

$$\begin{aligned}\tilde{\Sigma}(\omega_m) &= \Sigma_0 + \int_{-\infty}^{\infty} d\omega \frac{f(\omega)}{i\omega_m - \omega}, \\ \text{with } f &\geq 0, \Sigma_0 \in \mathbb{R}, \int_{-\infty}^{\infty} dx f(x) = \Sigma_1.\end{aligned}\quad (6.14)$$

The goal of the CPE-algorithm is to search for the positive function f , that minimizes the norm Λ ,

$$\Lambda(f) = \sum_{m=0}^M \left| \tilde{\Sigma}(\omega_m) - \Sigma(\omega_m) \right|^2. \quad (6.15)$$

In order to find f , we will decompose it in the basis of a regular spaced, piecewise linear function. If $\{\omega_n = n \Delta/N\}$ for $n \in \{-N, \dots, N\}$ forms our regular spaced grid on the real axis, we can define the decomposition explicitly with the help of the step-function θ ,

$$\begin{aligned}f(\omega) &= \sum_{n=-N}^N \alpha_n \varphi_n(\omega) \quad \text{with } \alpha_n \geq 0, \\ \varphi_n(\omega) &= \theta(\omega - \omega_{n-1}) \theta(\omega_n - \omega) \frac{\omega - \omega_{n-1}}{\omega_n - \omega_{n-1}} \\ &\quad + \theta(\omega - \omega_n) \theta(\omega_{n+1} - \omega) \frac{\omega_{n+1} - \omega}{\omega_{n+1} - \omega_n}.\end{aligned}\quad (6.16)$$

Due to this explicit decomposition, we can perform the integral in Eq. (6.14) analytically and rewrite $\tilde{\Sigma}(z)$ into a much simpler form

$$\begin{aligned}\tilde{\Sigma}(z) &= \Sigma_0 + \sum_{n=-N}^N \Phi_n(z) \alpha_n \quad \text{with } \alpha_n \geq 0, \\ \Phi_n(z) &= \frac{\omega_{n-1} - z}{\omega_{n-1} - \omega_n} \log \left(\frac{\omega_{n-1} - z}{\omega_n - z} \right) \\ &\quad - \frac{\omega_{n+1} - z}{\omega_n - \omega_{n+1}} \log \left(\frac{z - \omega_n}{z - \omega_{n+1}} \right)\end{aligned}\quad (6.17)$$

6. CONTINUOUS-POLE-EXPANSION: A NOVEL METHOD TO OBTAIN THE SPECTRUM OF ELECTRONIC LATTICE MODELS.

We can now define a transfer matrix $A_{m,n} = \Phi_n(i\omega_m)$ and rewrite the norm Λ into a least square problem with boundary conditions,

$$\Lambda = \sum_{m=0}^M \left| \Sigma_0 + \sum_{n=-N}^N A_{m,n} \alpha_n - \Sigma(i\omega_m) \right|^2, \quad \alpha_n \geq 0.$$

By expanding the norm and gathering the terms of the same order in α_n , we obtain an explicit quadratic form for the norm Λ as a function of the constant transfer matrix $A_{m,n}$ and the coefficients Σ_0 and $\{\alpha_n\}$,

$$\begin{aligned} \Lambda &= M \Sigma_0^2 - 2 \Sigma_0 \sum_{m=0}^{M-1} \text{Re}[\Sigma(i\omega_m)] \\ &\quad + \vec{\alpha} Q \vec{\alpha}^T + \vec{q} \vec{\alpha}^T + C, \end{aligned} \tag{6.18}$$

$$Q = \left(\text{Im}[A]^T \text{Im}[A] + \text{Re}[A]^T \text{Re}[A] \right)$$

$$\vec{q} = 2 \left((\Sigma_0 - \text{Re}[\vec{\Sigma}]) \text{Re}[A] - \text{Im}[\vec{\Sigma}] \text{Im}[A] \right)$$

$$\vec{\alpha} = \{\alpha_{-N}, \dots, \alpha_N\} \text{ and}$$

$$\vec{\Sigma} = \{\Sigma(i\omega_0), \dots, \Sigma(i\omega_M)\}.$$

Hence, the CPE algorithm rephrases the problem of analytic continuation of a noisy function to a quadratic programmable optimization problem, with linear constraints. These type of problems are well known, and a multiple algorithms exists to find the minimum. From Eqs. (6.18), it follows that Q is positive semi-definite and according to Eq. (6.15), Λ has a trivial lower bound. In a a quadratic programmable optimization problem, these conditions are sufficient to guarantee a unique solution for which our norm Λ is minimized. Consequently, given a Δ , an N and an M , there is a *unique* set of $\{\alpha_n\}$ and Σ_0 for which our norm Λ is minimized. The Frank-Wolf algorithm[22] (FWA) is the most simple algorithm, aimed at solving a quadratic programmable optimization problem. We will discuss here its implementation for the CPE-algorithm: First, we subtract the zeroth moment Σ_0 of the measured self-energy Σ . This ensures integrability of Σ and $\vec{\Sigma}$ along the real axis. Next, we choose an initial set of $\{\alpha\}$, and compute the gradient of Λ towards $\{\alpha_n\}$ and Σ_0 ,

$$\begin{aligned}
 \vec{\nabla}_{\{\alpha\}} \Lambda &= 2 \operatorname{Im}[A]^T \left(\operatorname{Im}[A] \vec{\alpha} - \operatorname{Im}[\vec{\Sigma}] \right) \\
 &\quad + 2 \operatorname{Re}[A]^T \left(\operatorname{Re}[A] \vec{\alpha} + \Sigma_0 - \operatorname{Re}[\vec{\Sigma}] \right). \\
 \frac{\partial \Lambda}{\partial \Sigma_0} &= 2 \sum_{m=0}^{M-1} \left(\operatorname{Re}[A] \vec{\alpha} + \Sigma_0 - \operatorname{Re}[\Sigma(i \omega_m)] \right)
 \end{aligned} \tag{6.19}$$

Notice that the initial guess of $\{\alpha_n\}$ is irrelevant, since there is only 1 minimum in our convex search-space. We now search a λ , that minimizes the norm Λ along the direction of $-\vec{\nabla}_{\{\alpha\}} \Lambda$. Special care has to be taken to enforce positivity of all coefficients $\{\alpha\}$. This is accomplished by pointwise application of the ρ ramp-function².

$$\begin{aligned}
 \vec{\Sigma}(\lambda) &= A \rho(\vec{\alpha} - \lambda \vec{\nabla}_{\{\alpha\}} \Lambda) \\
 \Lambda(\lambda) &= \sum_{m=0}^M \left(\operatorname{Im}[\vec{\Sigma}(\lambda) - \vec{\Sigma}] \right)^2 + \left(\operatorname{Re}[\vec{\Sigma}(\lambda) - \vec{\Sigma}] \right)^2.
 \end{aligned} \tag{6.20}$$

The parameter λ_{min} that minimizes our norm, can now be used to generate a new set of coefficients $\{\alpha\}$,

$$\vec{\alpha}_{i+1} = \rho(\vec{\alpha}_i - \lambda_{min} \vec{\nabla}_{\{\alpha_i\}} \Lambda) \tag{6.21}$$

We continue this iterative process until Λ is *numerically* converged to a minimum value. This minimization approach in the CPE-algorithm has major benefits compared to other algorithms. First, the CPE-algorithm depends only on 3 *external* parameters Δ , N and M , if we do not take into account the to be fitted self-energy points on the imaginary axis. Furthermore, for these 3 parameters, there is a *unique* solution, since the norm can be rewritten as a quadratic function with a positive semi-definite kernel-matrix A . Second, CPE is numerically stable against white noise on the measured self-energy Σ , since we use a fitting procedure. This robustness is important in the DMFT context, where the self-energy is computed via a statistical process. Third, CPE is a self-consistent method, which returns a *goodness-of-fit* measure via Λ . This measure can be used to adjust the *external* parameters.

6. CONTINUOUS-POLE-EXPANSION: A NOVEL METHOD TO OBTAIN THE SPECTRUM OF ELECTRONIC LATTICE MODELS.

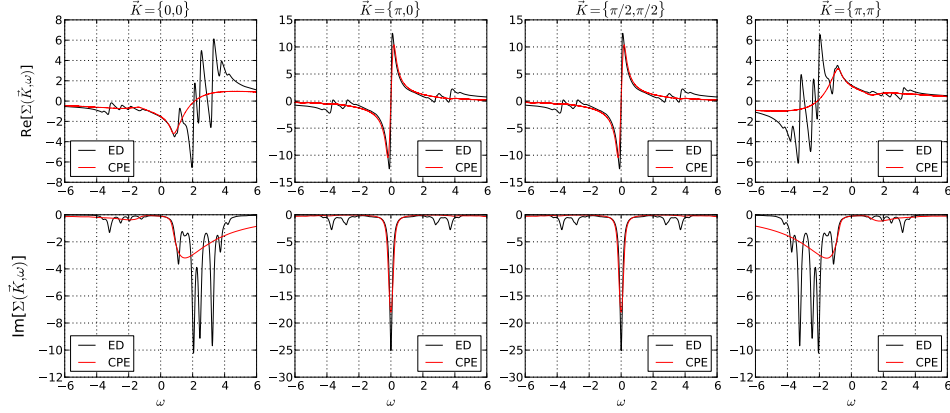


Figure 6.1: Comparison the real and imaginary part of the self-energy $\Sigma(\vec{K}, \omega)$ obtained with ED as well as with CPE. We observe that the CPE can capture the self-energy remarkably well around the Fermi-energy ($\omega = 0$), as well as the broad features far away from it.

6.4 Validation of CPE with Exact Diagonalization.

Since the analytical continuation of a complex function is a non-trivial task, a proper validation of the algorithm is absolutely essential. To this end, we would like to discuss in detail how the CPE performs for exactly solvable models. With exact diagonalization (ED), we can currently solve the single band Hubbard model on an isolated 8-site cluster. Due to the absence of the coupling to the bath, the the Hamiltonian has a finite number of term and is represented as

$$\mathcal{H} = -t \sum_{\sigma=\uparrow,\downarrow} \sum_{\langle i,j \rangle=1}^8 c_{i,\sigma}^\dagger c_{j,\sigma} + \frac{U}{2} \sum_{\sigma=\uparrow,\downarrow} \sum_{i=1}^8 (n_{i,\sigma} - 1/2)(n_{i,-\sigma} - 1/2)$$

The Hamiltonian acts on a Fock-space, composed of $2^{16} = 65536$ states. After applying total number and magnetization symmetries, the matrix can be block-diagonalized with a maximum block-size of 4900. Using standard eigenvalue decomposition routines of LAPACK, we can obtain all the eigenenergies $\{\varepsilon_i\}$ and eigenstates $\{|\Psi_i\rangle\}$ of the isolated 8-site cluster. Following standard many-body theory, we can now compute the Greens-function anywhere in the (upper) complex plane

²<http://mathworld.wolfram.com/RampFunction.html>

$$G(\nu, \mu, z) = \sum_{i,j} \frac{e^{-\beta \varepsilon_i} \langle \Psi_i | c_\nu | \Psi_j \rangle \langle \Psi_j | c_\mu^\dagger | \Psi_i \rangle}{\mathcal{Z} (z - \varepsilon_i + \varepsilon_j)}. \quad (6.22)$$

Here, the symbols ν and μ are short-hand notations for the band, spin and cluster K-point $\nu = \{b_\nu, s_\nu, \vec{K}_\nu\}$. By solving the cluster twice, once with the interaction switched on and once with the interaction switched off, we can obtain respectively the interacting and non-interacting Greens-function. From these two functions, we can obtain the self-energy in momentum space through the Dyson equation anywhere in the complex plane,

$$\Sigma(\vec{K}, z) = G_0^{-1}(\vec{K}, z) - G^{-1}(\vec{K}, z) \quad (6.23)$$

The idea is now to evaluate the self-energy on the real axis and on the Matsubara frequencies, located on the imaginary axis. In this way, we can use the self-energy on the Matsubara frequencies as an input for the CPE, and compare the analytically continued self-energy with the exact result.

In Fig. 6.1, we show the self-energy for various \vec{K} -points on the real axis, with an off-set of $\delta = 0.1i$. By comparing the ED results with the analytically continued self-energy, we can observe clearly the strengths and weaknesses of the CPE. Looking at the imaginary part of the self-energy, we can clearly observe that the high-frequency behavior of the self-energy decays smoothly and does not diverge. We can also see that the CPE can capture the self-energy remarkably well around the Fermi-energy ($\omega = 0$), as well as the broad features far away from it. However, sharp features can not be captured adequately. This is clear from the imaginary part of the self-energy at $\vec{K} = \{\pi, 0\}$. The divergence at the Fermi-energy is underestimated and the features at the interval $\omega = [-4, -2]$ are absent in the CPE-self-energy.

Consequently, one should therefore not expect to be able to determine sharp features in the spectrum with the CPE far from the Fermi-surface. Only broad features can be captured accurately far from the Fermi-surface. This is illustrated by Fig. 6.2, where we compare the spectrum obtained with ED as well as with CPE. One can clearly observe that the gap around the Fermi-surface is well represented by the CPE, as well as the broad Hubbard-bands at $\omega \approx \pm 3$.

In lattice models, we can safely assume that the spectrum is smoother than in finite size clusters, since we have an infinite number of eigenvalues instead of a finite set. The finite set of eigenvalues introduces poles with a finite weight on the real axis and thus originates the sharp features observed in

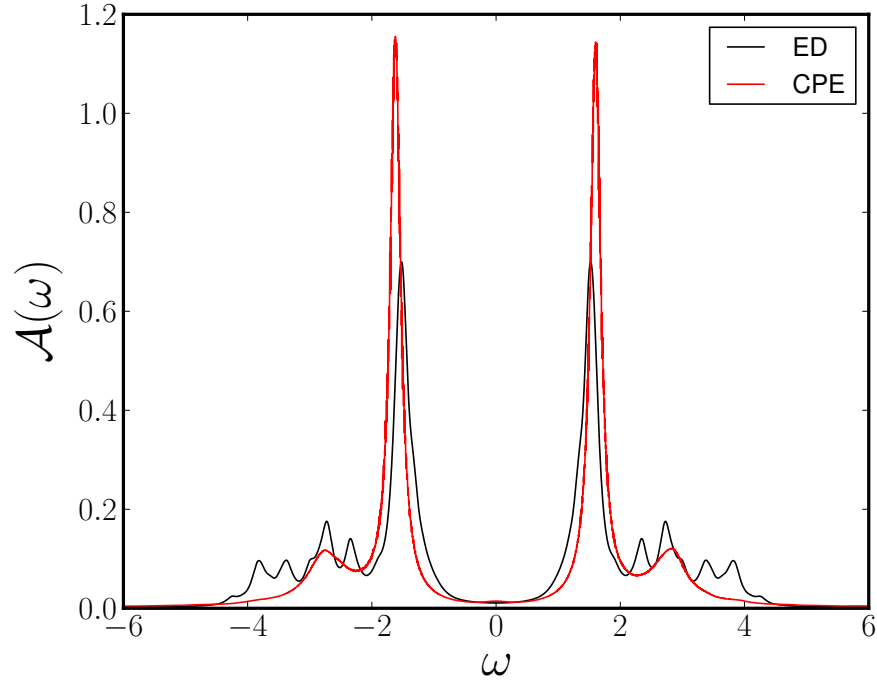


Figure 6.2: Comparison of the spectrum obtained with ED as well as with CPE. One can clearly observe that the gap around the Fermi-surface is well represented by the CPE, as well as the broad Hubbard-bands at $\omega \approx \pm 3$.

Fig. 6.1 and Fig 6.2. As a consequence, we expect that the CPE will perform even better for lattice models than in finite size model considered in this section.

6.5 Application to Physical problems

In this section, we want to further validate the CPE-algorithm, by applying it to some well known physical problems. The focus in this section is not on the actual physics, but rather on the fact that the CPE can be used effectively in a wide range of problems and obtains the results reported in the literature. We will concentrate on two fundamentally different problems. First, we will use the CPE to investigate the momentum dependence of the spectrum. Recently, a lot of attention has gone to the momentum dependent gap formation at half-filling in the single band Hubbard model. By applying the CPE on the \vec{k} -dependent self-energy obtained from the DCA, we would like to verify this phenomenon. Second, we would like to showcase the capabilities of the CPE by computing the spectrum of NiO and comparing the latter to experimental data. The prediction of a 4.3 eV gap around

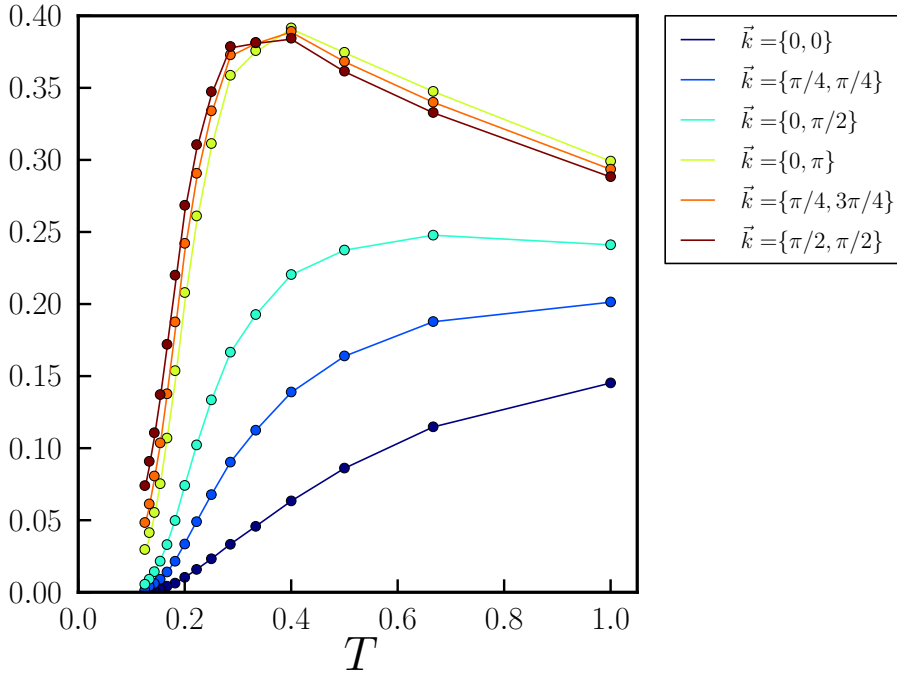


Figure 6.3: . Verification of the CPE algorithm through Eq. (6.24) at zero percent doping. The left hand side $\beta G(\vec{k}, \beta/2)$ is depicted by a solid line, while the right hand side is given by the solid dots. Given that this relationship is not enforced during the minimization-process, the agreement is remarkably good.

the Fermi-energy, absent in LDA-calculations, is one of the great successes of the DMFT. Consequently, it is imperative that the CPE can reproduce this result accurately.

All in all, we want to illustrate that the CPE, in combination with LDA+DMFT, can be a straightforward, easy-to-use numerical tool to determine accurately the spectrum of lattice models as well as real materials.

6.5.1 Momentum-dependent gap formation in half-filled 2D Hubbard model.

The combination of the Dynamical Cluster Approximation together with the CPE algorithm allows us to investigate the momentum dependency of the spectrum in different regimes of the phase-diagram. Recently, a lot of attention has gone to the momentum dependent gap formation at half-filling in the single band Hubbard model. In particular, it has been shown[102, 28]

6. CONTINUOUS-POLE-EXPANSION: A NOVEL METHOD TO OBTAIN THE SPECTRUM OF ELECTRONIC LATTICE MODELS.

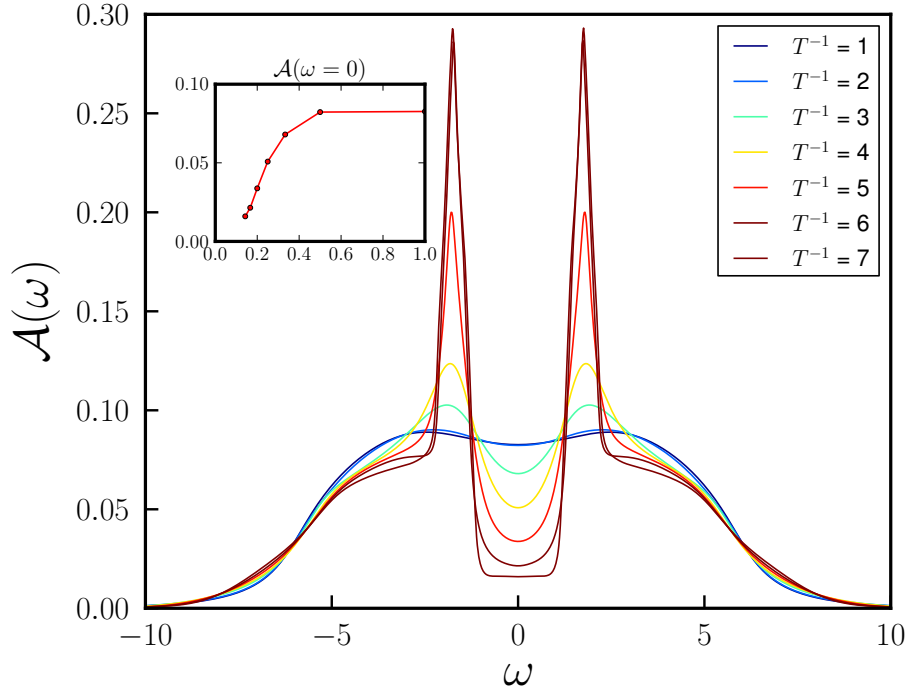


Figure 6.4: Temperature dependence of the spectrum \mathcal{A} at half-filling. Notice the appearance of the van-Hove singularities originating from the band splitting at the Fermi-energy $\omega = 0$.

that for a specific interaction-strength of $U/t = 6$, the anti-nodal regions ($[\pm\pi, 0]$ and $[0, \pm\pi]$) lose their spectral weight contribution at the Fermi-energy faster than the nodal regions ($[\pm\pi/2, \pm\pi/2]$). This momentum anisotropy in the self-energy is a very interesting phenomenon since exotic ground-states such as the anti-ferromagnetic and d-wave superconducting state require a momentum dependent self-energy.

In this paper, we would like to investigate this momentum anisotropy on 32-site cluster at half filling for an interaction strength of $U/t = 6$. A 32-site cluster is large enough to investigate carefully the momentum-anisotropy along the Fermi-surface, and will therefore give us an intimate view on the gap-formation at zero doping. In the literature, the momentum anisotropy of the gap formation has been investigated by using the identity,

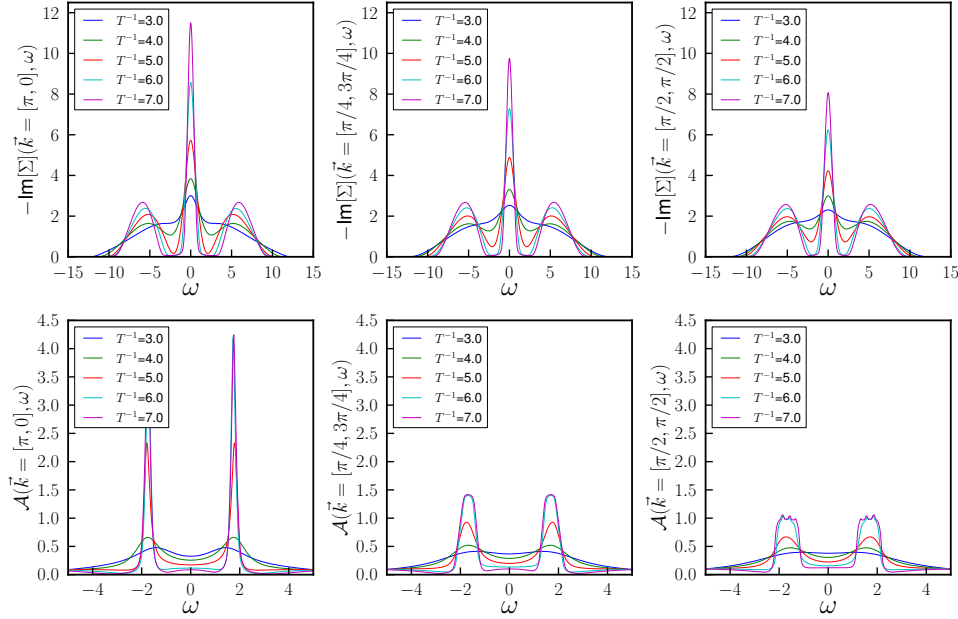


Figure 6.5: Temperature and momentum space dependence of the gap formation at half filling along the Fermi-surface

$$\beta G(\vec{k}, \tau = \beta/2) = -\beta/2 \int d\omega \frac{\mathcal{A}(\vec{k}, \omega)}{\cosh(\beta\omega/2)} \quad (6.24)$$

$$\stackrel{\beta \rightarrow \infty}{\approx} \mathcal{A}(\vec{k}, \omega = 0).$$

At low temperatures, the quantity $\beta G(\vec{k}, \tau = \beta/2)$ is a good estimate for the spectrum at the Fermi-energy, since the function $1/\cosh(\beta\omega/2)$ becomes a delta-function for β going to infinity. Since the imaginary time function can be computed directly with a QMC solver, the spectrum at the Fermi-energy can be probed straightforwardly, without having to do an analytical continuation of the self-energy or Greens-function. With the CPE, we can obtain the spectrum $\mathcal{A}(\vec{k}, \omega)$ on the entire real axis. As a consequence, we can verify the accuracy of the CPE, by performing the integral on the right-hand side of Eq. (6.24) and comparing it to the quantity $\beta G(\vec{k}, \tau = \beta/2)$. In Fig. 6.3, we show for various \vec{k} -points the left hand side of Eq. (6.24) (solid lines) and compare it with the right hand side (solid dots). Given that this relationship is not enforced during the minimization-process, the agreement is remarkably good. This finding implies that all qualitative features we can

deduce from the CPE-algorithm (at the Fermi-energy) would be identical to the results in the literature, deduced from the quantity $\beta G(\vec{k}, \beta/2)$.

The Mott-transition at zero percent doping has been intensively investigated, since the introduction of the DMFT. The behavior of the spectrum as a function of the temperature is therefore well known in this region and offers us a perfect platform to further benchmark the CPE algorithm. In Fig. 6.4, we show the temperature dependence of the spectrum $\mathcal{A}(\omega)$. As is expected, the spectrum drops quickly in a broad region around the Fermi-energy ($\omega = 0$) in order to form a gap. At the same time, two broad Hubbard bands emerge at $\omega = \pm 4$ and two sharp peaks emerge at the edge of the gap. These sharp features originate from the van-Hove singularities, which typically go together with the formation of a gap. The major advantage of analytically continuing the self-energy, opposed to the Greens-function becomes now clear. Since the CPE can only reproduce broad features, it is much better to analytically continue the self-energy. The sharper features such as the van-Hove singularities will then be generated by the Brillouin-zone integration of the Greens function on the real axis,

$$\mathcal{A}(\omega) = -\frac{1}{\pi} \int d\vec{k} \operatorname{Im} \left[\frac{1}{\omega + i\delta + \mu - \varepsilon(\vec{k}) - \Sigma(\vec{k}, \omega)} \right] \quad (6.25)$$

Here, we used a common used off-set of $\delta = 0.1$. The Brillouin zone integration is performed using the tetrahedron integration method[53, 54] (TIM). The TIM was developed especially to deal with integrals over inverse functions. The inversion introduces poles in the integrand, and TIM can treat these poles in a numerically controlled way.

Let us now focus on the momentum anisotropy of the self-energy, and its impact on the spectrum. In Fig. 6.5, we show the imaginary part of the self-energy and the spectrum for three different \vec{k} -points along the Fermi-surface. By looking at the rate of divergence on the imaginary axis of the self-energy and investigating the local densities, Werner et al. [102] argued that the spectrum at the Fermi-energy on the anti-nodal points should disappear at a much faster rate than at the nodal points. The CPE confirms these findings. The imaginary part of the self-energy at the anti-nodal points is much larger than at the nodal points. Since the spectrum is inversely proportional to the self-energy, the spectrum vanishes faster at the anti-nodal points. Furthermore, we can immediately observe that this anisotropy in the self-energy increases as the temperature T is lowered. Using the partial occupancies $n_{\vec{k}}$ in the different patches of the Brillouin zone, Gull et al. [28] have claimed that the gap opened at the nodal region should be much bigger than at the anti-nodal region. If we define the width of the gap as the

minimum distance between the two van Hove singularities in Fig.[6.5], the claim of the anisotropic gap can also be confirmed.

We now concentrate on the features which have not yet been discussed in the literature. In particular, we would like to draw the attention to the formation of the valleys in the imaginary part of the self-energy at $\omega \approx \pm 2$. Going from $T^{-1}=3$ to $T^{-1}=7$, we can observe that these valleys grow faster and are more profound at the anti-nodal points than at the nodal points. Since the imaginary part of the self-energy can be thought of as the inverse lifetime of the quasiparticle, we can conclude that the quasiparticle will have a short lifetime on the Fermi-energy, and a much longer one in the valleys. This picture translates directly into the spectrum, where we see two peaks rapidly grow at $\omega \approx \pm 2$. The difference in the shape of these peaks can be explained by the topology of the free dispersion $\varepsilon(\vec{k})$. The free dispersion is extremely flat at the anti-nodal points, since both the first derivative and the laplacian vanishes at this point). The spectral weight at the nodal point will thus be extremely peaked at the Fermi-energy if no interaction is present. However, if there is a non-zero interaction, the lifetime of the particles at the Fermi-energy will be very short, and all of them will be scattered in equal amount to higher or lower energy-levels. At the nodal points, the free dispersion spectrum is essentially linear with Fermi-velocity vector $\varepsilon(\vec{k}) \sim \vec{k} \vec{v}_F$). Hence, the free spectrum will be smeared around the Fermi-energy and have some spectral weight in the valleys of the the imaginary part of the self-energy. Hence, these electrons will not be scattered away, when an interaction is introduced into the system. With this simple picture in mind, one can now easily understand shape-difference of the peaks in the spectrum shown in Fig. [6.5], as well as the findings of Gull et al. with the partial occupancies as a function of the chemical potential.

6.5.2 Band-structure of NiO

We will now present how the CPE can be successfully used to investigate the spectral properties of real materials, as opposed to electronic lattice models. We have chosen to look at the NiO compound. This prototypical strongly correlated material has been extensively studied, both experimentally [65, 86, 90] as well as theoretically [96, 80, 49, 50]. The experimental results from the literature are the next best thing compared to the exact solution of the impurity model. As such, the NiO is an ideal testing ground for LDA + DMFT calculations [47, 42] with the subsequent CPE analytic continuation of the self-energy to obtain the spectrum of the compound.

The large insulating band gap of 4.3 eV can not be predicted by conventional band theory. More precisely, LDA wrongly predicts the NiO compound to be metallic. The inclusion of spin polarization in density functional theory, such as in LSDA[96], does introduce a band gap as a consequence of the anti-

ferromagnetic order. However, angle-resolved photoemission experiments (ARPES) have shown [97] that the electronic band gap also exists in the paramagnetic phase, far above the Neel temperature at 525K. As the predicted band gap in LSDA is also considerably smaller than the experimental values, the need to include dynamical correlation effects via DMFT is generally accepted. In this work, we will compare our calculated LDA + DMFT + CPE electronic spectra with experimental spectroscopy measurements in order to further validate the CPE method.

Since the exact value of the double counting correction in NiO is still under heavy debate and the goal of this paper is to showcase the capabilities of the CPE algorithm, we will follow the standard procedure reported in the literature by Karolak et al. [42]. As such, we will give a brief, detailed description how the self-energy on the Matsubara frequencies was obtained for this material, but refrain from going into the details surrounding the double counting correction. The non-correlated band structure of NiO was obtained by an LDA calculation and is displayed in the inset of Fig. 6.6. The resemblance of the band-structure reported by Karolak et al. is perfect and we can clearly observe the five Nickel-bands around the Fermi-energy $\omega = 0$ as well as the lower three Oxygen-bands around $\omega \approx -6$. The interaction tensor $U_{v,\sigma,\mu,\sigma'}$ was obtained through a constrained RPA calculation (c-RPA) [48]. As is usual in the NiO compound, we have only kept the interaction-terms between the Nickel-orbitals and ignore the density-density interaction between the Oxygen-Oxygen and Oxygen-Nickel orbitals. In the c-RPA method, the Wannier-orbitals, which are used to construct the tight-binding Hamiltonian \mathcal{H}_{LDA} of the impurity, are reused to construct the interaction tensor $U_{v,\sigma,\mu,\sigma'}$. As a consequence, the interaction terms are more consistent with the band-structure than a simple application of the rotationally invariant Slater-Kanamori [41, 92] on-site interaction-matrix, which is traditionally constructed with the help of the parameters U and J . However, a least squares fit of the the c-RPA matrix towards the parameters U and J reveals that the interaction-matrix can be approximated quite well with the parameters $U = 9.14$ and $J = 0.71$. These values do not differ tremendously from the original $U = 8$ and $J = 1$ parameters by Karolak. For the sake of completeness, we have listed the interaction tensor $U_{v,\sigma,\mu,\sigma'}$ in table 6.1.

The multi-band impurity problem in the self-consistent DMFT-loop was solved by an implementation of the CT-HYB algorithm [101, 103]. As is common in the literature[50], only the diagonal elements of the self-energy matrix are computed with the CT-HYB algorithm and the off-diagonal elements are ignored. Our calculations where performed at an inverse temperature of $\beta = 5 \text{ eV}^{-1}$. At this temperature, the material is in the paramagnetic state and the correlations are strong enough to introduce a band-gap. To account for correlation effects already included in the Hartree and exchange-

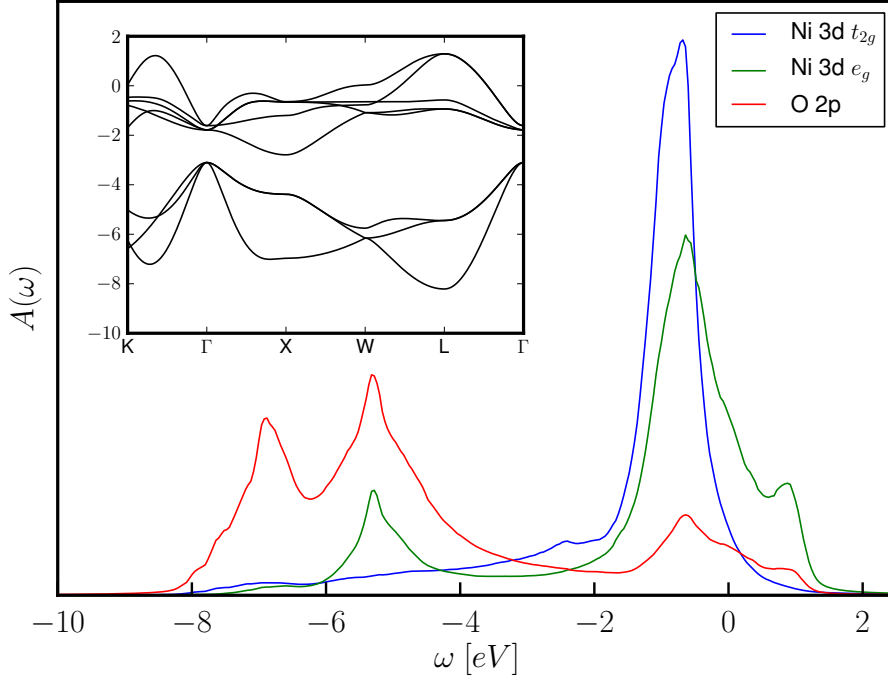


Figure 6.6: The non-correlated partial density of states of NiO as obtained by LDA. Inset: band-structure of NiO obtained with LDA.

correlation terms of the LDA calculation, we include the double-counting term \mathcal{H}_{dc} in our impurity-Hamiltonian \mathcal{H} , given in Eq. 6.26. It should be noted that the sum over the m in the double-counting term \mathcal{H}_{dc} only runs over the Nickel orbitals.

$$\mathcal{H} = \mathcal{H}_{\text{LDA}} - \underbrace{\mu_{\text{dc}} \sum_{m\sigma} n_{m\sigma}}_{\mathcal{H}_{\text{dc}}} + \frac{1}{2} \underbrace{\sum_{v,\sigma,\mu,\sigma'} U_{v,\sigma,\mu,\sigma'} n_{v,\sigma} n_{\mu,\sigma'}}_{\mathcal{H}_{\text{int}}}. \quad (6.26)$$

As pointed out by Karolak, the exact value of the double counting value μ_{dc} is not known. Furthermore, it was shown that the size of Mott-insulator gap increases by decreasing the double counting correction. As such, the double counting correction μ_{dc} can be tuned, such that the computed spectrum has a band-gap which is in accordance with the measured band-gap of 4.3eV. The most optimal value for the double counting correction was found to be 25 eV. For this reason, we use a double counting correction for the Ni-orbitals of 25 eV.

6. CONTINUOUS-POLE-EXPANSION: A NOVEL METHOD TO OBTAIN THE SPECTRUM OF ELECTRONIC LATTICE MODELS.

$U_{\nu,\sigma,\mu,-\sigma}$	$n_{t_{2g,-\sigma}}$	$n_{t_{2g,-\sigma}}$	$n_{e_g,-\sigma}$	$n_{t_{2g,-\sigma}}$	$n_{e_g,-\sigma}$
$n_{t_{2g,\sigma}}$	9.14	7.60	7.37	7.60	8.28
$n_{t_{2g,\sigma}}$	7.60	9.14	8.06	7.60	7.60
$n_{e_g,\sigma}$	7.37	8.06	9.14	8.06	7.37
$n_{t_{2g,\sigma}}$	7.60	7.60	8.06	9.14	7.60
$n_{e_g,\sigma}$	8.28	7.60	7.37	7.60	9.14

$U_{\nu,\sigma,\mu,\sigma}$	$n_{t_{2g,\sigma}}$	$n_{t_{2g,\sigma}}$	$n_{e_g,\sigma}$	$n_{t_{2g,\sigma}}$	$n_{e_g,\sigma}$
$n_{t_{2g,\sigma}}$	0.00	6.83	6.49	6.83	7.85
$n_{t_{2g,\sigma}}$	6.83	0.00	7.51	6.83	6.83
$n_{e_g,\sigma}$	6.49	7.51	0.00	7.51	6.49
$n_{t_{2g,\sigma}}$	6.83	6.83	7.51	0.00	6.83
$n_{e_g,\sigma}$	7.85	6.83	6.49	6.83	0.00

Table 6.1: The interaction tensor $U_{\nu,\sigma,\mu,\sigma'}$ for NiO obtained by c-RPA. The tensor can be approximated by the rotationally invariant Slater-Kanamori interaction-matrix, using $U = 9.14$ and $J = 0.71$, which are close to the commonly accepted values of $U = 8$ and $J = 1$ in the literature.

Once a density-density interaction is included between the Nickel-orbitals by means of a self-consistent DMFT calculation, a band gap appears in the spectral density. This can be clearly seen in Fig. 6.7, where the partial spectra of each orbital are displayed. As usual, Fig. 6.7 was obtained by performing an analytical continuation of the Matsubara self-energy to the real axis with an off-set of $\delta = 0.1$. A consecutive tetrahedron integration over the entire Brillouin zone then results in the lattice Greens-function, from which the partial spectra $A_\nu(\omega)$ can be trivially obtained. If we use the same definition of the band-gap from experimental physics, i.e. the distance between the mid-points of the top of the peaks, we obtain a band-gap of 4.55 eV, in good agreement with the experimental value of 4.3 eV obtained by Sawatzky and Allen [86]. These mid-points are represented by the horizontal dotted lines in Fig. 6.7. Their intersection with the peak is marked by the vertical dotted lines, which difference defines the band-gap.

From the comparison between the ED-results and CPE, we know that the CPE is very good at reproducing an accurate picture for the spectrum close to the Fermi-energy. As such, it is not surprising to reproduce the correct band-gap of NiO around the Fermi-energy. To further bench-mark the CPE, we will compare the calculated spectrum with the experimental spectrum obtained by Sawatzky and Allen [86]. In this way, we want to explore

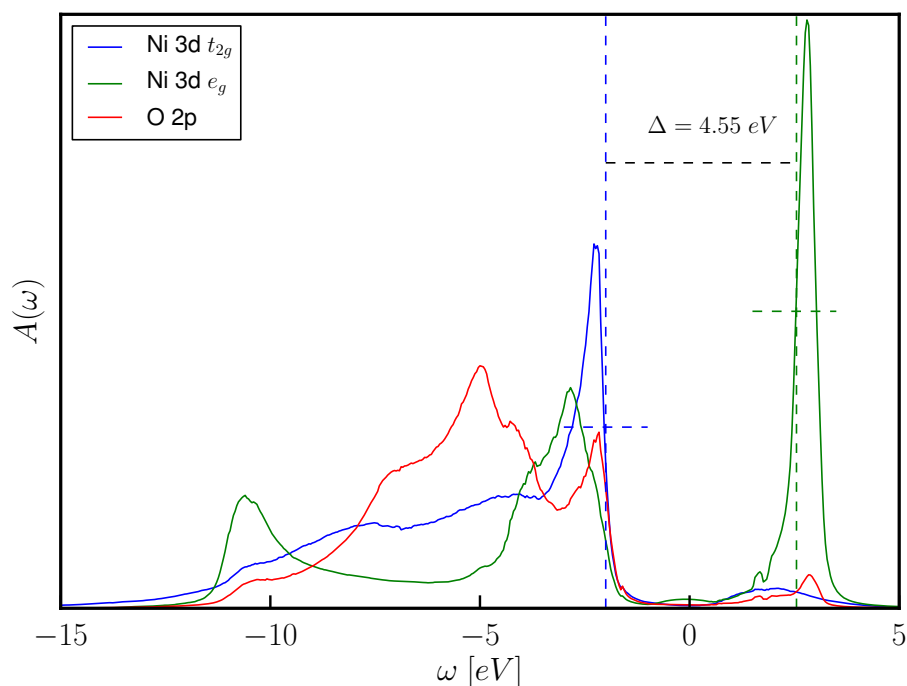


Figure 6.7: The correlated partial spectra of NiO calculated by LDA + DMFT + CPE. Defining the band-gap as in experimental physics, i.e. the distance between the mid-points of the top of the peaks, we obtain a band-gap of 4.55 eV, in good agreement with the experimental value of 4.3 eV.

how the CPE behaves over the entire real-axis and whether it can capture the essential physics far from the Fermi-energy, as we claimed in the Exact Diagonalization section. The experimental spectrum was obtained as a combination of X-ray photoemission (XPS) and Bremsstrahlung-Isocromat-Spectroscopy (BIS) measurements on cleaved single crystals of NiO. The XPS spectrum was recorded at 120 eV and mainly captures the Nickel 3d character. The measured spectra is shown in Fig. 6.8, together with the LDA + DMFT + CPE spectrum. The latter is obtained by summing up the partial spectra depicted in Fig. 6.7 and multiplied with the multiplicity of each orbital ($3 \times t_{2g}, 2 \times e_g, 3 \times O_{2p}$). Since the spectroscopy is measured in arbitrary units of intensity, we can scale the measured spectrum such that the largest peaks have the same height. A simple comparison of both spectra shows a very good agreement between measured and computed spectrum. In the region $[-15, -5]$, we can observe that the CPE gradually rises and appears to reproduce some of the peaks, albeit with a slight left-shift of approximately 2 eV. The peaks that define the gap around the Fermi-surface are also much sharper defined with the CPE. Most likely, this originates

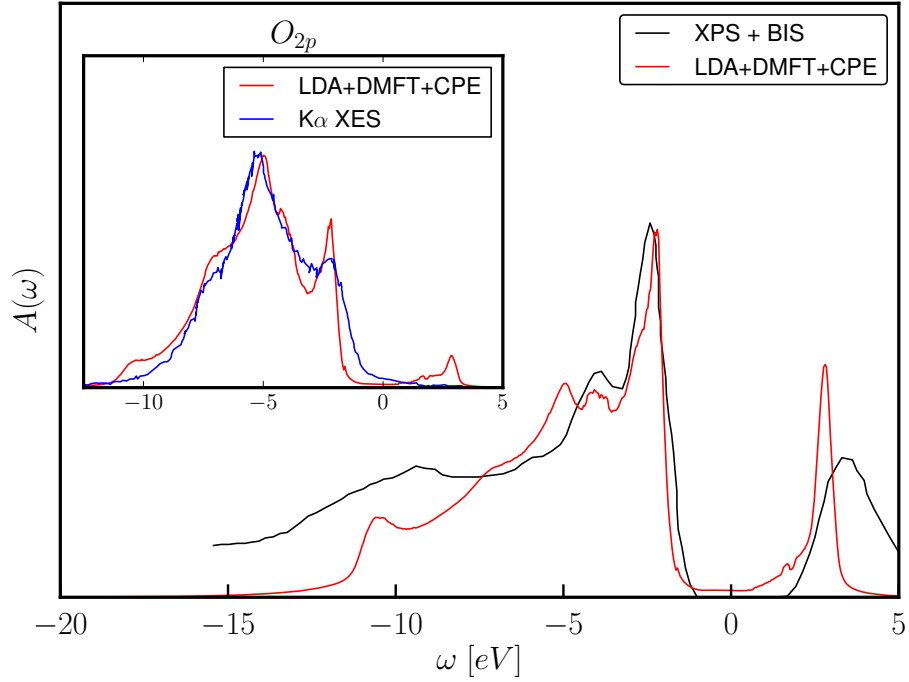


Figure 6.8: The comparison of XPS and BIS spectra[86] to the spectral function of NiO calculated by LDA + DMFT + CPE. The XPS spectrum is measured at 120 eV, showing primarily the Nickel 3d character. Inset: The comparison of $K\alpha$ -emission spectra[51] with the partial spectrum of the O_{2p} orbital calculated by LDA + DMFT + CPE.

from the TIM integration of the self-energy.

To further validate the CPE, we compare the partial spectrum of the O_{2p} orbitals. The latter was measured very accurately by Kurmaev et al.[51] with X-ray emission spectroscopy (XES). The Oxygen K-edge emission spectrum provides a representation of the O_{2p} spectrum, and can thus be readily used to compare with the calculated O_{2p} spectrum. In the inset of Fig. 6.8, we compare the measured with the computed partial spectrum. Just as with the total spectrum, we can observe a very good match between theory and experiment and much sharper peaks and valleys in the CPE. The figure also shows that the CPE can describe the essential physics far away from the Fermi-surface rather well, as claimed in the ED section. This is not surprising, since the CPE produces a smooth self-energy on the real-axis, which is consistent with the basic assumption of a mean field theory such as the DMFT.

6.6 Conclusions

We have presented a new algorithm, the continuous pole expansion, that allows us to probe the self-energy on the real axis through an analytical continuation of its values located on the Matsubara frequencies. As a consequence, we can compute the Greens-function on the real axis and thus obtain the spectrum of the interacting lattice-model, associated to the self-energy located on the Matsubara frequencies. The need for this algorithm arises from the development of a new class of impurity solvers, namely the continuous time Quantum Monte Carlo solvers. Together with the NFFT method, these new solvers can directly accumulate the Greens-function and self-energy on the Matsubara frequencies and by-pass therefore the less accurate accumulation in imaginary time and consecutive Fourier-transform to the Matsubara frequencies.

Since the analytical continuation of a complex function is notoriously unstable, we have developed the CPE algorithm starting from the well-known analytical properties of the self-energy. Two of these analytical properties are of particular use with regard to the CPE. First of all, there is a branch cut along the real-axis in the imaginary part of the self-energy. Moreover, when the branch-cut is approached from the upper complex plane, the self-energy is negative definite, i.e. $\lim_{\omega \rightarrow 0} \text{Im}[\Sigma(\vec{k}, \omega + i\varphi)] \leq 0$. As a consequence, we must parametrize the imaginary part of the self-energy as a purely negative function, which is a very strong constrain. Second, we know that the self-energy is an analytical function, which effectively means that it has no poles in the upper complex plane. This implies that we can use the Kramers-Kronig relationship to compute the self-energy anywhere in the complex plane, given its imaginary part on the real axis. Consequently, we can compute the self-energy on the Matsubara frequencies for any given parametrization of the imaginary part on the real axis. With these two analytical properties in mind, the CPE can now be summarized in one sentence: Find a negative definite parametrization of the imaginary part of the self-energy on the real axis such that the norm between the accumulated QMC self-energy and the computed self-energy on the Matsubara frequencies is minimized.

By taking advantage of the analytical properties of the self-energy, we have rewritten the analytical continuation problem into a constrained minimization problem. This has two advantages. A minimization problem is numerically more stable, especially with regard to statistical noise, which arises from the Monte Carlo procedure. Secondly, the constrained minimization problem can be rewritten to a quadratic programmable optimization problem, with linear constraints. These type of problems are well known and many algorithms exist to solve this particular type of problem. In this paper, we have used the simplest one: the Frank-Wolf algorithm.

6. CONTINUOUS-POLE-EXPANSION: A NOVEL METHOD TO OBTAIN THE SPECTRUM OF ELECTRONIC LATTICE MODELS.

The validation of the CPE algorithm has received special attention in this paper. In essence, we have approached the validation issue in two ways. First, we have looked at the exactly solvable models. By comparing the self-energy and spectrum of the CPE with the exact result of an 8-site, isolated cluster, we could investigate the strengths and weaknesses of the CPE. It became clear the CPE captures features close to the Fermi-energy very well, as well as broad features far from the Fermi-energy. It is however unable to capture any sharp features on the real-axis. Consequently, we obtain a much smoother spectrum with the CPE far from the Fermi-energy than in the exact result, while maintaining the correct spectrum around the Fermi-energy. Next, we wanted to show that the CPE produces the correct result for some well-known problems in the literature. The recent debate around the momentum-dependent gap formation in half-filled 2D Hubbard model is an ideal test-case. Since their findings are based on the identity in Eq. (6.24), we have validated this identity with the CPE over a wide range of temperatures and can thus conclude that the CPE confirms their findings and is in line with what is now commonly accepted in the literature. Furthermore, we could also observe from the k-dependent spectrum that the gap is indeed smaller at the nodal point than at the anti-nodal. Last but not least, we have also used the CPE in order to determine the spectrum of *NiO*. This strongly correlated material has been extensively studied, both experimentally as theoretically. Following the standard route in order to obtain the self-energy on the Matsubara frequencies, this material is an ideal testing ground for CPE calculations, since we can directly compare the CPE produced spectrum with XPS, XES and BIS measurements. The agreement between measurement and the CPE-spectrum in Fig. 6.8 is very satisfying and show-cases how the CPE might be used in the future in order to determine the spectra of other less well known strongly correlated materials.

Chapter 7

Press Releases

7.1 ORNL

A team of researchers simulating high-temperature superconductors has topped 15 petaflops or 15 thousand trillion calculations a second on Oak Ridge National Laboratory's (ORNL's) Titan supercomputer. More importantly, they did it with an algorithm that substantially overcomes two major roadblocks to realistic superconductor modeling.

For their achievement, the team from ETH Zurich in Switzerland and ORNL was named a finalist for the Gordon Bell Prize, awarded each year for outstanding achievement in high-performance computing.

Materials become superconducting when electrons within them form pairs called Cooper pairs allowing them to collect into a condensate. As a result, superconducting materials conduct electricity without resistance, and therefore without loss. This makes them immensely promising in energy applications such as power transmission. They are also especially powerful magnets, a property exploited in technologies such as maglev trains and MRI scanners.

The problem with these materials is that they are superconducting only when they are very, very cold. For instance, the earliest discovered superconductor, mercury, had a transition temperature of 4.2 Kelvin, which is below -450 degrees Fahrenheit and very close to absolute zero. Mercury and other early superconductors were cooled with liquid helium a very expensive process. Later materials remained superconducting above liquid nitrogen's boiling point of -321 degrees Fahrenheit, making their use less expensive.

The discovery, or creation, of superconductors that needn't be cooled would revolutionize power transmission and the energy economy.

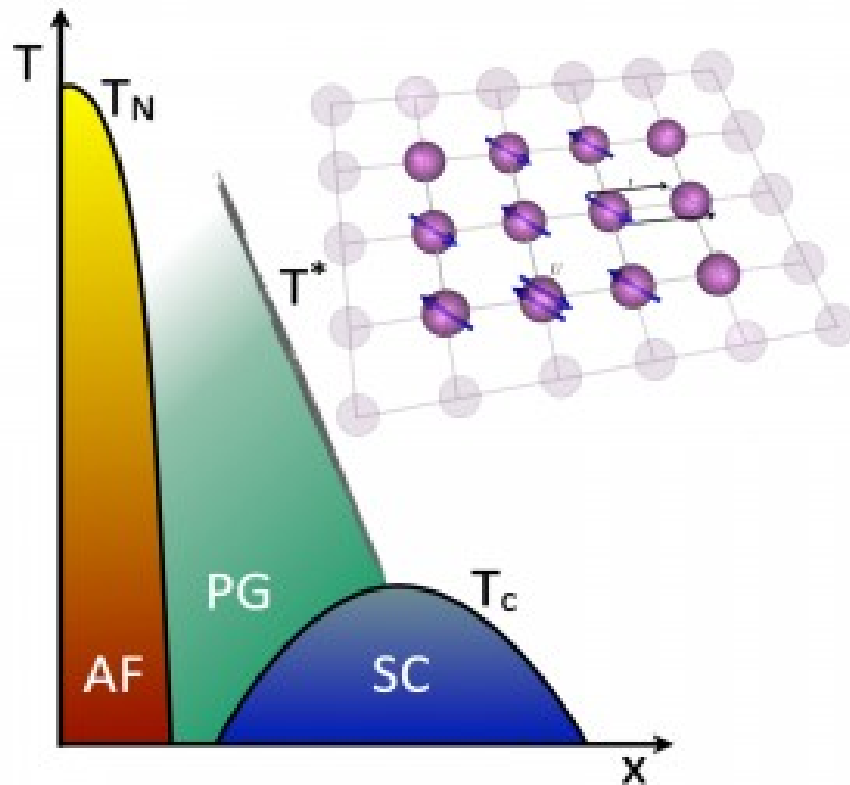


Figure 7.1: Generic temperature (T) vs. doping (x) phase diagram of the cuprates with antiferromagnetic (AF), superconducting (SC) and pseudogap (PG) phases. The inset on the top right shows an embedded Hubbard cluster representing a DCA calculation of a Hubbard model on a square lattice with nearest neighbor hopping t and local Coulomb repulsion U .

The Swiss and American team approaches the problem with an application called DCA++, with DCA standing for dynamical cluster approximation. DCA++ simulates a cluster of atoms using the Hubbard model which describes the behavior of electrons in a solid. It does so with a quantum Monte Carlo technique, which involves repeated random sampling.

The application earned its development team the Gordon Bell Prize in 2008.

The new method, known as DCA+, was developed largely by Peter Staar at ETH Zurich. It scaled to the full 18,688-node Titan system and took full advantage of the system's NVIDIA GPUs, reaching 15.4 petaflops.

In addition, it takes full advantage of the energy efficiency inherent in Titans hybrid architecture. Each node of Titan contains both a CPU and a GPU. Using this system, simulation of the teams largest realistic clusters consumed 4,300 kilowatt-hours. The same simulation on a comparable CPU-only system, the Cray XE6, would have consumed nearly eight times as much energy, or 33,580 kilowatt-hours.

The DCA+ algorithm also took a bite out of two nagging problems common to dynamic cluster quantum Monte Carlo simulations. These are known as the fermionic sign problem and the cluster shape dependency.

The sign problem is a major complication in the quantum physics of many-particle systems when they are modeled with the Monte Carlo method.

Particles in quantum mechanics are described by a wave function. For electrons and other fermions, this function switches from positive to negative or vice versa when two particles are interchanged. If you then sum the many-particle states, the positive and negative values nearly cancel one another out, essentially destroying the accuracy of the simulation.

This is a cluster method, said team member Thomas Maier of ORNL. If you could make the cluster size infinite, then you would get the exact solution. So the goal is to make it as large as possible.

But theres a problem when you deal with electrons, which are fermions. Its the infamous fermion sign problem, and it really limits the cluster size we can go to and the lowest temperature we can go to with quantum Monte Carlo.

The sign problem cannot be overcome simply by creating larger supercomputers, Maier noted, because computational demands grow exponentially with the number of atoms being simulated. In other words, as you go to realistically large systems, you get problems that overwhelm not only every existing supercomputer, but any system were likely to see in the foreseeable future.

According to team member Thomas Schulthess of ETH Zurich and ORNL, the DCA+ algorithm arrives at a solution nearly 2 billion times faster than its DCA predecessor. So while it doesnt make the sign problem go away entirely, it does make room for much more useful simulations, specifically by allowing for more atoms at lower temperatures a key requirement, since so far superconductivity happens only in very cold environments.

The other problem cluster shape dependency meant that when the researchers simulated an atom cluster, the answer they got varied widely depending on the shape of the cluster.

Lets say you have two 16-site clusters, Maier explained, one two-dimensional system with a four-by-four cluster and another 16-site cluster of a different

shape. The results with the standard DCA method depended a lot on the cluster shape. That's of course something you don't really want.

By improving the algorithm we succeeded in getting rid of this cluster shape dependence. Before you would get vastly different results for the superconducting transition temperature, but now you get pretty much the same.

The reduced sign problem, combined with the power of Titan, also allows the group to simulate much larger systems. In the past, the group was limited to eight-atom cluster simulations if it wanted to get down to the transition temperature for realistic parameters. More recently it has been able to scale up to 28-atom systems.

As the team moves forward, Maier noted, it would like to simulate more complex and realistic systems. For instance, two of the most promising materials in high-temperature superconducting research, which contain copper and iron, hold their electrons in a number of different orbitals. Yet, so far the team has simulated only one of these orbitals.

One direction we want to go into is to make the models more realistic by including more degrees of freedom, or orbitals. But before you do that you want to have a method that allows you to get an accurate answer for the simple model. Then you can move on to more complicated models.

The question is always, Do you get to the interesting region where you get interesting physics before you hit the sign problem, Maier noted. We were able to get there to some extent before we had this new method. But now we really have a significant improvement. Now we can really look at realistic parameters.

The Gordon Bell Prize will be presented November 21 during the SC13 supercomputing conference in Denver. Besides Staar, Maier, and Schulthess, the DCA+ team includes Raffaele Solca and Gilles Fourestey of ETH Zurich and Michael Summers of ORNL.

7.2 CSCS press release

November 18, 2013 - by Simone Ulmer

Quantum leap in superconductor simulation Researchers from ETH Zurich have developed an algorithm that simulates high-temperature superconductivity much faster. The team was nominated as one of the Gordon Bell Prize finalists for the project and is to be rewarded by the US Department of Energy with access to the supercomputer Titan.

Despite three decades of intensive science, the origin of the superconducting transition in the 2D copper-oxygen planes of the high T_c superconductors

(here $\text{YBa}_2\text{Cu}_3\text{O}_{6+x}$) is still a mystery. The aim of DCA+ is to improve our understanding of the superconductive state in these materials by simulating electrons on a square lattice that can hop from an occupied (red) to an unoccupied (blue) state and interact with an on-site interaction (red cloud). With the new code, the scientists can detect the temperature at which the system undergoes a superconducting transition with unprecedented accuracy and hope to understand the phase diagram better. Peter Staar, a doctoral student under Thomas Schulthess at ETH Zurich, refined an algorithm for the simulation of solid bodies like superconductors during his doctorate. Thanks to the algorithm, the researchers reach their goal considerably more rapidly than before – in some cases even up to a billion times faster, say the scientists. Using the algorithm on the supercomputer Titan at Oak Ridge National Laboratory, they managed to carry out 15,000 trillion computational operations per second – fifteen petaflops. However, not only does the new algorithm work faster; the scientists have also used it to overcome two central problems in the simulation of high-temperature superconductors. Moreover, the new calculations reveal that the simplest models do not rule out superconductivity at room temperature.

Conducting electricity without resistance

The researchers themselves dub their publication, for which they were nominated for the coveted Gordon Bell Prize, a quantum leap in the so-called time-to-solution simulation of high-temperature superconductor models. The US Department of Energy honored the teams achievement with its INCITE Award: the scientists are to receive 2 million dollars worth of computing time on the supercomputer Titan in 2014 and will also have the opportunity to have this awarded for 2015 and 2016.

Superconductors and probably also the little-understood high-temperature superconductors are composed of materials, in the crystal lattice of which electrons arrange themselves in pairs, so-called Cooper pairs, at extremely low temperatures – at least -234 Celsius or -140 Celsius for high-temperature superconductors. A phase transition then occurs in the system, where the electrical resistance of the material becomes zero and electricity can flow without any loss of energy.

Until now, such phase transitions were simulated approximately with the algorithm DCA (Dynamical Cluster Approximation). In doing so, only a small section of the crystal lattice, a cluster of atoms, was simulated on account of the complexity of the quantum system to be modeled and the associated computational intensity of the interacting particles. Qualitatively speaking, this works very well with the previous methods, says Staar. Ascertaining the exact so-called transition temperature at which a phase transition takes place quantitatively, however, was not possible until now. The central problem of DCA is that the critical temperature depends greatly on the size of

the cluster and its geometry. This doesn't allow us to determine a uniform and precise transition temperature.

More convincing simulations

Through Peter Staar's revision and extension of DCA to form the new algorithm DCA+, the clusters are basically calculated continuously as opposed to in steps, which eradicates the geometry problem. The results of the cluster are consistent, even if the geometry has been altered through a rotation in the crystal lattice, for instance. The new procedure has also made another breakthrough with the so-called fermionic sign problem, which arises when simulating quantum systems with the so-called Monte Carlo Method. With this technique, it is not possible to determine the transition temperature explicitly due to the mathematical and physical conditions.

Although the fermionic sign problem is not solved with DCA+, the effect is delayed, explains Staar. This enables us to reach the point where the transition to superconductivity takes place and determine the transition temperature. For him personally, however, another key aspect of these research results is the fact that the new calculations made with this simple model cannot rule out superconductivity at room temperature. If additional calculations on more complex and material-specific models confirm this, it could revitalize a discussion that has already been going on for decades. In materials science, the further development of superconductors is regarded as a promising field with many potential applications in energy technology and electronics. Scientists have dreamt of superconductivity at room temperature ever since the 1980s, when high-temperature superconductors were first discovered.

Whether Staar has won the Gordon Bell Prize for his work together with colleagues from ETH Zurich and Oak Ridge National Laboratory will be announced on 21 November 2013 at SC13 conference. The six finalists also include a project by ETH-Zurich professor Petros Koumoutsakos and his team, which they conducted in conjunction with IBM Research Zurich and Lawrence Livermore National Laboratory (see ETH News, 15.11.2013).

Titan: The supercomputer Titan has 18,688 computer nodes that generate 17.59 petaflops of computational power. DCA+ was scaled on the entire system, which means that the algorithm is capable of exploiting almost the entire computational capacity. This extraordinary achievement earned the project a nomination for the Gordon Bell Prize and the INCITE Award.

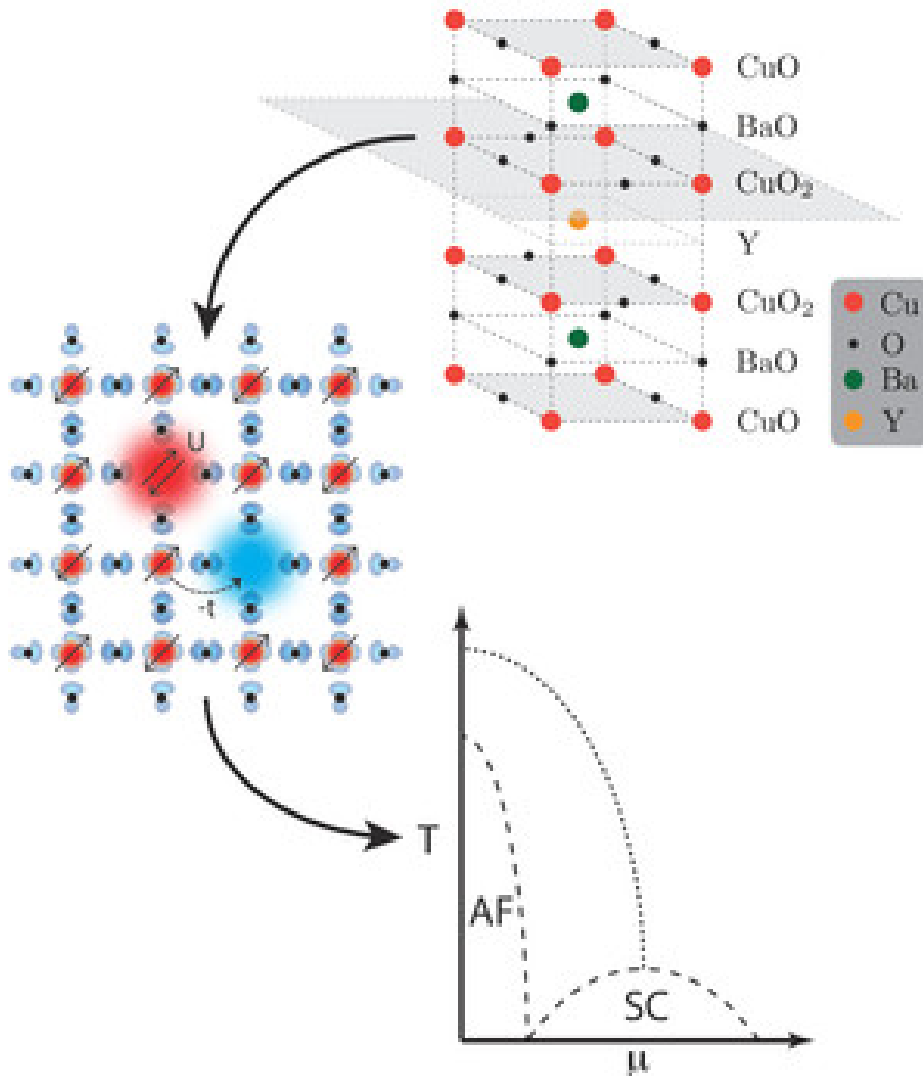


Figure 7.2: Despite three decades of intensive science, the origin of the superconducting transition in the 2D copper-oxygen planes of the high T_c superconductors (here $\text{YBa}_2\text{Cu}_3\text{O}_{6+x}$) is still a mystery. The aim of DCA+ is to improve our understanding of the superconductive state in these materials by simulating electrons on a square lattice that can hop from an occupied (red) to an unoccupied (blue) state and interact with an on-site interaction (red cloud). With the new code, the scientists can detect the temperature at which the system undergoes a superconducting transition with unprecedented accuracy and hope to understand the phase diagram better.

Bibliography

- [1] A. A. Abrikosov, L. P. Gorkov, and I. Y. Dzyaloshinskii. *Quantum field theoretical methods in statistical physics, International series of monographs in natural philosophy*, volume 4. Pergamon Press, Oxford, 1965.
- [2] G. Alvarez, M. S. Summers, D. E. Maxwell, M. Eisenbach, J. S. Meredith, J. M. Larkin, J. Levesque, T. A. Maier, P. R. C. Kent, E. F. D’Azevedo, and T. C. Schulthess. New algorithm to enable 400+ tflop/s sustained performance in simulations of disorder effects in high- T_c superconductors. In *Proceedings of the 2008 ACM/IEEE conference on Supercomputing, SC ’08*, pages 61:1–61:10, Piscataway, NJ, USA, 2008. IEEE Press.
- [3] O. K. Andersen and T. Saha-Dasgupta. Muffin-tin orbitals of arbitrary order. *Phys. Rev. B*, 62:R16219–R16222, Dec 2000.
- [4] O.K. Andersen, A.I. Liechtenstein, O. Jepsen, and F. Paulsen. LDA energy bands, low-energy hamiltonians, t' , t'' , $t_{\perp}(k)$ and j_{\perp} . *Journal of Physics and Chemistry of Solids*, 56(12):1573 – 1591, 1995. Proceedings of the Conference on Spectroscopies in Novel Superconductors.
- [5] V. I. Anisimov, D. E. Kondakov, A. V. Kozhevnikov, I. A. Nekrasov, Z. V. Pchelkina, J. W. Allen, S.-K. Mo, H.-D. Kim, P. Metcalf, S. Suga, A. Sekiyama, G. Keller, I. Leonov, X. Ren, and D. Vollhardt. Full orbital calculation scheme for materials with strongly correlated electrons. *Phys. Rev. B*, 71:125119, Mar 2005.
- [6] V I Anisimov, A I Poteryaev, M A Korotin, A O Anokhin, and G Kotliar. First-principles calculations of the electronic structure and spectra of strongly correlated systems: dynamical mean-field theory. *Journal of Physics: Condensed Matter*, 9(35):7359, 1997.

- [7] F. Aryasetiawan, K. Karlsson, O. Jepsen, and U. Schönberger. Calculations of hubbard u from first-principles. *Phys. Rev. B*, 74:125106, Sep 2006.
- [8] J. Bardeen, L. N. Cooper, and J. R. Schrieffer. Theory of superconductivity. *Phys. Rev.*, 108:1175–1204, Dec 1957.
- [9] Gordon Baym. Self-consistent approximations in many-body systems. *Phys. Rev.*, 127:1391–1401, Aug 1962.
- [10] Gordon Baym and Leo P. Kadanoff. Conservation laws and correlation functions. *Phys. Rev.*, 124:287–299, Oct 1961.
- [11] J.G. Bednorz and K.A. Müller. Possible high c superconductivity in the balacuo system. *Zeitschrift für Physik B Condensed Matter*, 64(2):189–193, 1986.
- [12] John M. Bennett. Triangular factors of modified matrices. *Numerische Mathematik*, 7:217–221, June 1965.
- [13] C. Berthod, T. Giamarchi, S. Biermann, and A. Georges. Breakup of the fermi surface near the mott transition in low-dimensional systems. *Phys. Rev. Lett.*, 97:136401, Sep 2006.
- [14] J.M. Bioucas-Dias, M. A T Figueiredo, and J.P. Oliveira. Total variation-based image deconvolution: a majorization-minimization approach. In *Acoustics, Speech and Signal Processing, 2006. ICASSP 2006 Proceedings. 2006 IEEE International Conference on*, volume 2, pages II–II, 2006.
- [15] R. Blankenbecler, D. J. Scalapino, and R. L. Sugar. Monte carlo calculations of coupled boson-fermion systems. i. *Phys. Rev. D*, 24:2278–2286, Oct 1981.
- [16] Martin D. Buhmann and M. D. Buhmann. *Radial Basis Functions*. Cambridge University Press, New York, NY, USA, 2003.
- [17] N. Bulut, D. J. Scalapino, and S. R. White. Bethe-salpeter eigenvalues and amplitudes for the half-filled two-dimensional hubbard model. *Phys. Rev. B*, 47:14599–14602, Jun 1993.
- [18] A. K. Cline. Scalar- and planar-valued curve fitting using splines under tension. *Commun. ACM*, 17(4):218–220, April 1974.
- [19] C. Deboor. *A Practical Guide to Splines*. Springer-Verlag Berlin and Heidelberg GmbH & Co. K, December 1978.

-
- [20] G. M. Eliashberg. Interactions between electrons and lattice vibrations in a superconductor. *Sov. Phys. JETP*, 11(3):696–702, 1960.
- [21] V. J. Emery and S. A. Kivelson. Importance of phase fluctuations in superconductors with small superfluid density. *Nature*, 374(6521):434–437, 03 1995.
- [22] M. Frank and P. Wolfe. An algorithm for quadratic programming. *Naval Research Logistics Quarterly*, 3(1-2):95–110, March-June 1956.
- [23] Matteo Frigo and Steven G. Johnson. The design and implementation of FFTW3. *Proceedings of the IEEE*, 93(2):216–231, 2005. Special issue on “Program Generation, Optimization, and Platform Adaptation”.
- [24] Jürg Fröhlich and Thomas Spencer. Kosterlitz-thouless transition in the two-dimensional plane rotator and coulomb gas. *Phys. Rev. Lett.*, 46:1006–1009, Apr 1981.
- [25] A. Fuhrmann, S. Okamoto, H. Monien, and A. J. Millis. Fictive-impurity approach to dynamical mean-field theory: A strong-coupling investigation. *Phys. Rev. B*, 75:205118, May 2007.
- [26] Antoine Georges, Gabriel Kotliar, Werner Krauth, and Marcelo J. Rozenberg. Dynamical mean-field theory of strongly correlated fermion systems and the limit of infinite dimensions. *Rev. Mod. Phys.*, 68:13–125, Jan 1996.
- [27] J Gubernatis, Mark Jarrell, R Silver, and D Sivia. Quantum monte carlo simulations and maximum entropy: Dynamics from imaginary-time data. *Physical Review B*, 44(12):6011–6029, September 1991.
- [28] E. Gull, M. Ferrero, O. Parcollet, A. Georges, and A. J. Millis. Momentum-space anisotropy and pseudogaps: A comparative cluster dynamical mean-field analysis of the doping-driven metal-insulator transition in the two-dimensional hubbard model. *Phys. Rev. B*, 82:155101, Oct 2010.
- [29] E. Gull, P. Werner, O. Parcollet, and M. Troyer. Continuous-time auxiliary-field monte carlo for quantum impurity models. *EPL (Europhysics Letters)*, 82(5):57003, 2008.
- [30] Emanuel Gull, Andrew J. Millis, Alexander I. Lichtenstein, Alexey N. Rubtsov, Matthias Troyer, and Philipp Werner. Continuous-time monte carlo methods for quantum impurity models. *Rev. Mod. Phys.*, 83:349–404, May 2011.

- [31] Emanuel Gull, Olivier Parcollet, and Andrew J. Millis. Superconductivity and the pseudogap in the two-dimensional hubbard model. *Phys. Rev. Lett.*, 110:216405, May 2013.
- [32] Emanuel Gull, Olivier Parcollet, Philipp Werner, and Andrew J Millis. Momentum-sector-selective metal-insulator transition in the eight-site dynamical mean-field approximation to the Hubbard model in two dimensions. *Physical Review B*, 80(24):245102, December 2009.
- [33] Emanuel Gull, Peter Staar, Sebastian Fuchs, Phani Nukala, Michael S. Summers, Thomas Pruschke, Thomas C. Schulthess, and Thomas Maier. Submatrix updates for the continuous-time auxiliary-field algorithm. *Phys. Rev. B*, 83:075122, Feb 2011.
- [34] M. H. Hettler, M. Mukherjee, M. Jarrell, and H. R. Krishnamurthy. Dynamical cluster approximation: Nonlocal dynamics of correlated electron systems. *Phys. Rev. B*, 61:12739–12756, May 2000.
- [35] M. H. Hettler, A. N. Tahvildar-Zadeh, M. Jarrell, T. Pruschke, and H. R. Krishnamurthy. Nonlocal dynamical correlations of strongly interacting electron systems. *Phys. Rev. B*, 58:R7475–R7479, Sep 1998.
- [36] J. E. Hirsch and R. M. Fye. Monte carlo method for magnetic impurities in metals. *Phys. Rev. Lett.*, 56:2521–2524, Jun 1986.
- [37] J Hubbard. Electron correlations in narrow energy bands. *Proceedings of the Royal Society A: Mathematical, Physical and Engineering Sciences*, 276(1365):238–257, November 1963.
- [38] P.A. Jansson. *Deconvolution of Images and Spectra: Second Edition*. Dover Books on Engineering Series. Dover Publications, 2011.
- [39] M. Jarrell, Th. Maier, C. Huscroft, and S. Moukouri. Quantum monte carlo algorithm for nonlocal corrections to the dynamical mean-field approximation. *Phys. Rev. B*, 64:195130, Oct 2001.
- [40] Mark Jarrell and James E Gubernatis. Bayesian inference and the analytic continuation of imaginary-time quantum monte carlo data. *Physics Reports*, 269(3):133–195, 1996.
- [41] Junjiro Kanamori. Electron correlation and ferromagnetism of transition metals. *Progress of Theoretical Physics*, 30(3):275–289, 1963.
- [42] M. Karolak, G. Ulm, T. Wehling, V. Mazurenko, A. Poteryaev, and A. Lichtenstein. Double counting in lda+ dmft—the example of nio. *Journal of Electron Spectroscopy and Related Phenomena*, 181(1):11–15, 2010.

-
- [43] Y. Katznelson. *An Introduction to Harmonic Analysis*. Cambridge Mathematical Library. Cambridge University Press, 2004.
- [44] Jens Keiner, Stefan Kunis, and Daniel Potts. Using nfft 3—a software library for various nonequispaced fast fourier transforms. *ACM Trans. Math. Softw.*, 36(4):19:1–19:30, August 2009.
- [45] R Keys. Cubic convolution interpolation for digital image processing. *Acoustics, Speech and Signal Processing, IEEE Transactions on*, 29(6):1153–1160, 1981.
- [46] J M Kosterlitz and D J Thouless. Ordering, metastability and phase transitions in two-dimensional systems. *Journal of Physics C: Solid State Physics*, 6(7):1181, 1973.
- [47] G. Kotliar, S. Y. Savrasov, K. Haule, V. S. Oudovenko, O. Parcollet, and C. A. Marianetti. Electronic structure calculations with dynamical mean-field theory. *Rev. Mod. Phys.*, 78:865–951, Aug 2006.
- [48] Anton Kozhevnikov, Adolfo G. Eguiluz, and Thomas C. Schulthess. Toward first principles electronic structure simulations of excited states and strong correlations in nano- and materials science. In *Proceedings of the 2010 ACM/IEEE International Conference for High Performance Computing, Networking, Storage and Analysis, SC '10*, pages 1–10, Washington, DC, USA, 2010. IEEE Computer Society.
- [49] J. Kuneš, V. I. Anisimov, A. V. Lukoyanov, and D. Vollhardt. Local correlations and hole doping in nio: A dynamical mean-field study. *Phys. Rev. B*, 75:165115, Apr 2007.
- [50] J Kunes, V Anisimov, S Skornyakov, A Lukoyanov, and D Vollhardt. NiO: Correlated Band Structure of a Charge-Transfer Insulator. *Physical Review Letters*, 99(15):156404, October 2007.
- [51] E. Z. Kurmaev, R. G. Wilks, A. Moewes, L. D. Finkelstein, S. N. Shamin, and J. Kuneš. Oxygen x-ray emission and absorption spectra as a probe of the electronic structure of strongly correlated oxides. *Phys. Rev. B*, 77:165127, Apr 2008.
- [52] B. Kyung, S. S. Kancharla, D. Sénéchal, A.-M. S. Tremblay, M. Civelli, and G. Kotliar. Pseudogap induced by short-range spin correlations in a doped mott insulator. *Phys. Rev. B*, 73:165114, Apr 2006.
- [53] P Lambin and JP Vigneron. Computation of crystal green’s functions in the complex-energy plane with the use of the analytical tetrahedron method. *Physical Review B*, 29(6):3430–3437, 1984.

- [54] Joo-Hyoung Lee, Tatsuya Shishidou, and Arthur Freeman. Improved triangle method for two-dimensional brillouin zone integrations to determine physical properties. *Physical Review B*, 66(23):233102, December 2002.
- [55] E. Y. Loh, J. E. Gubernatis, R. T. Scalettar, S. R. White, D. J. Scalapino, and R. L. Sugar. Sign problem in the numerical simulation of many-electron systems. *Phys. Rev. B*, 41:9301–9307, May 1990.
- [56] L. B. Lucy. An iterative technique for the rectification of observed distributions. *Astronomical Journal*, 79:745, June 1974.
- [57] J. M. Luttinger and J. C. Ward. Ground-state energy of a many-fermion system. ii. *Phys. Rev.*, 118:1417–1427, Jun 1960.
- [58] Alexandru Macridin, M. Jarrell, Thomas Maier, P. R. C. Kent, and Eduardo D’Azevedo. Pseudogap and antiferromagnetic correlations in the hubbard model. *Phys. Rev. Lett.*, 97:036401, Jul 2006.
- [59] T Maier, G Alvarez, M Summers, and T Schulthess. Dynamic Cluster Quantum Monte Carlo Simulations of a Two-Dimensional Hubbard Model with Stripelike Charge-Density-Wave Modulations: Interplay between Inhomogeneities and the Superconducting State. *Physical Review Letters*, 104(24):247001, June 2010.
- [60] T. A. Maier, M. Jarrell, T. C. Schulthess, P. R. C. Kent, and J. B. White. Systematic study of d -wave superconductivity in the 2d repulsive hubbard model. *Phys. Rev. Lett.*, 95:237001, Nov 2005.
- [61] T. A. Maier, M. S. Jarrell, and D. J. Scalapino. Structure of the pairing interaction in the two-dimensional hubbard model. *Phys. Rev. Lett.*, 96:047005, Feb 2006.
- [62] Thomas Maier, Mark Jarrell, Thomas Pruschke, and Matthias H. Hettler. Quantum cluster theories. *Rev. Mod. Phys.*, 77:1027–1080, Oct 2005.
- [63] Thomas A Maier, M Jarrell, and D J Scalapino. Pairing interaction in the two-dimensional Hubbard model studied with a dynamic cluster quantum Monte Carlo approximation. *Physical Review B*, 74(9):094513, September 2006.
- [64] Nicola Marzari, Arash A. Mostofi, Jonathan R. Yates, Ivo Souza, and David Vanderbilt. Maximally localized wannier functions: Theory and applications. *Rev. Mod. Phys.*, 84:1419–1475, Oct 2012.

-
- [65] Jeffrey M. McKay and Victor E. Henrich. Structure of valence and conduction levels in nio. *Phys. Rev. Lett.*, 53:2343–2346, Dec 1984.
- [66] A. K. McMahan, James F. Annett, and Richard M. Martin. Cuprate parameters from numerical wannier functions. *Phys. Rev. B*, 42:6268–6282, Oct 1990.
- [67] R Micnas, J Ranninger, and St Robaszkiewicz. Superconductivity in narrow-band systems with local nonretarded attractive interactions. *Reviews of Modern Physics*, 62(1):113, 1990.
- [68] A. Migdal. Interaction between electrons and lattice vibrations in a normal metal. *Soviet Physics JETP*, 34(6):996–6, 1958.
- [69] F. Mila. Parameters of a hubbard hamiltonian to describe superconducting cu oxides. *Phys. Rev. B*, 38:11358–11367, Dec 1988.
- [70] A Moreo and D J Scalapino. Two-dimensional negative-U Hubbard model. *Physical Review Letters*, 66(7):946–948, 1991.
- [71] David R Nelson and J M Kosterlitz. Universal jump in the superfluid density of two-dimensional superfluids. *Physical Review Letters*, 39(19):1201–1205, 1977.
- [72] M. R. Norman, D. Pines, and C. Kallin. The pseudogap: friend or foe of high t/c ? *Advances in Physics*, 54(8):715–733, 2005.
- [73] Michael R. Norman. The challenge of unconventional superconductivity. *Science*, 332(6026):196–200, 2011.
- [74] Phani K. V. V. Nukala, Thomas A. Maier, Michael S. Summers, Gonzalo Alvarez, and Thomas C. Schulthess. Fast update algorithm for the quantum monte carlo simulation of the hubbard model. *Phys. Rev. B*, 80:195111, Nov 2009.
- [75] S. Okamoto, A. J. Millis, H. Monien, and A. Fuhrmann. Fictive impurity models: An alternative formulation of the cluster dynamical mean-field method. *Phys. Rev. B*, 68:195121, Nov 2003.
- [76] Thereza Paiva, Raimundo R dos Santos, R T Scalettar, and PJH Denteneer. Critical temperature for the two-dimensional attractive Hubbard model. *Physical Review B*, 69(18):184501, 2004.
- [77] O. Parcollet, G. Biroli, and G. Kotliar. Cluster dynamical mean field analysis of the mott transition. *Phys. Rev. Lett.*, 92:226402, Jun 2004.

- [78] M Potthoff. Self-energy-functional approach: Analytical results and the mott-hubbard transition. *The European Physical Journal B - Condensed Matter*, 36(3):335–348, December 2003.
- [79] M Potthoff. Self-energy-functional approach to systems of correlated electrons. *The European Physical Journal B - Condensed Matter*, 32(4):429–436, April 2003.
- [80] X. Ren, I. Leonov, G. Keller, M. Kollar, I. Nekrasov, and D. Vollhardt. Lda+ dmft computation of the electronic spectrum of nio. *Physical Review B*, 74(19):195114, 2006.
- [81] WH Richardson. Bayesian-based iterative method of image restoration. *Journal of the Optical Society of America*, 62(1):55–59, 1972.
- [82] S. Rombouts, K. Heyde, and N. Jachowicz. A discrete hubbard-stratonovich decomposition for general, fermionic two-body interactions. *Physics Letters A*, 242(4–5):271 – 276, 1998.
- [83] S. M. A. Rombouts, K. Heyde, and N. Jachowicz. Quantum monte carlo method for fermions, free of discretization errors. *Phys. Rev. Lett.*, 82:4155–4159, May 1999.
- [84] A. N. Rubtsov, V. V. Savkin, and A. I. Lichtenstein. Continuous-time quantum monte carlo method for fermions. *Phys. Rev. B*, 72:035122, Jul 2005.
- [85] Leonid I. Rudin, Stanley Osher, and Emad Fatemi. Nonlinear total variation based noise removal algorithms. *Physica D: Nonlinear Phenomena*, 60(1–4):259 – 268, 1992.
- [86] GA Sawatzky and JW Allen. Magnitude and origin of the band gap in nio. *Physical review letters*, 53(24):2339–2342, 1984.
- [87] D. J. Scalapino and R. L. Sugar. Monte carlo calculations of coupled boson-fermion systems. ii. *Phys. Rev. B*, 24:4295–4308, Oct 1981.
- [88] R T Scalettar, E Y Loh, J E Gubernatis, A Moreo, S R White, D J Scalapino, R L Sugar, and E Dagotto. Phase diagram of the two-dimensional negative-U Hubbard model. *Physical Review Letters*, 62(12):1407–1410, 1989.
- [89] C E Shannon and W Weaver. A mathematical theory of communication. *Bell Syst. Tech. J.*, 27(379), 1948.

-
- [90] Z.-X. Shen, R. S. List, D. S. Dessau, B. O. Wells, O. Jepsen, A. J. Arko, R. Bartlett, C. K. Shih, F. Parmigiani, J. C. Huang, and P. A. P. Lindberg. Electronic structure of nio: Correlation and band effects. *Phys. Rev. B*, 44:3604–3626, Aug 1991.
- [91] R N Silver, D S Sivia, and J E Gubernatis. Maximum-entropy method for analytic continuation of quantum monte carlo data. *Physical Review B*, 41(4):2380–2389, February 1990.
- [92] J. C. Slater. The ferromagnetism of nickel. *Phys. Rev.*, 49:537–545, Apr 1936.
- [93] Peter Staar, Thomas A Maier, and Thomas C Schulthess. Efficient non-equidistant FFT approach to the measurement of single- and two-particle quantities in continuous time Quantum Monte Carlo methods. *Journal of Physics: Conference Series*, 402:012015, December 2012.
- [94] Peter Staar, Thomas A. Maier, Michael S. Summers, Gilles Fourestey, Raffaele Solca, and Thomas C. Schulthess. Taking a quantum leap in time to solution for simulations of high-*t_c* superconductors. In *Proceedings of SC13: International Conference for High Performance Computing, Networking, Storage and Analysis, SC '13*, pages 1:1–1:11, New York, NY, USA, 2013. ACM.
- [95] Louis Taillefer. *Scattering and Pairing in Cuprate Superconductors*, volume 1 of *Annual Review of Condensed Matter Physics*. ANNUAL REVIEWS, 4139 EL CAMINO WAY, PO BOX 10139, PALO ALTO, CA 94303-0897 USA, 2010.
- [96] K. Terakura, T. Oguchi, A. R. Williams, and J. Kübler. Band theory of insulating transition-metal monoxides: Band-structure calculations. *Phys. Rev. B*, 30:4734–4747, 1984.
- [97] O. Tjernberg, S. Söderholm, G. Chiaia, R. Girard, UO Karlsson, H. Nylén, and I. Lindau. Influence of magnetic ordering on the nio valence band. *Physical Review B*, 54(15):10245, 1996.
- [98] Matthias Troyer and Uwe-Jens Wiese. Computational complexity and fundamental limitations to fermionic quantum monte carlo simulations. *Phys. Rev. Lett.*, 94:170201, May 2005.
- [99] H.J. Vidberg and J.W. Serene. Solving the eliashberg equations by means of *n*-point padé approximants. *Journal of Low Temperature Physics*, 29(3-4):179–192, 1977.

- [100] Yayu Wang, N. P. Ong, Z. A. Xu, T. Kakeshita, S. Uchida, D. A. Bonn, R. Liang, and W. N. Hardy. High field phase diagram of cuprates derived from the nernst effect. *Phys. Rev. Lett.*, 88:257003, Jun 2002.
- [101] Philipp Werner, Armin Comanac, Luca de' Medici, Matthias Troyer, and Andrew J. Millis. Continuous-time solver for quantum impurity models. *Phys. Rev. Lett.*, 97:076405, Aug 2006.
- [102] Philipp Werner, Emanuel Gull, Olivier Parcollet, and Andrew J. Millis. Momentum-selective metal-insulator transition in the two-dimensional hubbard model: An 8-site dynamical cluster approximation study. *Phys. Rev. B*, 80:045120, Jul 2009.
- [103] Philipp Werner and Andrew J. Millis. Hybridization expansion impurity solver: General formulation and application to kondo lattice and two-orbital models. *Phys. Rev. B*, 74:155107, Oct 2006.
- [104] John A Wilson. Developments in the negative- U modelling of the cuprate HTSC systems. *Journal of Physics: Condensed Matter*, 13(50):R945–R977, November 2001.
- [105] F. C. Zhang and T. M. Rice. Effective hamiltonian for the superconducting cu oxides. *Phys. Rev. B*, 37:3759–3761, Mar 1988.